Control of Light-Matter Interactions in Classical and Quantum Optics

by

Anas Othman

A thesis

presented to the University Of Waterloo

in fulfilment of the

thesis requirement for the degree of

Doctor of Philosophy

in

Physics

Waterloo, Ontario, Canada, 2018

Examining Committee Membership

The following served on the Examining Committee for this thesis. The decision of the Examining Committee is by majority vote.

1 - Supervisor	Prof. **David Yevick**
2 - Internal examiner	Prof. **Russell Thompson**
3 - Internal examinar	Prof. **James Martin**
4 - Internal/External examinar	Prof. **Omar Ramahi**
5 - External examinar	Prof. **Daniel F.V. James** (University of Toronto)

Author's Declaration

This thesis consists of material all of which I authored or co-authored: see Statement of Contributions included in the thesis. This is a true copy of the thesis, including any required final revisions, as accepted by my examiners.

I understand that my thesis may be made electronically available to the public.

Statement of Contributions

I am the primary author of the material of this thesis which was performed under guidance and supervision of Prof. **David Yevick**. Most of the chapters of of this thesis have been published or are submitted for publication

[1] - Anas Othman and David Yevick, "Stretchable photonic crystal design", Optical and Quantum Electronics, **48**, 207 (2016).

[2] - Anas Othman and David Yevick, "Enhanced negative refractive index control in a 5-level system", Journal of Modern Optics, **64**, 1208 (2017).

[3] - Anas Othman and David Yevick, "The interaction of a N-type four level atom with the electromagnetic field for a Kerr medium induced intensity-dependent coupling", International Journal of Theoretical Physics, **57**, 159 (2018).

We have one project collaborative with Prof. **Mohammed Al-Amri**, and the resultant paper is submitted to a journal

[4] - Anas Othman, David Yevick, and Mohammed Al-Amri, "Generation of three wide frequency bands within a single white light cavity", (**submitted**).

And lastly, we had one paper on a conference

[5] - Anas Othman, "The superposition of two identical states: The empty state", Photonics North (PN), (2016).

Abstract

In this thesis, we examined a series of techniques for controlling the interaction of light with matter that could be employed to optimize or to control physical phenomena in various potential applications. Some of these schemes are described with classical electrodynamic theory while others require a semi-classical or full quantum framework.

In Ch.(2), we study numerically two implementations of stretchable photonic crystals (SPCs) embedded in elastic polymers. Our analysis, which classifies the bandgaps in terms of two simply determined parameters, indicates that such structures exhibit bandgaps that can be readily adjusted by straining the polymer.

In Ch.(3), we considered a five-level atomic system in a dense gas interacting with two low-intensity fields. By examining the influence of different parameters on the refraction index we found that by adjusting the ratio of the two magnetic amplitudes associated with the fields the effects of atomic coherence can be simply controlled. As well, a negative index of refraction can be achieved and controlled over a wide wavelength range with minimal absorption.

In Ch.(4), we theoretically investigated the double Λ scheme inside a Fabry-Pérot cavity. By introducing a weak probe beam and two strong driving fields and employing an incoherent pumping mechanism we found that when the intensity of the two driving fields are equal, a single giant white band was generated. However, when they are not equal, three white bands can be present in one cavity. This procedure can also be employed to displace the center frequency of the white band.

In Ch.(5), we studied the interaction of a N-type four-level atom with a single field in the presence of an intensity-dependent coupling in a nonlinear Kerr medium. The exact analytic solution is obtained in the case that the atom and electromagnetic field are initially in a higher excited state and a coherent state, respectively. It is then demonstrated that nonclassical properties such as the degree of entanglement stabilization, Kerr medium nonclassical control, and squeezed light can be

more efficiently realized and controlled within this four-level framework than in many competing procedures.

Finally, in Ch.(6), we theoretically studied the superposition of two nearly identical coherent states. This "near coherent" state exhibits numerous nonclassical properties such as sub-Poissonian statistics, squeezing for certain relative phases of the superposition and a partially negative Wigner function.

Acknowledgements

First of all, I would like to thank **My God** for guiding me to finish the Ph.D. and for every single thing happened in my life. Then, I would like to provide many thanks to my supervisor **Prof. David Yevick** for all his helpful advice and his continuous support. Also, many thanks to **Prof. Mohammed Al-Amri** for his supervising and welcoming me in Saudi Arabia.

I also would like to thank my wife **Basma Shawsh** for her excellent continuous encouraging and her patient to finish this project. My mother **Aisha Al-Turk** is indeed also acknowledged and thanked for her sincere prayers. Also, many thanks to my university **Taibah university** for their continued financial support. Besides, I cannot forget the great welcoming and hospitality of KACST (King Abdulaziz City for Science and Technology) as I did one of my chapters there. Also, many thanks to **university of Waterloo** for their great environment of study and their supports. We also thank **Omar Alshehri** for his remarkable advice in some parts of this thesis.

To conclude, I would like to thank every single one helped or advised me to finish this thesis. And to whom I have thanked, this small acknowledgment is not sufficient to thank you. And to whom I did not mention and helped me to finish this project, you indeed are acknowledged and please accept my apology for forgetting to mention your name. But indeed your good deeds will be rewarded either in this life or afterlife.

Table of Contents

List of Figures

List of Abbreviations

QED	Quantum electrodynamic
TISE	Time independent Schrödinger equation
SE	Schrödinger equation
EIT	Electromagnetically induced transparency
PC	Photonic crystals
SPC	Stretchable photonic crystal
FDTD	Finite-difference time domain
BPM	Beam propagation method
PWE	Plane wave expansion
RAW	Rotating wave approximation
EM	Electromagnetic
WLC	White light cavity
JCM	Jaynes-Cummings model
CPT	Coherent population trapping
EIA	Electromagnetically induced absorption
SCS	Schrödinger cat state
DEM	Degree of entanglement

Chapter 1

Introduction

Quantum optics combines quantum mechanics and electrodynamics by describing the interactions of light and matter when the application requires that at least one of these be treated as quantized. Applications of the theory include quantum information, quantum computing, lasers, masers and accurate measurements.

The electromagnetic field can be described by different physical theories depending on the degree of approximation. Generally, the quantum effects can be ignored when the number of detected photons is large such as in a typical light beam, or when the details of the interaction of light with matter are irrelevant. In this case, the light can be described classically as in a laser beam passing through transparent materials, open slots, classical waveguides, photonic crystals, empty cavities, and nonlinear materials.

On the other hand, for a large number of incident photons, if quantum effects are significant, a semi-classical approach in which the light beam is treated classically, while the interaction of the light with matter is instead considered quantum mechanically is generally employed. Examples of these such interactions are the description of lasing, electromagnetically induced transparency (EIT), optical white light cavities and nonlinear coefficient enhancement.

Finally, for a small number of photons, the electromagnetic field is generally treated as fully quantized. Some phenomena which cannot be described by the previous theories, but can be explained by this theory including entanglement, squeezed states, photon anti-bunching, spontaneous emission and collapse and revival phenomenon. Such an approach, however, cannot generally predict interactions of high-energy photons with matter such as pair production and Lamb shifts, which instead

requires the formalism of quantum electrodynamics and high energy physics. Fig.(1.1), compares the capabilities of the different theories of the light-matter interactions.

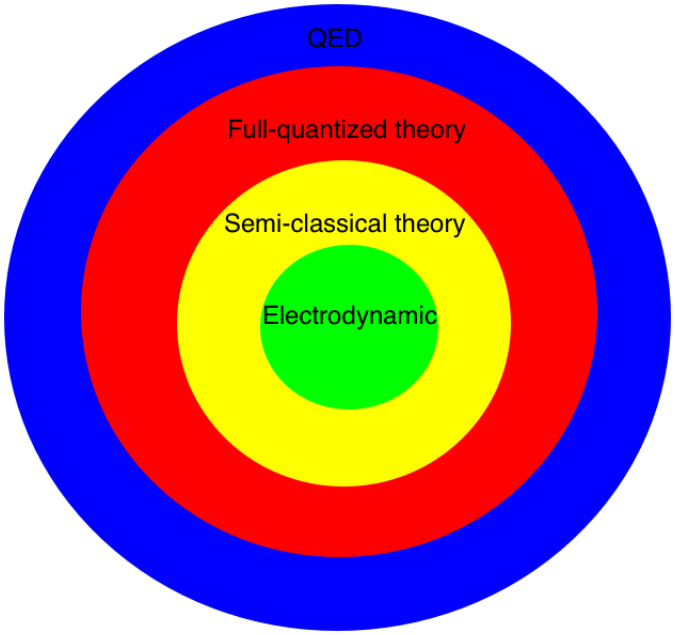

Figure 1.1: Relationships between different theories of light-matter interactions

This thesis concerns quantum light-matter interactions applications at low energy, primarily in quantum optics. Classical, semi-classical and full quantum descriptions are employed to generate proposals for controlling or enhancing various physical phenomena. In particular, the chapters of this thesis cover

1) Photonic crystals devices that reflect light completely within a band of frequencies termed the optical band gap. Such materials can be employed in quantum optics to increase the strength of certain optical interactions. In Ch.(2) a classical description of light is therefore applied to examine the possibility of varying the optical band gap based in stretchable polymer devices.

2) Negative refractive index materials are usually fabricated from complex periodic structures termed metamaterials, which however generally exhibit high absorption. In Ch.(3) a semi-classical study is instead employed to analyze 5-level atomic scheme interacts with two fields in a dense gas that yields a negative refractive index with near zero absorption.

3) White light cavities resonate within a band of frequencies but are generally restricted to a fixed frequency region. In Ch.(4), we propose a double Λ scheme generated by a certain pumping mechanisms and coupling fields. From a semi-classical analysis, it is demonstrated that this procedure

generates three white light bands with controllable bandwidths and center positions.
4) A full quantum description is provided for the N-type interaction of a four-level atom a single light mode in a nonlinear surrounding in Ch.(5). This analysis demonstrates that the resulting light is squeezed, anti-bunched and entangled more effectively than in many other comparable systems.
5) Schrödinger cat light states in quantum optics are employed in quantum communications and elsewhere. In Ch.(6), we consider an extension of these states which we term near coherent states. We analyze the non-classical properties of these states and propose a method for creating them.

Thus the first three chapters Chs.(2-4) consider procedures for controlling classical optical properties such as the refractive index, wavelength spectrum and susceptibility while the following two chapters (5, 6) are concerned with nonclassical properties such as squeezing, anti-bunching, and entanglement. Thus the second chapter of the thesis employs the classical theory of light, while chapters (3,4) and chapters (5,6) employ semiclassical and full quantized theories. Finally, in the last of each chapter, we provided a summary which states our most important findings and suggested future work.

Chapter 2

Stretchable Photonic Crystals

Photonic crystals (PC) are materials containing 1D, 2D or 3D periodic structures with a lattice period on the order of the light wavelength, c.f. Fig.(2.1) [6]. As a result of Bragg scattering, these materials can exhibit a photonic band gap in the dispersion relation, analogous to the electronic band gap in atomic crystals. In the same manner that an electronic band gap precludes the transport of electrons with energies within the gap, the photonic band gap reflects light within the bandgap frequencies.

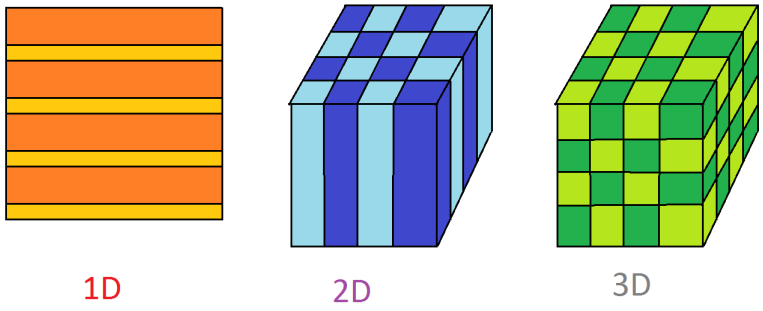

Figure 2.1: Photonic crystals of different dimensionalities. The alternating colors represent different dielectric constants.

Photonic crystals can be employed in a wide range of current or potential applications in both classical and quantum optics. These include waveguiding light through engineered line defects in 2D PCs [7, 8], confining light to a resonant cavity formed by a point defect [9, 10] and altering the spontaneous emission amplitude in appropriately designed cavities [10, 11].

In this chapter, we calculate the band structure of 2D elastic photonic crystals. In the first

section, we provide a theoretical background to PCs followed by 1D PC example. After that, we introduce stretchable photonic crystals (SPC) and consider two possible designs. The conclusion proposes several potential applications of SPCs.

2.1 Background

To introduce the topic of photonic crystals, we recall that Maxwell's equations in the absence of free charge and electric currents take the form

$$\begin{aligned} \nabla \cdot \mathbf{B}(\mathbf{r},t) &= 0, & \nabla \cdot \mathbf{D}(\mathbf{r},t) &= 0, \\ \nabla \times \mathbf{E}(\mathbf{r},t) &= -\tfrac{\partial \mathbf{B}(\mathbf{r},t)}{\partial t}, & \nabla \times \mathbf{H}(\mathbf{r},t) &= \tfrac{\partial \mathbf{D}(\mathbf{r},t)}{\partial t}, \end{aligned} \tag{2.1}$$

where $\mathbf{E}(\mathbf{r},t)$ is the electric field, $\mathbf{B}(\mathbf{r},t)$ is the magnetic induction, and $\mathbf{D}(\mathbf{r},t)$ and $\mathbf{H}(\mathbf{r},t)$ are the electric displacement and magnetic fields respectively. In this chapter, the relative permittivity or the dielectric constant ϵ of the material is a wavelength-independent function of spatial coordinates $\epsilon = \epsilon(\mathbf{r})$ and is assumed to be independent of the electric field amplitude while the material, is further assumed nonmagnetic so that $\mu = \mu_0$ everywhere. Further, $\epsilon(\mathbf{r})$ is assumed real corresponding to a transparent medium.

Based on these assumptions the electric displacement can be written as $\mathbf{D}(\mathbf{r},t) = \epsilon_0\epsilon(\mathbf{r})\mathbf{E}(\mathbf{r},t)$ while the magnetic field is $\mathbf{H}(\mathbf{r},t) = \mu_0\mathbf{B}(\mathbf{r},t)$, where ϵ_0 (μ_0) is the vacuum permittivity (permeability). If the fields are monochromatic,

$$\mathbf{E}(\mathbf{r},t) = \mathbf{E}(\mathbf{r})e^{-i\omega t}, \qquad \mathbf{H}(\mathbf{r},t) = \mathbf{H}(\mathbf{r})e^{-i\omega t}, \tag{2.2}$$

where ω is the angular frequency of the fields, the two curl equations of Eqs.(2.1) become

$$\nabla \times \mathbf{E}(\mathbf{r}) = i\mu_0\omega\mathbf{H}(\mathbf{r}), \qquad \nabla \times \mathbf{H}(\mathbf{r}) = -i\epsilon_0\omega\epsilon(\mathbf{r})\mathbf{E}(\mathbf{r}). \tag{2.3}$$

Hence taking the curl of $\mathbf{H}(\mathbf{r})$ from Eqs.(2.3), dividing both sides by $\epsilon(\mathbf{r})$ and taking the curl of both sides yields

$$\nabla \times \left(\frac{1}{\epsilon(\mathbf{r})}\nabla \times \mathbf{H}(\mathbf{r})\right) = -i\epsilon_0\omega\nabla \times \mathbf{E}(\mathbf{r}). \tag{2.4}$$

After substituting $\nabla \times \mathbf{E}(\mathbf{r})$ from Eq.(2.3) and applying $c^2 = (\mu_0\epsilon_0)^{-1}$, we arrive at the master

equation

$$\nabla \times \left(\frac{1}{\epsilon(\mathbf{r})} \nabla \times \mathbf{H}(\mathbf{r}) \right) = \left(\frac{\omega}{c} \right)^2 \mathbf{H}(\mathbf{r}). \tag{2.5}$$

For a given set of boundary conditions, this equation generates an eigenvalue problem, where $\mathbf{H}(\mathbf{r})$ are the eigenfunctions and ω^2/c^2 are the eigenvalues. Once $\mathbf{H}(\mathbf{r})$ is determined, the electric field is given by the Eqs.(2.3) as

$$\mathbf{E}(\mathbf{r}) = \frac{i}{\omega \epsilon_0 \epsilon(\mathbf{r})} \nabla \times \mathbf{H}(\mathbf{r}). \tag{2.6}$$

Another important feature of the master equation is its scalability. That is, if vector $\mathbf{r}$ is scaled by s as $\mathbf{r} \to \mathbf{r}/s$, where s is any real value so that ∇ becomes $s\nabla$, the master equation is replaced by

$$s\nabla \times \left(\frac{1}{\epsilon(\mathbf{r}/s)} s\nabla \times \mathbf{H}(\mathbf{r}/s) \right) = \left(\frac{\omega}{c} \right)^2 \mathbf{H}(\mathbf{r}/s). \tag{2.7}$$

which can be rewritten as

$$\nabla \times \left(\frac{1}{\epsilon(\mathbf{r}/s)} \nabla \times \mathbf{H}(\mathbf{r}/s) \right) = \left(\frac{\omega}{sc} \right)^2 \mathbf{H}(\mathbf{r}/s). \tag{2.8}$$

which reproduces Eq.(2.5) scaled by $1/s$. Accordingly results for a given structure can be applied to a scaled structure by if the wavelength is also appropriately scaled.

2.1.1 Photonic crystals

We now specialize to periodic photonic crystals. Approximating a finite crystal by an infinite or possibly semi-infinite structure, we can define a unit cell as the smallest rectangular repeating unit in the lattice. These cells can be described by their basis vectors $\mathbf{a} = (\mathbf{a_1}, \mathbf{a_2}, \mathbf{a_3})$ such that the origin of any unit cell in the lattice can be expressed as $\mathbf{R} = l\mathbf{a_1} + m\mathbf{a_2} + n\mathbf{a_3}$, where (n, l, m) are integers. A unit cell, a unit lattice vector, and $\mathbf{R}$ vector are illustrated in Fig.(2.2).

The reciprocal vectors $\mathbf{b} = (\mathbf{b_1}, \mathbf{b_2}, \mathbf{b_3})$ are then defined by $\mathbf{a} \cdot \mathbf{b} = 2\pi\delta_{ij}$, where δ_{ij} represents the Kronecker delta function. After some algebra, these vectors can be expressed as

$$\mathbf{b_1} = 2\pi \frac{\mathbf{a_2} \times \mathbf{a_3}}{\mathbf{a_1} \cdot \mathbf{a_2} \times \mathbf{a_3}}, \qquad \mathbf{b_2} = 2\pi \frac{\mathbf{a_3} \times \mathbf{a_1}}{\mathbf{a_1} \cdot \mathbf{a_2} \times \mathbf{a_3}}, \qquad \mathbf{b_3} = 2\pi \frac{\mathbf{a_1} \times \mathbf{a_2}}{\mathbf{a_1} \cdot \mathbf{a_2} \times \mathbf{a_3}}. \tag{2.9}$$

The Brillouin zone is then defined as the unit cell of the reciprocal lattice. The Bloch waves of the

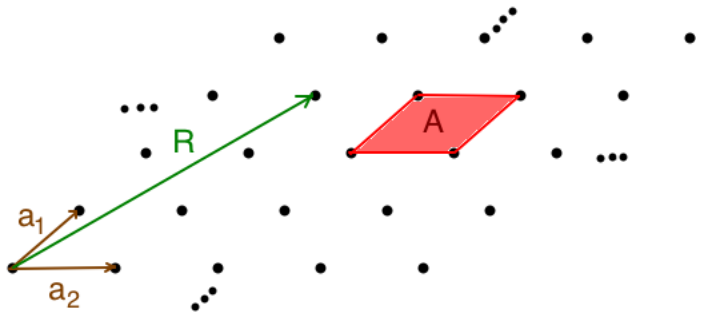

Figure 2.2: An 2D lattice for which the unit vectors are $\mathbf{a_1}$ and $\mathbf{a_2}$, a unit cell is colored red at the position (2,2) and a position vector $\mathbf{R}$ points to the cell at $(3,1)$.

crystal are then defined by

$$\mathbf{H}(\mathbf{r}) = \mathbf{u}(\mathbf{r})e^{i\mathbf{k}\cdot\mathbf{r}}, \tag{2.10}$$

where $\mathbf{u}(\mathbf{r})$ is a periodic function with the same periodicity of the lattice, so $\mathbf{u}(\mathbf{r}) = \mathbf{u}(\mathbf{r}+\mathbf{R})$, and $\mathbf{k}$ is the Bloch wave vector which is a combination of the primitive reciprocal vectors. Applying the Bloch theorem of Eq.(2.10) to the master equation with a Bloch wave vector given by $\mathbf{k} = k_1\mathbf{b_1} + k_2\mathbf{b_2} + k_3\mathbf{b_3}$, where k_i can take any real value inside the Brillouin zone then yields

$$\begin{aligned} \nabla \times \left[\tfrac{1}{\epsilon(\mathbf{r})}\nabla \times \left[\mathbf{u}(\mathbf{r})e^{i\mathbf{k}\cdot\mathbf{r}}\right]\right] &= \left(\tfrac{\omega(\mathbf{k})}{c}\right)^2 \mathbf{u}(\mathbf{r})e^{i\mathbf{k}\cdot\mathbf{r}}, \\ (i\mathbf{k}+\nabla) \times \tfrac{1}{\epsilon(\mathbf{r})}(i\mathbf{k}+\nabla) \times \mathbf{u}(\mathbf{r}) &= \left(\tfrac{\omega(\mathbf{k})}{c}\right)^2 \mathbf{u}(\mathbf{r}), \end{aligned} \tag{2.11}$$

where the explicit dependence of ω on $\mathbf{k}$ is introduced. While this equation is restricted to a single Brillouin zone PC, if additional symmetries are present, it is only necessary to solve the equation within a smaller region termed the irreducible Brillouin zone as detailed in e.g. [6, 12].

Since in general the master equation cannot be solved analytically, numerical methods such as the imaginary distance beam propagation method (BPM), the finite-difference time domain (FDTD) and the plane wave expansion (PWE) can be applied to obtain the dispersion relation. [13–15]. In the next section, we consider for illustration a 1D PC example.

2.1.2 One dimensional PC example

One of the simplest 1D PC structures, which is periodic only in the z direction, so that $\epsilon(\mathbf{r}) \to \epsilon(z)$ is illustrated in Fig.(2.3). The primitive lattice vector here is $\mathbf{a} = a\mathbf{z}$ while the primitive reciprocal vector is then $\mathbf{b} = (2\pi/a)\mathbf{z}$. Consequently, the Brillouin zone extends between $-\pi/a \leq k_z \leq \pi/a$.

For an electromagnetic wave incident in the z direction, $\mathbf{H}(\mathbf{r}) \rightarrow \mathbf{H}(z)$. If we further assume x polarization, the master equation, Eq.(2.11), simplifies to the scalar wave equation

$$\left(ik_z + \frac{d}{dz}\right)\frac{1}{\epsilon(z)}\left(ik_z + \frac{d}{dz}\right)u_x(z) = \left(\frac{\omega(k_z)}{c}\right)^2 u_x(z), \tag{2.12}$$

where $k_z = k$ is the component of the z axis of $\mathbf{k}$.

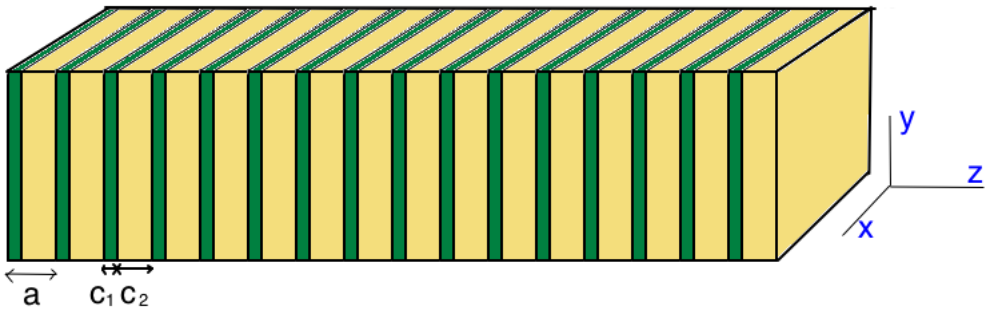

Figure 2.3: A 1D PC with two alternately repeating layers in the z direction, where a is the length of the unit cell. The colors indicate different materials.

At this point the dispersion relation $\omega(k_z)$ or the field $H_x(z)$ can be determined. If the length of each of the first material layers equals c_1, while the second is c_2 and the corresponding dielectric constants are $\epsilon = 9$ and $\epsilon = 1$, the PWE method yields the band structure of Fig.(2.4). Here the left figure displays the band structure of a single material with $\epsilon = 9$ given by

$$\omega(k) = \frac{ck}{\sqrt{\epsilon}}. \tag{2.13}$$

while the middle figure is the 1D PC band structure with $c_1 = c_2 = 0.5a$ and ϵ altering between 9 and 1 while the right figure pertains to $c_1 = 0.2a$ and $c_2 = 0.8a$ for the same values of ϵ. The value of (a) is not physically meaningful since the master equation and its solution can be scaled according to Eq.(2.8).

The left figure of Fig.(2.4) indicates that when only one material is present the band gap is absent, where the folded Brillouin zone of Eq.(2.13) is displayed for comparison. In the middle and right figures a band gap is however evident. Thus in the middle figure, the first band gap is positioned between $0.1811(2\pi c)/a < \omega < 0.2999(2\pi c)/a$, incident light with frequencies inside this bandgap is completely Bragg reflected. In the right figure, the gap between the second and third bands occurs for $0.6431 < \omega a/(2\pi c) < 0.7043$, which is the smallest gap between the two bands. An additional

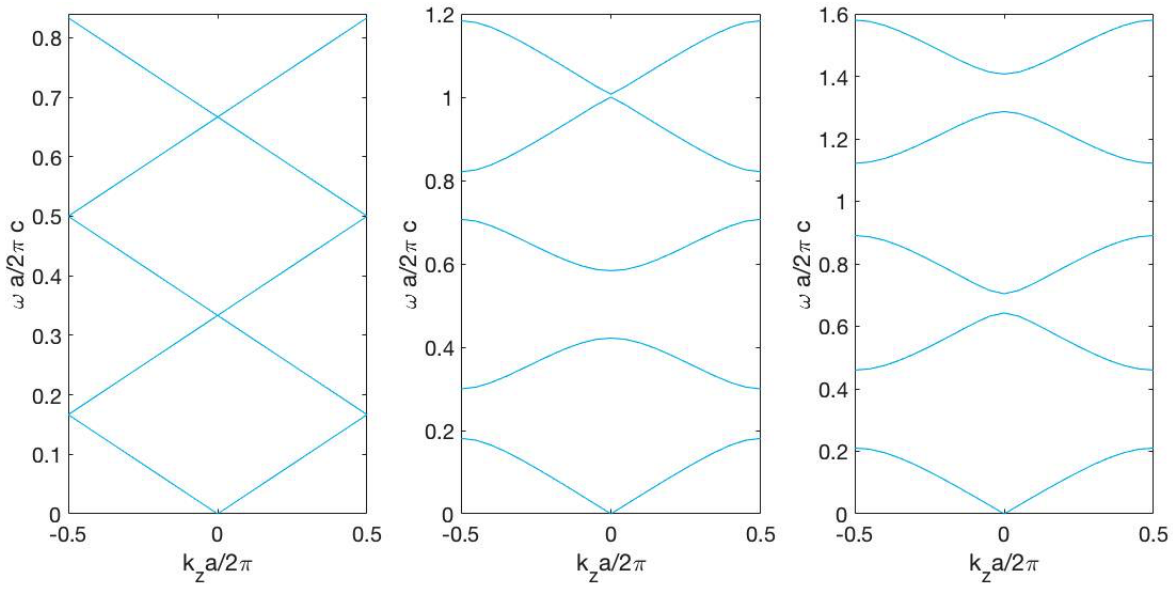

Figure 2.4: The first 5 bands of the 1D PC band structure for the material parameters presented in the text.

feature evident from Fig.(2.4) is that the lowest band becomes nearly linear as $\omega \to 0$. This feature is expected since for small frequencies and therefore large wavelengths the electromagnetic wave is only influenced by the average refractive indices of the layers. Finally, it should be noted that the size of a band gap is a function of the dielectric constant values and the spacing of the materials lengths c_1, c_2.

2.2 Stretchable photonic crystal (SPC)

In higher dimensional systems such as slab waveguides [16–19], cylindrical fibers [20–23], and geometries as well as three dimensional cavities [24, 25] the optical band structure is far more complex than that of 1D PCs and therefore generally must be determined numerically. Accordingly, in the remainder of this chapter the band structure and resultant band gaps were calculated with the PWE tool of the commerical OptiFDTD package. After results were obtained for numerous material and geometric parameters the most significant findings were collected and presented below.

Standard 2D PC structures are generally fabricated by drilling triangular lattices of air holes into slab waveguides or by etching square lattices of rods, which respectively results in bandgaps for TM and TE polarizations. Light can then be guided by Bragg reflection from the surrounding PC along one or more straight, curved or intersecting line defects generated, for example by omitting

cells of the periodic structure, changing the refractive index or deforming the unit cell geometry [26–28]. In a similar fashion, surrounding a point defect with a PC creates a resonator [29, 30]. In dynamic structures the wavelength range of the bandgaps can further be altered by changing external parameters such as heat [31], electric current [32], and magnetic fields [33] or general physical forces [34].

Photonic crystals formed from elastic polymer material that can be distorted by mechanical stress. In view of the low polymer refractive index compared to that of e.g. semiconductors, rather than inserting air holes into the polymer a Stretchable Photonic Crystal (SPC) can be more effectively implemented by surrounding a lattice of dielectric rods, here assumed to be formed from a semiconductor with $n = \sqrt{\epsilon} = 3.6$, and with a polymer material with $n = \sqrt{\epsilon} = 1.4$ as in Fig.(2.5).

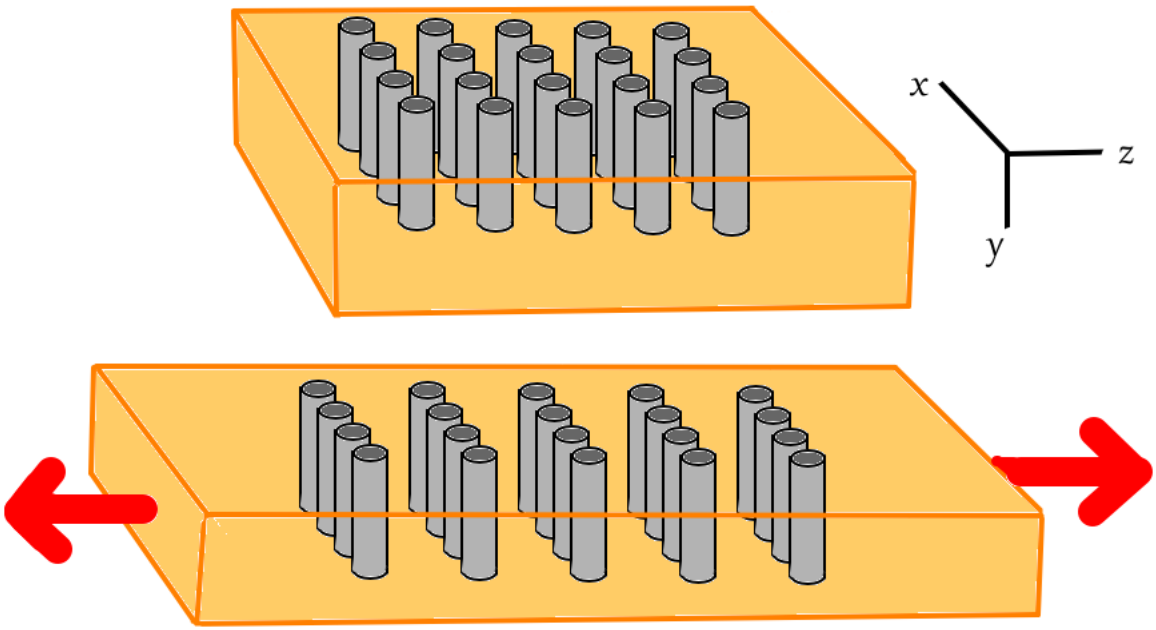

Figure 2.5: The proposed stretchable photonic crystal (SPC) structure, where orange and grey indicate polymer and semiconductor materials.

The upper and lower sections of the figure represent the SPC device without and with an applied force in the longitudinal, z, direction, where the lateral direction is denoted by x and the rods are separated by polymer regions. While a similar structure was fabricated in [35], we will examine both triangular and rectangular patterns of rods for both small and large deformations. By examining the full band structure, we further propose applications that utilize several simultaneous bandgap regions. Our analysis generalizes the work of previous authors in that it compares two types of pho-

tonic crystal structures in terms of two simply expressed parameters and suggests several potential applications.

2.3 Designs of SPC

2.3.1 Rectangular lattice

Following previous studies of square lattices [6, 36, 37], we first consider a rectangular lattice of dielectric rods of radius $r = fX_0$ with f a dimensionless constant and X_0 the spacing between adjacent rods in the lateral, x direction in the absence of applied forces, c.f. the left diagram of Fig.(2.6) which shows the rods in the absence of strain. Similarly denoting by Z_0 the zero strain spacing between the rods in z direction and $s_0 = Z_0/X_0$, the PC can be parametrized by the two values (f, s_0).

Since the volume of an SPC remains invariant in the presence of an applied strain, if the photonic crystal is transformed into a waveguiding structure by, for example, removing one line of rods, the strained material will possess a smaller lateral dimension. Further, if instead two photonic crystal regions are situated on both sides of a rib waveguide, unless a lateral compression force is applied to the side of each elastic region, the cladding regions would separate from the sides of waveguide. Additionally, under sufficiently large strain, the pillars could separate from the polymer generating additional air regions. Since however such effects can presumably be controlled through proper design, they are not considered further here. Quantitatively, if in response to an applied force the distance between adjacent pillars increases to $Z = gZ_0$ in the z-direction, the associated strain is given by

$$\epsilon = \frac{z' - z}{z} = \frac{gz - z}{z} = g - 1 \tag{2.14}$$

while from conservation of volume and the ratio between y and x, the spacing between the rods varies as

$$X = X_0/\sqrt{g}, \tag{2.15}$$

resulting in the configuration at the right of Fig.(2.6). Note that when

$$g_{square} = s_0^{-2/3} \tag{2.16}$$

$X = Z$ yielding a square arrangement of rods. The strain dependence of the photonic crystal bandgap can again be parametrized solely by (f, s_0) values once the frequency ω is scaled according to $\omega X_0/2\pi c$, effectively replacing X_0 as the third parameter. That is, each f and s_0 yield a different band gap (and associated band structure diagram), where the quasi-two dimensional unit cell contains a single rod and possesses an area ZX (see Figure(2.6)).

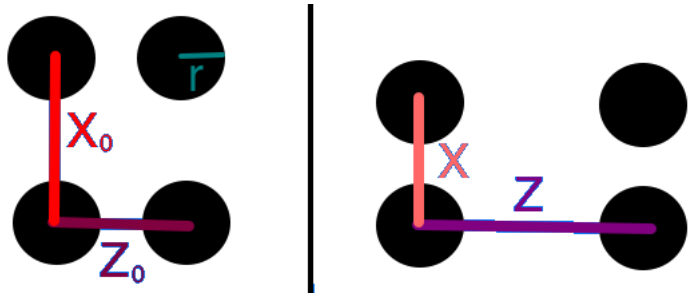

Figure 2.6: The configuration of rods in a rectangular lattice in the absence (left diagram) and presence (right diagram) of stress.

A rectangular lattice of dielectric rods typically yields a TM mode bandgap. To obtain a bandgap of maximum width, s_0 is often held fixed while f is varied [6]. Since, however the geometry of the unit cell depends on strain, the SPC profile must be optimized separately for each application. To illustrate the procedure, Fig.(2.7) displays two sets of values, $(0.2, 0.5)$ and $(1/7, 0.3644)$, that generate markedly different band gaps.

In the case of the $(0.2, 0.5)$ structure, which becomes a square lattice at $\epsilon = 0.587401$ the position and width of the largest bandgap decreases with strain nearly linearly from an initial normalized central frequency of 0.4 to 0.3. A second large bandgap occurs for strains between 0.8 and 1.6 at normalized frequencies of approximately twice the first major bandgap. In contrast, for the $(1/7, 0.3644)$ structure, which forms a square lattice at $\epsilon = 0.96011$ the dominant bandgap is initially narrow but increases in width until $\epsilon = 0.5$ only to subsequently decrease and vanish at 1.5. These varied behaviors indicate that the band gap properties can be in general adapted to numerous device requirements.

2.3.2 Triangular lattice

In contrast to a rectangular lattice, triangular lattices exhibit significant TE mode bandgaps. If the parameters r and s_0 are defined as $r = fX_0$, with X_0 defined in Fig.(2.8) and $s_0 = Z_0/X_0$, Eq.(2.15) is preserved. At the strain value Eq.(2.16), the triangular lattice of Fig.(2.8) coincides with a square

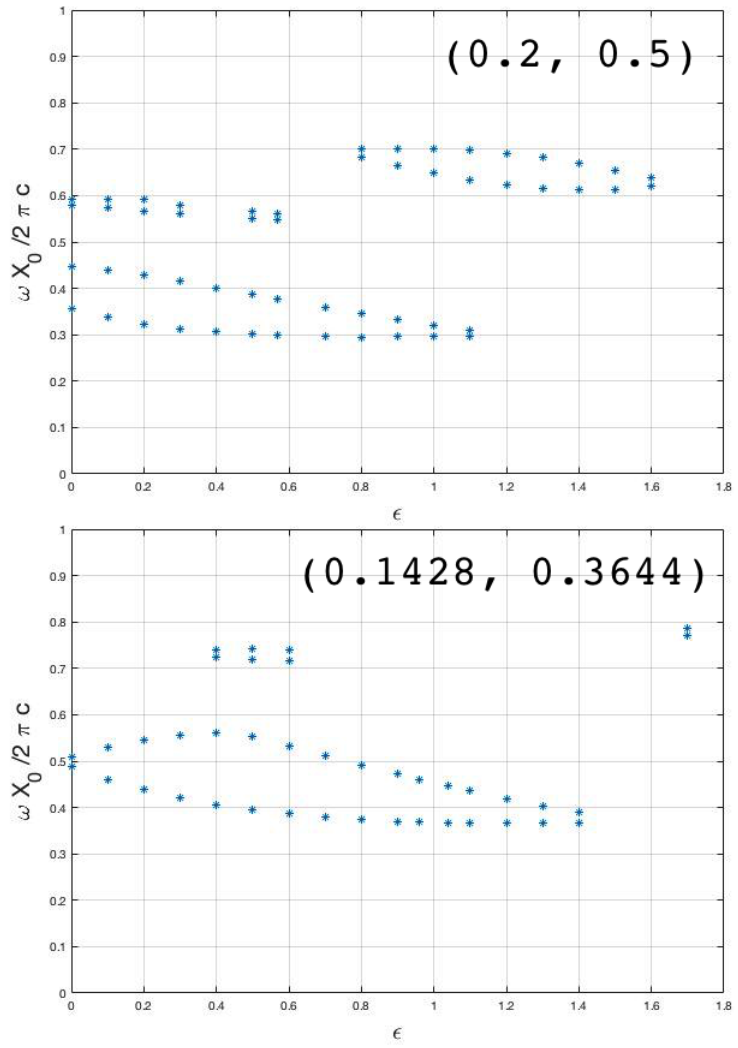

Figure 2.7: The bandgaps in normalized units for TM polarization for rectangular SPC:s specified by the parameter pairs $(0.2, 0.5)$ and $(0.1428, 0.3644)$.

lattice while for

$$g_{hex} = \left(\frac{1}{s_0 \tan 60}\right)^{2/3}. \tag{2.17}$$

the pattern of rods form equilateral triangles or equivalently, hexagons.

For the unit cell of Fig.(2.8), the vertical length a_x coincides with X, while the length in the direction of the strain a_z is denoted Z. The length, t, in the figure between two adjacent rods is then

$$t = \frac{\sqrt{Z^2 + X^2}}{2} = \frac{X_0}{2}\sqrt{g^2 s_0^2 + \frac{1}{g}}. \tag{2.18}$$

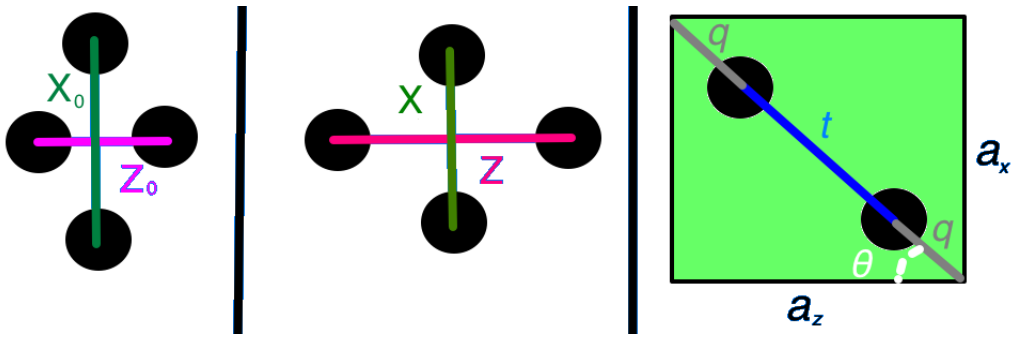

Figure 2.8: Triangular lattice in the absence (left figure) and presence (right figure) of strain. Far right: a unit cell of the lattice

while the angle θ equals

$$\tan\theta = \frac{1}{s_0 g^{3/2}}. \tag{2.19}$$

and $q = t/2$.

The bandgap as a function of strain for the two illustrative parameter sets $(0.1, 0.25)$, and $(0.15, 6/9)$ is displayed in Fig.(2.9). Note that for the $(0.1, 0.25)$ structure, a TM bandgap is present for strain values greater than 0.2 at a normalized frequency of ≈ 0.65 while a second bandgap appears for $\epsilon > 0.5$ at a normalized frequency of 1.1. A TE mode bandgap is present from 0.6 to 1.7 that varies slowly in position and width. This structure coincides with a square and a hexagonal lattice at strain values of $\epsilon = 1.5198$ and $\epsilon = 0.747161$, respectively. For the parameters $(0.15, 6/9)$ a wide TM bandgap is present for $\epsilon < 1.7$ while numerous additional smaller bandgaps of various widths are also present. Note as well that a complete (simultaneous TE and TM) bandgap appears for $0.8 < \epsilon < 1$ with a maximum size of ≈ 0.03 while a large TE bandgap is present in the figure centered at a nearly constant normalized frequency but with a strain-dependent width.

2.4 Potential applications and conclusions

While the calculations of this paper are only intended to illustrate the degree to which the bandgap can be mechanically adjusted in representative SPC structures, the results suggest numerous potential applications which vary depending on the details of the structure and geometry of the superlattice material. For example, a slab waveguide composed of a line of defects within an SPC will exhibit adjustable geometrical and optical properties. The feasibility of such a waveguide is evident from the nearly stress-invariant TM bandgaps present in both $(0.1, 0.25)$ and $(0.15, 6/9)$ triangu-

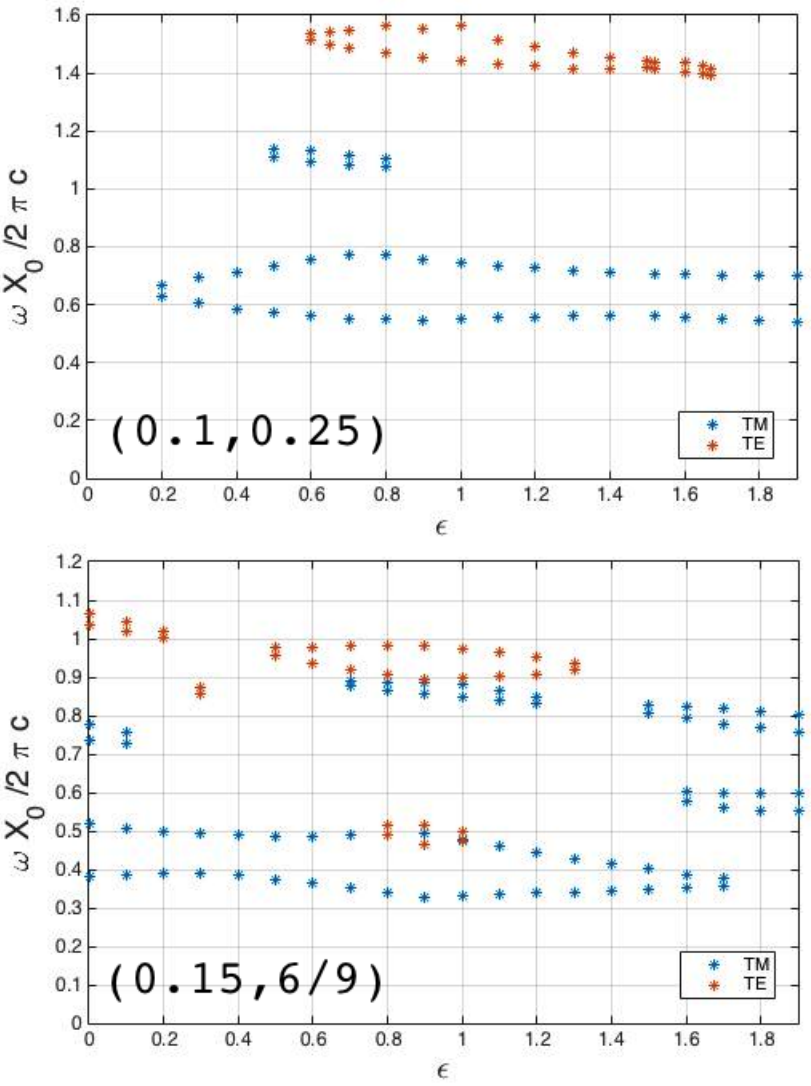

Figure 2.9: The strain dependence of the band gap in normalized frequency units for triangular SPC structures with parameter values $(0.1, 0.25)$ and $(0.15, 6/9)$ for strains $\epsilon < 1.9$.

lar lattice structures in Fig.(2.9). Since the bandgap widths vary only moderately with frequency, the waveguide can further be appreciably curved (or tapered) without incurring losses by applying non-uniform stresses. That is the wavguide segment at the left of Fig.(2.10) with initial width W_0, length, L_0 and slope angle ϕ_0 when stressed in the W_0 direction distorts to the waveguide at the right of the figure where the corresponding variables are related through the value of g according to

$$W = gW_0, \qquad L = \frac{L_0}{\sqrt{g}}, \qquad \tan\phi = \frac{\tan\phi_0}{g^{3/2}} \tag{2.20}$$

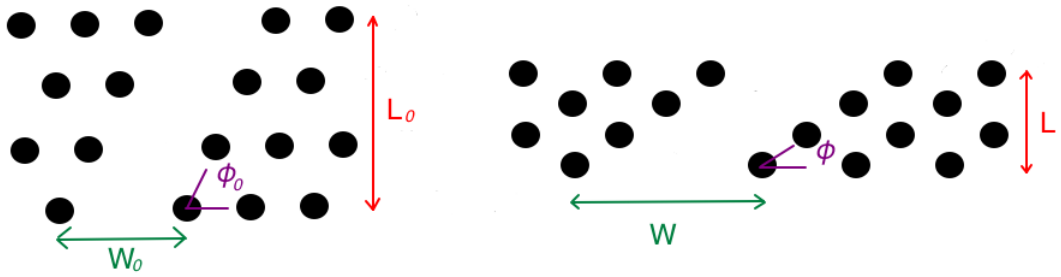

Figure 2.10: A slab SPC waveguide with a width W_0, length L_0, and angle ϕ_0 before (left figure) and after (right figure) stretching.

Numerous waveguiding structures can accordingly be generated in this manner.

Our results further extend previously reported work by implying that a tuneable resonator formed from a point defect in a $2D$ SPC can possess Q factors at a spectrum of wavelengths that can be varied by applying stress to effect both small and large deformations of the material (for either triangular or square lattices). Additionally, the behavior of the two large bandgaps in the diagram for the square lattice parameters $(0.2, 0.5)$ in Fig.(2.7) suggests a two wavelength switch that reflects one wavelength reflects and transmits the second at one strain value while transmitting the first and reflecting the second at a different value. The large number of bandgaps evident for the parameter values $(0.15, 6/9)$ in Fig.(2.9) again indicate that this behavior could possibly be extended to a larger number or even a limited continuum range of frequencies.

Similarly, numerous potential applications could be envisioned for multiwavelength $3D$ flexible PC:s. Such SPC materials could provide a platform for a variety of innovative devices.

Chapter 3

Enhanced Negative Refractive Index Control

In the semi-classical treatment of the interaction of the electromagnetic field with matter, the field is modelled classically through Maxwell's equations while the atomic interaction is treated quantum mechanically. For example, electromagnetically induced transparency (EIT), laser properties, and electromagnetically induced absorption (EIA) are typically modelled in this manner.

The semiclassical theory can also be applied to negative refractive indices materials, which were first proposed by Victor Veselago in 1967 [38]. Such materials, which result when both the electric permittivity and magnetic permeability are negative, have significant potential applications such as Doppler shift and Cerenkov radiation reversals [38], evanescent wave amplification [39], sub-wavelength focusing [40], and perfect lenses [41].

As negative refractive index materials do not occur in nature, they must be artificially designed. While they can be created from metamaterials [42–47] and photonic crystals [48–50], these are difficult to manufacture, function in a limited wavelength range and exhibit high absorption as a result of electrical and magnetic resonances. Alternatively, in dense atomic gases in which both electric and magnetic transitions are present the magnetic susceptibility can be enhanced significantly in comparison to common gases for which the electric susceptibility typically exceeds the magnetic susceptibility by approximately four orders of magnitude. Accordingly, in this chapter, we propose a 5-level scheme in a dense gas with electric and magnetic dipole interactions. This enables the magnitude of the negative refractive index value to be varied without significantly increasing the

absorption from its minimum value.

This chapter is organized as follows: After a short description of the semiclassical model light-atom interactions we summarize previous work on generating negative refractive indices in dense gases. The new scheme is then introduced and analyzed theoretically. After the dependence of the refractive index on different physical parameters is examined, the chapter concludes with a summary and suggestions for future research.

3.1 Background

To introduce the semiclassical approach light-atom interactions, consider first the Hamiltonian of an electron in the absence of EM field interactions

$$\hat{H}_0 = \frac{\hat{\mathbf{P}}^2}{2m} + V(r), \tag{3.1}$$

where $\hat{H}_0$ is the unperturbed Hamiltonian of the electron, m is the mass of the electron, $\mathbf{P}$ is the quantum momentum operator of the electron, and $V(r)$ is a radial atomic potential. The time-independent Schrödinger equation (TISE) then yields for the bound states of the potential

$$\hat{H}_0\psi_k^0(\mathbf{r}) = E_k\psi_k^0(\mathbf{r}), \tag{3.2}$$

where $\psi_k^0(\mathbf{r})$ are the eigenfunctions of the unperturbed Hamiltonian H_0 in the spatial representation and E_k with $k = 0, 1, 2, 3, \cdots$ are the energy eigenvalues. The spatial representation follows from $\hat{\mathbf{r}}|\mathbf{r}\rangle = \mathbf{r}|\mathbf{r}\rangle$, so $\psi_k^0(\mathbf{r}) = \langle\mathbf{r}|k\rangle$. $|\psi\rangle$ is the full wave function of the system which can be expanded as $|\psi\rangle = \sum_{k=0}^{\infty} C_k|k\rangle$, where $|k\rangle$ is the wave function of the k state, and C_k are some probability amplitudes. The wave functions of a given state also satisfy the eigensystem equation which is $\hat{H}_0|k\rangle = E_k|k\rangle$.

Assuming that all the functions $|k\rangle$ are known, in the presence of an external field interacting with the electron, the Hamiltonian H_0 of Eq.(3.1) becomes

$$\hat{H}(\mathbf{r}, t) = \frac{1}{2m}\left[\hat{\mathbf{P}} - e\mathbf{A}(\mathbf{r}, t)\right]^2 + e\Phi(\mathbf{r}, t) + V(r), \tag{3.3}$$

where $\mathbf{A}(\mathbf{r}, t)$ and $\Phi(\mathbf{r}, t)$ are the vector and scalar potentials of the external field respectively and

e is the absolute charge of the electron. The electric and magnetic fields are defined as

$$\mathbf{E}(\mathbf{r},t) = -\nabla\Phi(\mathbf{r},t) - \frac{\partial \mathbf{A}(\mathbf{r},t)}{\partial t}, \qquad \mathbf{B}(\mathbf{r},t) = \nabla \times \mathbf{A}(\mathbf{r},t), \tag{3.4}$$

and they are invariant under the following transformation

$$\Phi(\mathbf{r},t) \to \Phi(\mathbf{r},t) - \frac{\partial \chi(\mathbf{r},t)}{\partial t}, \qquad \mathbf{A}(\mathbf{r},t) \to \mathbf{A}(\mathbf{r},t) + \nabla\chi(\mathbf{r},t). \tag{3.5}$$

The solution of the classical wave equation for the field $\mathbf{A}(\mathbf{r},t)$ of an atom at a position $\mathbf{r}_0$, takes the following form

$$\mathbf{A}(\mathbf{r}_0+\mathbf{r},t) = \mathbf{A}(t)e^{i\mathbf{k}\cdot(\mathbf{r}_0+\mathbf{r})} \approx \mathbf{A}(t)e^{i\mathbf{k}\cdot\mathbf{r}_0}(1 + i\mathbf{k}\cdot\mathbf{r} + \cdots), \tag{3.6}$$

where $\mathbf{k} = 2\pi/\lambda$ is the wave vector of the radiated wave. As $\mathbf{r}$ is of the order of the atomic radius while $|\mathbf{k}^{-1}|$ is comparable to the optical wavelength (in order of 10^{-7}), the product $\mathbf{k}\cdot\mathbf{r}$ can be neglected. Hence the atom is point-like with respect to a light field, which is termed the dipole approximation. The $\mathbf{A}(\mathbf{r},t)$ then takes the form

$$\mathbf{A}(\mathbf{r},t) = \mathbf{A}(t)e^{i\mathbf{k}\cdot\mathbf{r}_0} = \mathbf{A}(t), \tag{3.7}$$

where the atomic origin is set to $\mathbf{r_0} = 0$.

The time-dependent Schrödinger equation is now written as

$$\hat{H}(\mathbf{r},t)\psi(\mathbf{r},t) = i\hbar\frac{\partial\psi(\mathbf{r},t)}{\partial t} \tag{3.8}$$

Now, let us use the Coulomb (or radiation) gauge which is defined to satisfy $\Phi(\mathbf{r},t) = 0$ and $\nabla\cdot\mathbf{A}(t) = 0$. If we apply this gauge to the Hamiltonian of Eq.(3.3), it will be

$$\hat{H}(\mathbf{r},t) = \frac{1}{2m}\left[\hat{\mathbf{P}} - e\mathbf{A}(t)\right]^2 + V(r). \tag{3.9}$$

Let us now apply another arbitrary gauge $\chi(\mathbf{r},t)$, so

$$\Phi(\mathbf{r},t) \to 0 - \frac{\partial \chi(\mathbf{r},t)}{\partial t}, \qquad \mathbf{A}(t) \to \mathbf{A}(t) + \nabla\chi(\mathbf{r},t). \tag{3.10}$$

Eq.(3.9) then becomes

$$\hat{H}(\mathbf{r},t) = \frac{1}{2m}\left[\hat{\mathbf{P}} - e\mathbf{A}(t) + e\nabla\chi(\mathbf{r},t)\right]^2 + e\frac{\partial\chi(\mathbf{r},t)}{\partial t} + V(r). \tag{3.11}$$

In the gauge $\chi(\mathbf{r},t) = -\mathbf{A}(t)\cdot\mathbf{r}$,

$$\nabla\chi(\mathbf{r},t) = -\mathbf{A}(t), \qquad \frac{\partial\chi(\mathbf{r},t)}{\partial t} = -\mathbf{r}\cdot\frac{\partial\mathbf{A}(t)}{\partial t} = -\mathbf{r}\cdot\mathbf{E}(t), \tag{3.12}$$

the Hamiltonian of Eq.(3.11) becomes

$$\hat{H}(\mathbf{r},t) = \frac{\hat{\mathbf{P}}^2}{2m} + V(r) - e\mathbf{r}\cdot\mathbf{E}(t) = \hat{H}_0 + \hat{H}_I, \tag{3.13}$$

where H_I is the dipole interaction Hamiltonian $\hat{H}_I = -e\mathbf{r}\cdot\mathbf{E}(t) = \hat{\mathbf{d}}\cdot\mathbf{E}(t)$, where the dipole moment $\hat{\mathbf{d}} = -e\mathbf{r}$. For transitions between two states of identical parity the interaction instead equals $\hat{H}_I = \hat{\mu}\cdot\mathbf{B}(t)$ and is associated with magnetic transitions. Further discussions of these topics can be found in [51–53].

3.1.1 Density operator

Density operator solutions of the time-dependent SE incorporate statistical averaging and therefore provide information about the population and coherence of a given quantum system as well as many other statistical properties. In particular, consider a statistical mixture of pure states $|k\rangle$. The density operator is defined as

$$\hat{\rho} = \sum_{k=0}^{\infty} P_k |k\rangle\langle k|, \tag{3.14}$$

where P_k is the probability for the system to be at the state $|k\rangle$, and $\hat{\rho}$ is the density operator. Clearly

$$\sum_{k=0}^{\infty} P_k = 1. \tag{3.15}$$

while the expectation value of a given operator $\hat{O}$, is

$$\langle\hat{O}\rangle = \sum_{k=0}^{\infty} P_k \langle k|\hat{O}|k\rangle = \mathrm{Tr}(\hat{O}\hat{\rho}). \tag{3.16}$$

For a quantum state $|\psi\rangle = \sum_{k=0}^{\infty} C_k|k\rangle$ the density matrix acquires off-diagonal elements

$$\hat{\rho} = |\psi\rangle\langle\psi| = \sum_{k=0}^{\infty}\sum_{k'=0}^{\infty} C_{k'}^* C_k |k\rangle\langle k'|, \tag{3.17}$$

which are associated with the coherence of the system. The expectation value expression of Eq.(3.16) holds for this density operator as well.

The dynamic equation of the density operator for a Hermitian Hamiltonian can be derived from the time-dependent SE and its complex conjugate

$$\frac{\partial|\psi\rangle}{\partial t} = -\frac{i}{\hbar}\hat{H}|\psi\rangle, \qquad \frac{\partial\langle\psi|}{\partial t} = \frac{i}{\hbar}\langle\psi|\hat{H}, \tag{3.18}$$

From the definition of $|\psi\rangle$,

$$\sum_{k=0}^{\infty}\frac{\partial C_k}{\partial t}|k\rangle = -\frac{i}{\hbar}\sum_{k=0}^{\infty} C_k\hat{H}|k\rangle, \qquad \sum_{k=0}^{\infty}\frac{\partial C_k^*}{\partial t}\langle k| = \frac{i}{\hbar}\sum_{k=0}^{\infty} C_k^*\langle k|\hat{H}. \tag{3.19}$$

while the derivative of Eq.(3.17) with respect to time is

$$\frac{\partial\hat{\rho}}{\partial t} = \sum_{k=0}^{\infty}\sum_{k'=0}^{\infty}\left(\frac{\partial C_{k'}^*}{\partial t}C_k + C_{k'}^*\frac{\partial C_k}{\partial t}\right)|k\rangle\langle k'|. \tag{3.20}$$

Inserting Eq.(3.19), yields

$$\frac{\partial\hat{\rho}}{\partial t} = -\frac{i}{\hbar}\sum_{k=0}^{\infty}\sum_{k'=0}^{\infty} C_k C_{k'}^*\left(-|k\rangle\langle k'|\hat{H} + \hat{H}|k\rangle\langle k'|\right) = -\frac{i}{\hbar}\left[\hat{H},\hat{\rho}\right]. \tag{3.21}$$

which describes the evolution of the density operator and is termed the quantum Liouville equation or the Von Neumann equation of motion. Almost any quantum particle or any statistical ensemble can be studied using this equation. Various physical effects can be incorporated directly into this equation, for example state decay which can be modelled by writing

$$\dot{\hat{\rho}} = \frac{\partial\hat{\rho}}{\partial t} = -\frac{i}{\hbar}\left[\hat{H},\hat{\rho}\right] - \hat{S}\hat{\rho}\hat{S}^\dagger - \frac{1}{2}\{\hat{S}^\dagger\hat{S},\hat{\rho}\}, \tag{3.22}$$

where $\{a,b\} = ab + ba$, and the operator $\hat{S}$ describes physical effects such as pumping or state decay [54]. The elements of $\hat{S}$ must be specified such that the trace of the right-hand side of Eq.(3.22) vanishes. When the equation describes different physical processes it is often termed the

master equation (this is a separate terminology than the EM master equation of Eq.(2.5)). In the following section, we will apply the master equation formalism to a two-level system.

3.1.2 Two-level scheme

We first consider the simplest interaction of light with the two level system of Fig.(3.1). This scheme consists of two levels $|a\rangle$ (the excited state) and $|b\rangle$ (the ground state) and an interacting field $\mathbf{E}(t)$. The unperturbed Hamiltonian of the system $\hat{H}_0$ satisfies $\hat{H}_0|a\rangle = E_a|a\rangle$ and $\hat{H}_0|b\rangle = E_b|b\rangle$. To describe $\hat{H}_0$ in terms of $|a\rangle$ and $|b\rangle$ states, first equation of $\hat{H}_0$ can be multiplied by $\langle a|$ and the second equation by $\langle b|$, and the resulting equations summed to yield

$$\hat{H}_0(|a\rangle\langle a| + |b\rangle\langle b|) = E_a|a\rangle\langle a| + E_b|b\rangle\langle b|. \tag{3.23}$$

Since only two states are present in this system, the operator $|a\rangle\langle a| + |b\rangle\langle b|$ must equal the unity operator $\hat{I}$, so that Eq.(3.23) simplifies to

$$\hat{H}_0 = E_a|a\rangle\langle a| + E_b|b\rangle\langle b|. \tag{3.24}$$

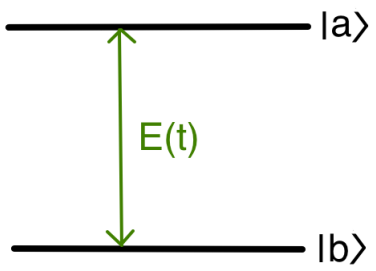

Figure 3.1: A two-level system interacting with an electromagnetic field.

If the interaction Hamiltonian $\hat{H}_I$ is multiplied by the unity operator on both sides, we obtain

$$\hat{H}_I = \hat{I}\hat{H}_I\hat{I} = (|a\rangle\langle a| + |b\rangle\langle b|)(-e\mathbf{r}\cdot\mathbf{E}(t))(|a\rangle\langle a| + |b\rangle\langle b|). \tag{3.25}$$

Expanding $\mathbf{E}(\mathbf{t})$ as $\mathbf{E}(t) = E_x(t)\mathbf{i} + E_y(t)\mathbf{j} + E_z(t)\mathbf{k}$, $\hat{H}_I$ becomes

$$\hat{H}_I = -(\mathbf{d}_{ab}|a\rangle\langle b| + \mathbf{d}_{ba}|b\rangle\langle a|)\cdot\mathbf{E}(t), \tag{3.26}$$

in which $\mathbf{d}_{ab} = \mathbf{d}^*_{ba} = \langle a|ex|b\rangle\mathbf{i} + \langle a|ey|b\rangle\mathbf{j} + \langle a|ez|b\rangle\mathbf{k}$, which assumes that $\langle a|ei|a\rangle = \langle b|ei|b\rangle = 0$, where i is x, y or z. This symmetry applies to atomic gases, in which the potential is symmetric upon inversion but does not necessarily hold for more complex molecular systems. If the field is further taken for simplicity to be x polarized, Eq.(3.26) becomes

$$\hat{H}_I = -\left(d_{ab}|a\rangle\langle b| + d_{ba}|b\rangle\langle a|\right)E_x(t) = -\hat{d}E_x(t), \tag{3.27}$$

with $d_{ab} = d^*_{ba} = \langle a|ex|b\rangle$. For a monochromatic plane wave electric field $E_x(t) = E_0\cos(\omega t)$, the full Hamiltonian in the matrix representation takes the form

$$\hat{H} = \hat{H}_0 + \hat{H}_I = \begin{pmatrix} E_a & -d_{ab}E_0\cos(\omega t) \\ -d^*_{ab}E_0\cos(\omega t) & E_b \end{pmatrix} \tag{3.28}$$

and the decay matrix in the master equation, Eq.(3.22), can be replaced by

$$-\hat{S}\hat{\rho}\hat{S}^\dagger - \frac{1}{2}\{\hat{S}^\dagger\hat{S},\hat{\rho}\} \rightarrow \begin{pmatrix} -\gamma\rho_{aa} & -\frac{\gamma}{2}\rho_{ab} \\ -\frac{\gamma}{2}\rho_{ba} & \gamma\rho_{aa} \end{pmatrix}, \tag{3.29}$$

in which γ is the decay rate from the state $|a\rangle$. Hence

$$\begin{pmatrix} \dot{\rho}_{aa} & \dot{\rho}_{ab} \\ \dot{\rho}_{ba} & \dot{\rho}_{bb} \end{pmatrix} = \begin{pmatrix} -\gamma\rho_{aa} - i\cos(\omega t)(\Omega^*\rho_{ab} - \Omega\rho_{ba}) & (-\frac{\gamma}{2} - iW)\rho_{ab} - i\cos(\omega t)\Omega(\rho_{aa} - \rho_{bb}) \\ (-\frac{\gamma}{2} + iW)\rho_{ba} + i\cos(\omega t)\Omega^*(\rho_{aa} - \rho_{bb}) & \gamma\rho_{aa} - i\cos(\omega t)(\Omega\rho_{ba} - \Omega^*\rho_{ab}) \end{pmatrix}, \tag{3.30}$$

where $W = (E_a - E_b)/\hbar$ and the Rabi frequency Ω equals $\Omega = d_{ab}E_0/\hbar$.

After the transformations $\tilde{\rho}_{ab} = \rho_{ab}e^{i\omega t}$ and $\tilde{\rho}_{ba} = \rho_{ba}e^{-i\omega t}$ Eq.(3.30) becomes

$$\begin{pmatrix} \dot{\rho}_{aa} & \dot{\tilde{\rho}}_{ab} \\ \dot{\tilde{\rho}}_{ba} & \dot{\rho}_{bb} \end{pmatrix} = \begin{pmatrix} -\gamma\rho_{aa} - i\cos(\omega t)(\Omega^*\tilde{\rho}_{ab}e^{-i\omega t} - \Omega\tilde{\rho}_{ba}e^{i\omega t}) & (-\frac{\gamma}{2} + i\Delta)\tilde{\rho}_{ab} - i\cos(\omega t)e^{i\omega t}\Omega(\rho_{aa} - \rho_{bb}) \\ (-\frac{\gamma}{2} - i\Delta)\tilde{\rho}_{ba} + i\cos(\omega t)e^{-i\omega t}\Omega^*(\rho_{aa} - \rho_{bb}) & \gamma\rho_{aa} - i\cos(\omega t)(\Omega\tilde{\rho}_{ba}e^{i\omega t} - \Omega^*\tilde{\rho}_{ab}e^{-i\omega t}) \end{pmatrix}, \tag{3.31}$$

where $\Delta = \omega - W$ is termed the detuning parameter. Inserting $\cos(\omega t) = (e^{-i\omega t} + e^{i\omega t})/2$ into Eq.(3.31) and neglecting the rapidly oscillating terms with frequency 2ω ($e^{\pm 2i\omega t}$) in the rotating

wave approximation (RWA) yields

$$\begin{pmatrix} \dot{\rho}_{aa} & \dot{\tilde{\rho}}_{ab} \\ \dot{\tilde{\rho}}_{ba} & \dot{\rho}_{bb} \end{pmatrix} = \begin{pmatrix} -\gamma\rho_{aa} - \frac{i}{2}(\Omega^*\tilde{\rho}_{ab} - \Omega\tilde{\rho}_{ba}) & (-\frac{\gamma}{2} + i\Delta)\tilde{\rho}_{ab} - \frac{i}{2}\Omega(\rho_{aa} - \rho_{bb}) \\ (-\frac{\gamma}{2} - i\Delta)\tilde{\rho}_{ba} + \frac{i}{2}\Omega^*(\rho_{aa} - \rho_{bb}) & \gamma\rho_{aa} - \frac{i}{2}(\Omega\tilde{\rho}_{ba} - \Omega^*\tilde{\rho}_{ab}) \end{pmatrix}, \tag{3.32}$$

This system of first-order linear differential equations can be solved exactly to find the dynamics of the density operator elements and the Rabi oscillations from which the properties of the dressed states and the AC Stark effect can be explored. However, in the analysis below only the steady state with $\dot{\rho}_{ij} = 0$, which determines quantities such as the susceptibility, is of interest. Imposing the normalization condition $\rho_{aa} + \rho_{bb} = 1$ the density operator elements are

$$\rho_{aa} = \frac{|\Omega|^2}{4\Delta^2 + \gamma^2 + 2|\Omega|^2},$$

$$\rho_{bb} = 1 - \frac{|\Omega|^2}{4\Delta^2 + \gamma^2 + 2|\Omega|^2},$$

$$\tilde{\rho}_{ab} = \frac{2i\Omega(\frac{\gamma}{2} + i\Delta)}{4\Delta^2 + \gamma^2 + 2|\Omega|^2}, \qquad \tilde{\rho}_{ba} = \tilde{\rho}^*_{ab}. \tag{3.33}$$

The electric field $E(t)$ induces a dipole moment between the two levels yielding for the polarization of a single atom

$$\langle\hat{d}\rangle = Tr(\hat{d}\hat{\rho}) = d_{ab}\rho_{ba} + d^*_{ab}\rho_{ab} = d_{ab}\tilde{\rho}_{ba}e^{i\omega t} + d^*_{ab}\tilde{\rho}_{ab}e^{-i\omega t}. \tag{3.34}$$

Multiplying by the atomic density yields for the induced polarization

$$P(t) = N\langle\hat{d}\rangle = N(d_{ab}\tilde{\rho}_{ba}e^{i\omega t} + d^*_{ab}\tilde{\rho}_{ab}e^{-i\omega t}), \tag{3.35}$$

Classically, the polarization induced by an electric field with frequency ω is

$$P(t) = \frac{1}{2}\epsilon_0 E_0(\chi e^{-i\omega t} + \chi^* e^{i\omega t}), \tag{3.36}$$

where χ is the electric susceptibility so that

$$\chi = \frac{2Nd^*_{ab}\tilde{\rho}_{ab}}{\epsilon_0 E_0}. \tag{3.37}$$

Substituting $\tilde{\rho}_{ab}$ from Eq.(3.33) and employing $\Omega = d_{ab}E_0/\hbar$, yields for the susceptibility of the two-level system

$$\chi = \frac{4iN|d_{ab}|^2}{\epsilon_0\hbar}\frac{\frac{\gamma}{2}+i\Delta}{4\Delta^2+\gamma^2+2|\Omega|^2}. \tag{3.38}$$

which, however is only valid for $\Omega << 1$ since the linear approximation was employed. The susceptibility is plotted in Fig.(3.2) with $4N|d_{ab}|^2/(\epsilon_0\hbar) = \gamma$ and $\Omega = 0.1\gamma$ where γ is an arbitrary scaling constant.

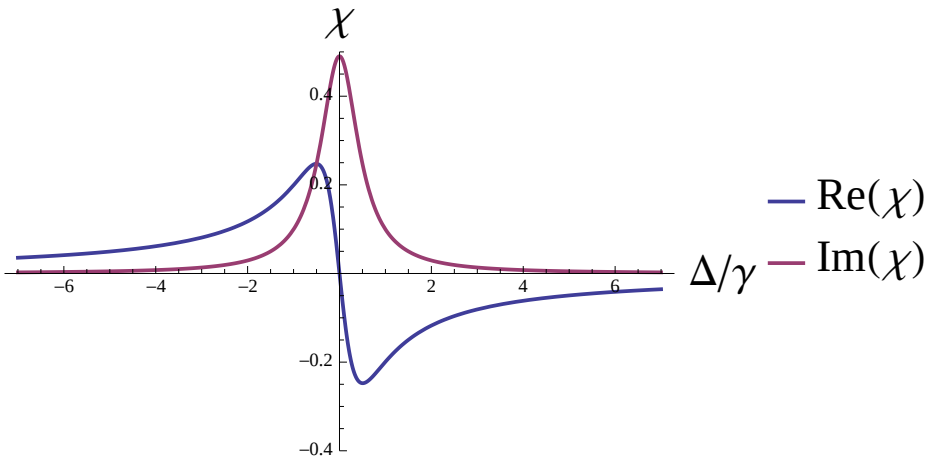

Figure 3.2: The real (blue) and imaginary (red) part of the two-level susceptibility, χ, of Eq.(3.38)

This figure resembles the classical Lorentz model of dielectrics. As we can see, the real part of $\chi' = Re(\chi)$ is mostly increasing for all values of Δ, which is expected for the two-level systems given the absence of magnetic and other interactions. Additionally, the susceptibility generally increases with the detuning Δ which is termed normal dispersion except in the anomalous dispersion region near $\Delta = 0$, which is mostly associated with slow light and other phenomena. However, in this region the absorption, $\chi'' = Im(\chi)$ is large. To suppress this absorption in the anomalous region requires more complicated systems such as those presented in this and the following chapter.

3.2 Negative refraction index of dense gases

Dense gases can exhibit negative refraction if the magnetic susceptibility is enhanced such that it becomes comparable to the electric susceptibility. This can be achieved by various techniques including electromagnetically induced transparency (left- or right-handedness) [55–62] and chirality [63–67]. In such cases, dense atomic gases can exhibit a negative refractive index accompanied by

minimal absorption [68].

The concept of employing atomic coherence to modify the refractive index of a gas while maintaining near-zero absorption was first advanced by Scully [69], who observed that atomic coherence can be employed in different atomic systems to suppress the absorption through quantum destructive interference, a procedure which clearly lacks a classical counterpart. This and related techniques have subsequently been advanced by many researchers [63, 68, 70] to manipulate the electric and magnetic properties of atomic systems while suppressing absorption. For example in 2016 Zubairy et. al. obtained a negative refractive index over a large frequency range with zero absorption in a 4 level atomic cascade interacting with the electric and magnetic components of a probe field in a dense gas [71]. Here this procedure is extended to a system in which the probe field and a second low-intensity field induce a negative refraction with a large magnitude through coherent superposition. We find further, rather unexpectedly, that by changing either the ratio of the two magnetic amplitudes of the two fields or the phase of the atomic coherence, the magnitude of the negative refractive index can be easily controlled while simultaneously suppressing absorption.

3.3 Analytic formulation of the 5-level scheme

We consider the 5 level atomic system represented by Fig.(3.3). The levels $|5\rangle$, $|4\rangle$, $|3\rangle$, and $|1\rangle$ possess identical parities that are the opposite of the parity of $|2\rangle$. Consequently, electric-dipole transition between $|5\rangle - |3\rangle$ and $|4\rangle - |3\rangle$ are forbidden, but magnetic-dipole transitions are allowed. The level energies are denoted $E_i = \hbar\omega_i, i = 1, 2, \ldots 5$, with decay rates γ_i. The electric component of the probe field Ω_{EP} couples $|3\rangle - |2\rangle$, while the magnetic component Ω_{BP} couples $|5\rangle - |3\rangle$.

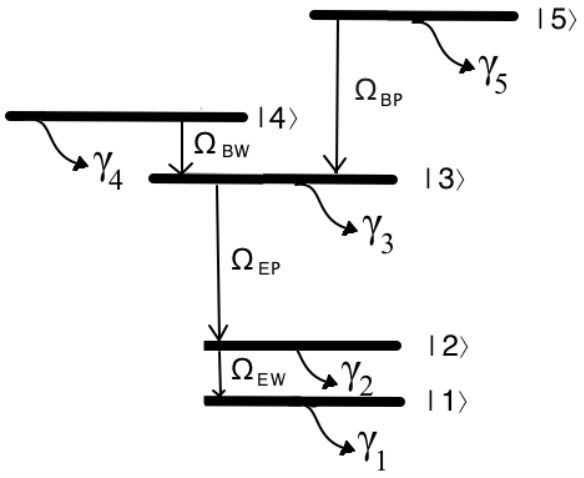

Figure 3.3: The five level system

A second low-intensity auxiliary field further couples $|2\rangle - |1\rangle$ through its electric component Ω_{EW} and $|4\rangle - |3\rangle$ through its magnetic component Ω_{BW}. Such a system could possibly occur in, for example, neon gas, in which $|1\rangle$ to $|4\rangle$ are present in an isolated system while $|5\rangle$ could be generated in the presence of an applied magnetic field by the anomalous Zeeman effect, which splits $|4\rangle$ into two levels by an amount proportional to the applied field.

If $|4\rangle$ and $|5\rangle$ are coherently excited, the initial density operator can be expressed as

$$\hat{\rho}^{(0)} = \sum_{i=1}^{5} \rho_{ii}^{(0)} |i\rangle\langle i| + \rho_{45}^{(0)} |4\rangle\langle 5| + \rho_{54}^{(0)} |5\rangle\langle 4|, \tag{3.39}$$

where the coefficients $\rho_{ii}^{(0)}$ represent the initial atomic population of each level, while $\rho_{45}^{(0)}$ and $\rho_{54}^{(0)}$ parametrize the coherence between the levels $|4\rangle$ and $|5\rangle$. This atomic coherence can be generated with many techniques including coherent pulse excitation [72], Raman- induced coherence [73], and adiabatic population conversion [74]. The atomic coherence in Eq.(3.39) leads to quantum destructive interference [69] between the two paths of our scheme ($|5\rangle - |3\rangle$) and ($|4\rangle - |3\rangle$) that cancels or reduces the probe field absorption. Consequently, the initial atomic populations in the exited states are assumed to be sufficiently large that both $\rho_{55}^{(0)} + \rho_{44}^{(0)} > \rho_{11}^{(0)}$ and $\rho_{45}^{(0)} \approx \rho_{44}^{(0)} \approx \rho_{55}^{(0)}$, so that the atom is at the start of the calculation with high probability in the excited states $|4\rangle$ and $|5\rangle$.

The system Hamiltonian in the interaction picture after applying the rotating wave approximation (RWA) and the dipole approximation adopts the form

$$\hat{H} = \hbar \left[\sum_{i=0}^{5} \omega_i |i\rangle\langle i| - \frac{\Omega_{EW}}{2} e^{i\Delta_1 t} |2\rangle\langle 1| - \frac{\Omega_{EP}}{2} e^{i\Delta_2 t} |3\rangle\langle 2| - \frac{\Omega_{BW}}{2} e^{i\Delta_3 t} |4\rangle\langle 3| - \frac{\Omega_{BP}}{2} e^{i\Delta_4 t} |5\rangle\langle 3| + H.C. \right], \tag{3.40}$$

in which $\Delta_1 = \omega_2 - \omega_1 - \omega_W$, $\Delta_2 = \omega_3 - \omega_2 - \omega_P$, $\Delta_3 = \omega_4 - \omega_3 - \omega_W$, and $\Delta_4 = \omega_5 - \omega_3 - \omega_P$. Additionally, ω_P and ω_W represent the probe and auxiliary field frequencies. The Ω variables represent the Rabi frequencies, terms of the electric and magnetic amplitudes of the probe field ξ_{EP} and ξ_{BP}, and the auxiliary field, ξ_{EW} and ξ_{BW} are given by $\Omega_{EW} = \frac{|d_{21}|\xi_{EW}}{\hbar}$, $\Omega_{EP} = \frac{|d_{32}|\xi_{EP}}{\hbar}$, $\Omega_{BW} = \frac{|\mu_{43}|\xi_{BW}}{\hbar}$, and $\Omega_{BP} = \frac{|\mu_{53}|\xi_{BP}}{\hbar}$. The electric and magnetic dipole moments of each transition are then defined as $d_{21} = |\langle 2|\hat{d}_1|1\rangle|$, $d_{32} = |\langle 3|\hat{d}_2|2\rangle|$, $\mu_{43} = |\langle 4|\hat{\mu}_1|3\rangle|$, and $\mu_{53} = |\langle 5|\hat{\mu}_2|3\rangle|$. The first term of Eq.(3.40) describes the atomic energy levels in the absence of an incident field while the remaining terms model the interactions between the atom and different components of the probe and auxiliary fields present in Fig.(3.3).

The Master equation Eq.(3.22) of the five level system can be written in the form

$$\dot{\hat{\rho}} = -\frac{i}{\hbar}[\hat{H}, \hat{\rho}] - \frac{1}{2}\{\hat{\Gamma}, \hat{\rho}\} + r_P \hat{\rho}^{(0)}. \tag{3.41}$$

Here $\hat{\Gamma}$ is the decay matrix defined as $\langle i|\hat{\Gamma}|j\rangle = \delta_{ij}\gamma_i$ and r_P represents the rate at which the atoms are pumped by the coherent excitation between the levels $|4\rangle$ and $|5\rangle$. The steady state atomic response to the incident fields is then obtained as the solution of the Master equation. An approximation to this time-independent solution for the Hamiltonian of Eq.(3.41) is given in the following section.

3.4 Approximate solution

While the Master equation, Eq.(3.41) represents 25 equations since, however $\rho_{ij} = \rho_{ji}^*$, only the equations associated with the upper off-diagonal elements of the matrix must be considered. Further, the zeroth-order values of all Ω variables are employed to construct the diagonal components of the density matrix ρ_{ii}, as Ω magnitudes are far smaller than those of both γ_i and r_P. Accordingly, the diagonal elements in the master equation can be approximated as

$$\rho_{ii} = \frac{r_P \rho_{ii}^{(0)}}{\gamma_i}. \quad i = 1, \cdots 5 \tag{3.42}$$

Thus we left with 10 equations of the upper off-diagonal elements. After applying the rotating frame transformation these equations adopt the form

$$\dot{\tilde{\rho}}_{12} = [-\gamma_{12} + i(\omega_{21} - \Delta_1)]\tilde{\rho}_{12} + \frac{i}{2}[\Omega_{EW}(\rho_{22} - \rho_{11}) - \Omega^*_{EP}\tilde{\rho}_{13}]. \tag{3.43}$$

$$\dot{\tilde{\rho}}_{13} = [-\gamma_{13} + i(\omega_{31} - \Delta_1 - \Delta_2)]\tilde{\rho}_{13} + \frac{i}{2}[\Omega_{EW}\tilde{\rho}_{23} - \Omega_{EP}\tilde{\rho}_{12} - \Omega^*_{BW}\tilde{\rho}_{14} - \Omega^*_{BP}\tilde{\rho}_{15}]. \tag{3.44}$$

$$\dot{\tilde{\rho}}_{14} = [-\gamma_{14} + i(\omega_{41} - \Delta_1 - \Delta_2 - \Delta_3)]\tilde{\rho}_{14} + \frac{i}{2}[\Omega_{EW}\tilde{\rho}_{24} - \Omega_{BW}\tilde{\rho}_{13}]. \tag{3.45}$$

$$\dot{\tilde{\rho}}_{15} = [-\gamma_{15} + i(\omega_{51} - \Delta_1 - \Delta_2 - \Delta_4)]\tilde{\rho}_{15} + \frac{i}{2}[\Omega_{EW}\tilde{\rho}_{25} - \Omega_{BP}\tilde{\rho}_{13}]. \tag{3.46}$$

$$\dot{\tilde{\rho}}_{23} = [-\gamma_{23} + i(\omega_{32} - \Delta_2)]\tilde{\rho}_{23} + \frac{i}{2}[\Omega^*_{EW}\tilde{\rho}_{13} + \Omega_{EP}(\rho_{33} - \rho_{22}) - \Omega^*_{BW}\tilde{\rho}_{24} - \Omega^*_{BP}\tilde{\rho}_{25}]. \tag{3.47}$$

$$\dot{\tilde{\rho}}_{24} = [-\gamma_{24} + i(\omega_{42} - \Delta_2 - \Delta_3)]\tilde{\rho}_{23} + \frac{i}{2}[\Omega^*_{EW}\tilde{\rho}_{14} - \Omega_{BW}\tilde{\rho}_{23} + \Omega_{EP}\tilde{\rho}_{34}]. \tag{3.48}$$

$$\dot{\tilde{\rho}}_{25} = [-\gamma_{25} + i(\omega_{52} - \Delta_2 - \delta_4)]\tilde{\rho}_{25} + \frac{i}{2}[\Omega^*_{EW}\tilde{\rho}_{15} - \Omega_{BP}\tilde{\rho}_{23} + \Omega_{EP}\tilde{\rho}_{35}]. \tag{3.49}$$

$$\dot{\tilde{\rho}}_{34} = [-\gamma_{34} + i(\omega_{43} - \Delta_3)]\tilde{\rho}_{34} + \frac{i}{2}[\Omega^*_{BW}(\rho_{44} - \rho_{33}) + \Omega^*_{EP}\tilde{\rho}_{24} + \Omega_{BP}\tilde{\rho}_{54}]. \tag{3.50}$$

$$\dot{\tilde{\rho}}_{35} = [-\gamma_{35} + i(\omega_{53} - \Delta_4)]\tilde{\rho}_{35} + \frac{i}{2}[\Omega_{BP}(\rho_{55} - \rho_{33}) + \Omega_{BW}\tilde{\rho}_{45} + \Omega^*_{EP}\tilde{\rho}_{25}]. \tag{3.51}$$

$$\dot{\tilde{\rho}}_{45} = [-\gamma_{45} + i(\omega_{54} - \Delta_4 + \Delta_3)]\tilde{\rho}_{45} + \frac{i}{2}[\Omega^*_{BW}\tilde{\rho}_{35} - \Omega_{BP}\tilde{\rho}_{43}] + r_P\tilde{\rho}^{(0)}_{45}. \tag{3.52}$$

In the above equation, $\omega_{ji} \equiv \omega_j - \omega_i$, $\gamma_{ij} = (\gamma_i + \gamma_j)/2$, and $\tilde{\rho}_{ij}$ represents the ijth density matrix element in the rotating frame. Since in the present model Ω_{EW}, Ω_{BW}, Ω_{EP}, and Ω_{BP} are taken to be far smaller than $\ll \gamma_i$, while the pumping rate r_P and ω_i's are further assumed to greatly exceed the Rabi frequencies of the two fields, the above equations are solved only to first order for all Ω variables while the diagonal elements are independent of these variables as in Eq.(3.42). In the steady state the time derivatives vanish so that $\dot{\tilde{\rho}}_{ij} = 0$. Additionally, only the behavior of the probe field is of interest which is described by the two density matrix elements ρ_{35} and ρ_{23}. With these approximations, Eq.(3.43-3.52) yields

$$\tilde{\rho}_{35} = \frac{ir_P}{2(-\gamma_{35} + i(\Delta_P + \omega_{53}))}\left[\frac{\tilde{\rho}^{(0)}_{45}\Omega_{BW}}{-\gamma_{45} + i(\Delta_P - \Delta_W + \omega_{54})} - \Omega_{BP}\left(\frac{\rho^{(0)}_{55}}{\gamma_5} - \frac{\rho^{(0)}_{33}}{\gamma_3}\right)\right], \tag{3.53}$$

and

$$\tilde{\rho}_{23} = -\frac{ir_P\Omega_{EP}}{2(-\gamma_{23} + i(\Delta_P + \omega_{53}))}\left(\frac{\rho_{33}^{(0)}}{\gamma_3} - \frac{\rho_{22}^{(0)}}{\gamma_2}\right), \tag{3.54}$$

in which $\Delta_P \equiv \omega_P - \omega_{53}$, and $\Delta_W \equiv \omega_W - \omega_{43}$.

Note that the atomic coherence $\tilde{\rho}_{45}^{(0)}$ can change the sign of $\tilde{\rho}_{35}$ while for zero coherence $\tilde{\rho}_{45}^{(0)} = 0$, implying that negative refraction cannot be achieved in the absence of absorption. As well, the model effectively describes the interaction of 3 level system composed of $|3\rangle$, $|4\rangle$ and $|5\rangle$ with the two subsystems $|3\rangle - |2\rangle$ and $|2\rangle - |1\rangle$, hence the parameters associated with the level $|1\rangle$ as well as the Rabi frequency Ω_{EW} are absent. The small magnitude of the auxiliary and probe fields together with the restriction of the calculation to the properties of the probe field is responsible for the absence of interaction between the levels $|2\rangle$ and $|1\rangle$ in Eq.(3.53) and Eq.(3.54). The electric polarization and the magnetization of an atom generated by the probe field can be written as $p = d_{32}\rho_{23}e^{-i\omega_P t} + c.c.$ and $m = \mu_{35}\rho_{53}e^{-i\omega_P t} + c.c.$, respectively, identifying the positive part of the probe field with the classical expressions for the electric and magnetic response yields

$$d_{32}\tilde{\rho}_{23} = \chi_e\epsilon_0\xi_{EP}/2, \tag{3.55}$$

and

$$\mu_0\mu_{35}\tilde{\rho}_{53} = \chi_m\epsilon_0\xi_{BP}/2, \tag{3.56}$$

in which χ_e and χ_m represent the electric and magnetic susceptibilities. Accordingly, since $d_{ij} = d_{ji}^*$, $\mu_{ij} = \mu_{ji}^*$, and introducing the ratio of the two magnetic amplitudes $S = \xi_{BW}/\xi_{BP}$

$$\chi_e = -\frac{i|d_{32}|^2 r_P}{\epsilon_0\hbar(-\gamma_{23} + i(\Delta_P + \omega_{53}))}\left(\frac{\rho_{33}^{(0)}}{\gamma_3} - \frac{\rho_{22}^{(0)}}{\gamma_2}\right), \tag{3.57}$$

$$\chi_m = \frac{i\mu_0 r_P}{\hbar(-\gamma_{35} + i(\Delta_P + \omega_{53}))}\left[\frac{S\tilde{\rho}_{45}^{(0)}|\mu_{43}||\mu_{53}|}{-\gamma_{45} + i(\Delta_P - \Delta_W + \omega_{54})} - |\mu_{53}|^2\left(\frac{\rho_{55}^{(0)}}{\gamma_5} - \frac{\rho_{33}^{(0)}}{\gamma_3}\right)\right], \tag{3.58}$$

The parameter S, which multiplies by the atomic coherence, can equal any positive value resulting in either an amplification or a reduction of atomic coherence effects. Hence under the condition that the auxiliary field possesses a sufficiently small amplitude, the atomic coherence can be easily be adjusted experimentally by varying S without affecting the atomic system.

Since we have a dense atomic gas, we cannot just multiply the dipole elements directly by N as we did in the two-level scheme. Therefore, the electric permittivity and the magnetic permittivity

of atomic dense gases can be calculated from the Clausius and Mossotti relations [75]

$$\epsilon = \epsilon_r + i\epsilon_i = \frac{1 + \frac{2}{3}N\chi_e}{1 - \frac{1}{3}N\chi_e}, \tag{3.59}$$

$$\mu = \mu_r + i\mu_i = \frac{1 + \frac{2}{3}N\chi_m}{1 - \frac{1}{3}N\chi_m}, \tag{3.60}$$

in which N is the density of the atoms in the dense gas. This relation is derived by considering the local fields of the dense atomic gases. Negative values of χ_m and χ_e accordingly can yield negative permittivities and/or permeabilities. The refractive index is obtained from the (typically complex) values of ϵ and μ through [76]

$$n_r = -\frac{1}{\sqrt{2}}\sqrt{|\epsilon||\mu| + \mu_r\epsilon_r - \mu_i\epsilon_i}, \tag{3.61}$$

$$n_i = -\frac{1}{\sqrt{2}}\frac{\mu_i\epsilon_r + \mu_r\epsilon_i}{\sqrt{|\epsilon||\mu| + \mu_r\epsilon_r - \mu_i\epsilon_i}}. \tag{3.62}$$

which require

$$\epsilon_r|\mu| + \mu_r|\epsilon| < 0 \tag{3.63}$$

This last relation must accordingly be verified before applying Eqs.(3.61,3.62). If it does not hold, we need to replace the negative front sign of Eqs.(3.61, 3.62) to positive. In general, if this inequality is correct for a system, then that system will possess negative refractive index. Also, note that Eq.(3.63) is always greater than or equal to zero for a nonmagnetic material, in which $\mu_r = p, \mu_i = 0$, where p is any positive value. This fact indicates that the negative refractive index requires a material with both electric and magnetic responses.

3.5 Results

Having developed the underlying equations, Eqs.(3.59,3.60,3.61,3.62), in this section the functional dependence of the refractive index and absorption on the amplification parameter S will be determined. The atomic parameters employed are similar to those suggested by previous authors [56, 71]. Namely, the atomic decay rates are set to $\gamma_2 = 2\gamma$, $\gamma_3 = \gamma$, and $\gamma_4 = \gamma_5 = 2\gamma$, with $\gamma = 10^7$ Hz, the atomic density $N = 8 * 10^{23} m^{-3}$, and the dipole moments are calculated for the infrared spectrum with $|\mu_{53}| = 1.457 * 10^{-21}$, $|\mu_{43}| = 7.572 * 10^{-21}$ and $|d_{32}| = 6.659 * 10^{-28}$. The interlevel spacings

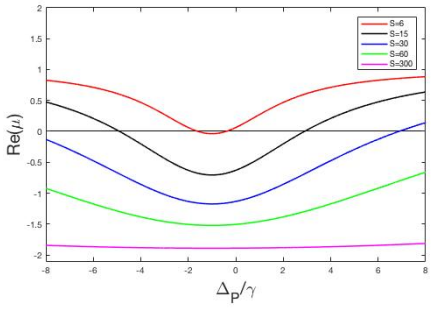

(a) The real part of μ.

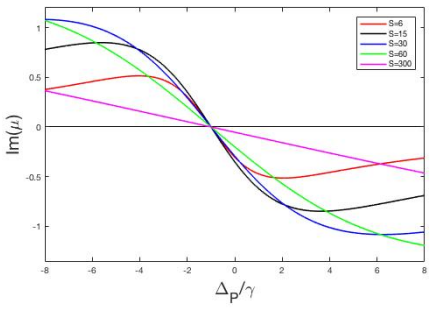

(b) The imaginary part of μ.

Figure 3.4: The real and imaginary parts of μ for different values of S, where the (red) curve for $S = 6$, the (black) curve for $S = 15$, the (blue) curve for $S = 30$, the (green) curve for $S = 60$, and the (magenta) curve for $S = 300$.

between $|5\rangle$ and $|4\rangle$ and between $|5\rangle$ and $|3\rangle$ are further taken as $\omega_{54} = 2\gamma$ and $\omega_{53} = 0.001\gamma^2$ while $r_P = 2\gamma$. The atomic system is assumed to be initially in a combination of exited states, with populations $\rho_{55}^{(0)} = \rho_{44}^{(0)} = 0.25$, $\rho_{33}^{(0)} = 0.1$, $\rho_{22}^{(0)} = 0.05$, and $\rho_{11}^{(0)} = 1 - \rho_{22}^{(0)} - \rho_{33}^{(0)} - 2\rho_{44}^{(0)} = 0.35$ together with a maximum value of the atomic coherence $\rho_{45}^{(0)} = (\rho_{44}^{(0)} + \rho_{55}^{(0)})/2 = 0.25$.

Considering first the variation of the real and imaginary parts of the electric permittivity with the probe field detuning, Δ_P, indicates that $\epsilon_r \approx -2$ and $\epsilon_i \approx 0$ for $-8\gamma < \Delta_P < 8\gamma$. This indicates that the local field of the dense gas gives the principal contribution to the total electric field. Fig.(3.4) next displays the dependence of μ on S for $\Delta_W = 0$. Evidently the real and imaginary parts of μ become nearly independent of Δ_P as the coherence amplification factor S increases. Further, from Fig.(3.4a) the real parts of both μ and ϵ are negative over a wide range of Δ_P, which is in fact the principal source of the observed negative refraction.

Fig.(3.5) plots the variation of the real and imaginary values of the refractive index with S and Δ_P for $\Delta_W = 0$. Clearly this figure demonstrates that, as a result of the amplification of the atomic coherence for large values of S, when $S \approx 300$, the real component of the refractive index is effectively independent of Δ_P and approaches -2 while its imaginary component approaches 0. Indeed for large S, the real and imaginary refractive indices are not only largely unaffected by the value of Δ_P, but are also nearly independent of γ_5 and most of the other parameters in the calculation. That the negative refraction is largely unaffected by the field and the atomic parameters could prove highly significant in applications that require both a stable n value and negligible absorption.

Figs.(3.5a,3.5b) illustrate the dependence of the real and imaginary values of the refraction

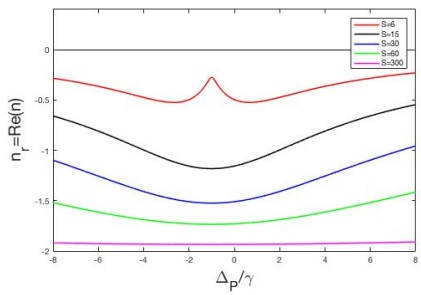

(a) Re(n), $\gamma_5 = 2\gamma$

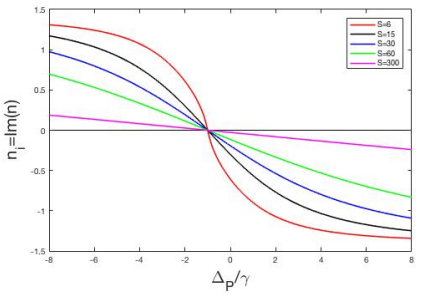

(b) Im(n), $\gamma_5 = 2\gamma$

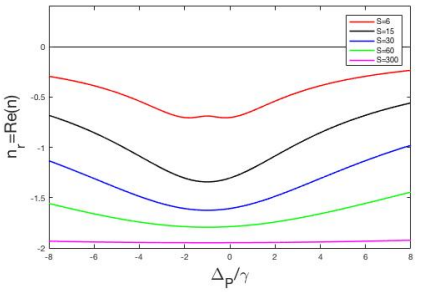

(c) Re(n), $\gamma_5 = \gamma$

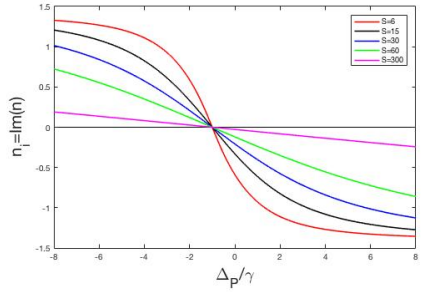

(d) Im(n), $\gamma_5 = \gamma$

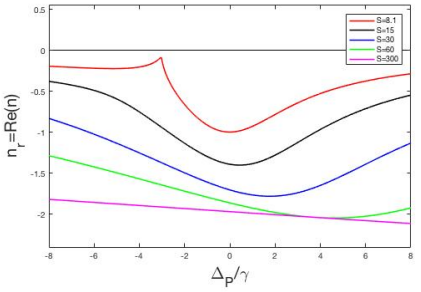

(e) Re(n), $\rho_{45}^{(0)} = |\rho_{45}^{(0)}|e^{i\pi/4}$

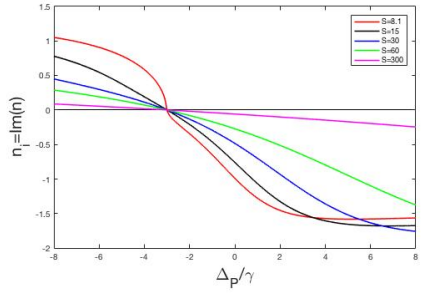

(f) Im(n), $\rho_{45}^{(0)} = |\rho_{45}^{(0)}|e^{i\pi/4}$

Figure 3.5: The real and imaginary parts of n for different values of S,γ_5, and $\rho_{45}^{(0)}$, where the (red) curves for $S = 6$, the (black) curves for $S = 15$, the (blue) curves for $S = 30$, the (green) curves for $S = 60$, and the (magenta) curve for $S = 300$. The (red) curve in the last two figures (e) and (f) with $S = 8.1$.

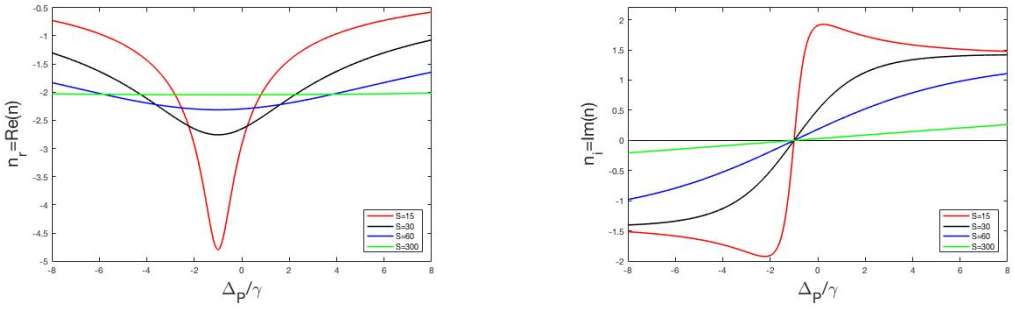

Re(n) Im(n)

Figure 3.6: The real and imaginary parts of n for different values of S and $\rho_{45}^{(0)} = |\rho_{45}^{(0)}|e^{i\pi}$. The (red) curves for $S = 15$, the (black) curves for $S = 30$, the (blue) curves for $S = 60$, and the (green) curves for $S = 300$.

index n for $\gamma_5 = 2\gamma$ for different values of S on the detuning Δ_P while Figs.(3.5c,3.5d) employ identical parameters but with $\gamma_5 = \gamma$. Evidently in Figs.(3.5a, 3.5b, 3.5c, 3.5d) for $\Delta_P \approx -\gamma$, the absorption is close to zero and independent of S, suggesting a simple procedure for modulating the negative refraction index without inducing an appreciable degree of absorption. Figs.(3.5e,3.5f) further quantify the influence of the atomic coherence on the refractive index by the initial value of $\rho_{45}^{(0)}$ to $|\rho_{45}^{(0)}|e^{i\pi/4}$, with $\gamma_5 = 2\gamma$. An interesting feature around the similarly for a probe detuning of $\approx -3\gamma$, as apparent from Figs.(3.5e,3.5f), the negative refractive index can be modulated by varying S without inducing absorption as discussed in the context of the previous figures.

To quantify the effect of the coherent phase for phases larger than or equal π, Fig.(3.6) displays n for different S values with an atomic coherence set to $|\rho_{45}^{(0)}|e^{i\pi}$. For $S = 15$ the refractive index is close to -4.8 for $\Delta_P \approx -\gamma$ which corresponds to the minimum refractive index for which the absorption is nearly zero. The refractive index for $n > -2$ is dependent on S when the phase of the atomic coherence equals zero while the refractive index for large negative values $n < -2$ can be modulated by varying the phase of $\rho_{45}^{(0)}$ and S. This effect can also be observed in Fig.(3.7) which plots n and the absorption for $S = 15$ as a function of the phase of the atomic coherence, ϕ, where $\rho_{45}^{(0)} = |\rho_{45}^{(0)}|e^{i\phi}$. Evidently the magnitude of the negative refractive index increases as ϕ approaches 1.25π while the absorption vanishes. Conversely, as n becomes more negative the absorption rapidly increases. Accordingly, a wide range of negative n values can clearly be realized for which the absorption is negligible.

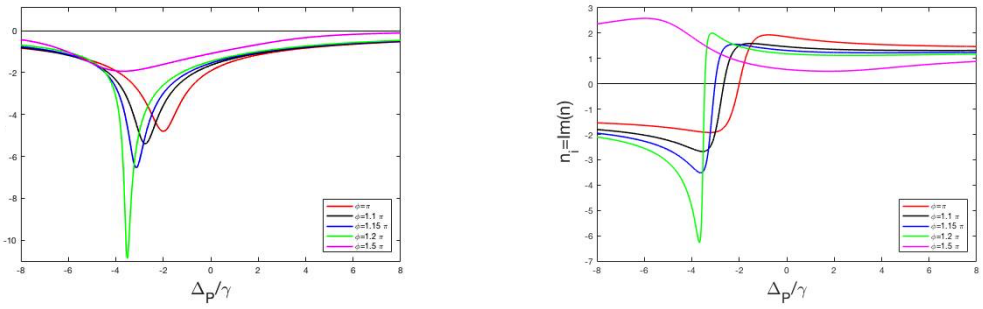

Re(n) Im(n)

Figure 3.7: The real and imaginary parts of n for different values of ϕ, the phase of the atomic coherence $\rho_{45}^{(0)} = |\rho_{45}^{(0)}|e^{i\phi}$. The value of S here is fixed to 15. The (red) curve is for $\phi = \pi$, the (black) curve is for $\phi = 1.1\pi$, the (blue) curve is for $\phi = 1.15\pi$, the (green) curve is for $\phi = 1.2\pi$, and the (magenta) curve for $\phi = 1.5\pi$.

3.6 Conclusion

Varying S in our procedure provides a simpler procedure for controlling the negative refractive index than competing techniques. For example, in [64], the negative refraction index is altered by varying some of the parameters present in a 5-level scheme. This however requires four fields of which two or more require high intensity. Additionally, the detuning does not cover the entire range from -2 to near zero in most cases unlike the procedure of this paper, c.f Figs.(3.5a and 3.5e)). In contrast the method proposed here requires only two weak fields, and for sufficiently large S stablizes the negative refractive index to a value close to -2 while insuring near zero absorption over a wide range of Δ_P.

Thus in this chapter we have demonstrated that in a 5 level atomic system interacting with two incoming fields in a dense gas the influence of the atomic coherence on the real and imaginary parts of the refractive index can be amplified by appropriately specifying the ratio S of the magnetic amplitudes of the incoming fields. Hence the negative refractive index can be modulated while maintaining a small value of the absorption. Accordingly, this procedure or an appropriate modification could be relevant to practical implementations of negative refractive index materials. In the future this work could be extended into the nonlinear, strong field regime. Further, although the results here assume a large initial atomic excitation, a smaller excitation population could also yield identical behavior if the atomic coherence is suitably amplified through a larger value of S.

Chapter 4

Double Λ Scheme in a White Light Cavity

Optical switches have replaced electronic switches in numerous applications, including optical communications, internet traffic, quantum information processing and quantum networking. Switches have been designed to detect gravitational-waves through a signal recycling mirror (SRM) [77, 78] and to Q switch lasers through electro and acousto optic switches [79, 80] as well as rotating mirrors [81]. In quantum mechanics, optical switches can to control entanglement in trapped qubits [82], in quantum circuits and quantum networks [83–85].

In the previous chapter, the semi-classical theory of light-matter interactions was employed to to calculate the refractive index. In this chapter, we realize optical switching by applying the same approach to a different atomic system. In particular, placing a material inside an optical cavity alters its transmission, and reflection spectrum near the cavity resonant frequencies. Hence by properly specifying the material and cavity properties the transmission spectrum can be appropriately engineered, resulting in an optical switch.

Here we exclusively study the double Λ scheme. If this system is applied in a cavity with two applied light fields, more than one white light region can be generated and modulated or switched. The chapter first reviews the Fabry-Pérot cavities, and presents the details of the double Λ scheme which is subsequently analyzed semi-classically. After presenting several possible techniques for modulating the transmission spectrum possible avenues for future research are suggested.

4.1 Background

This chapter concerns the evaluation of the transmission and reflection spectrum of a Fabry-Pérot cavity in the presence of the fields and atomic states shown in Fig.(4.1). Both sides of the cavity are assumed to be terminated with mirrors with zero absorption and amplitude transmission and reflection coefficients denoted by t and r that satisfy $r^2 + t^2 = 1$. For the electromagnetic fields we assume monochromatic plane waves

$$E_{in} = E_0 e^{-i\omega t + ikz}, \tag{4.1}$$

and employ the scalar approximation. The lossless medium within the cavity is described by a real refractive index n while the cavity is assumed surrounded by vacuum.

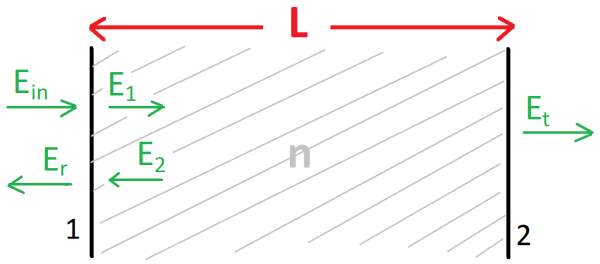

Figure 4.1: The interacting fields within the Fabry-Pérot cavity.

Referring to Fig.(4.1), the field E_1 upon reflecting from mirror 2 generates a reflected field

$$E_2 = rE_1 e^{2ikL}. \tag{4.2}$$

and the transmitted amplitude E_t

$$E_t = tE_1 e^{ikL}. \tag{4.3}$$

Hence

$$E_1 = t'E_{in} + rE_2. \tag{4.4}$$

while the reflected amplitude E_r can similarly be described as

$$E_r = r'E_{in} + tE_2, \tag{4.5}$$

where r' and t' are the coefficients of the mirrors when the incident field is outside the cavity. The relations between these different coefficients are

$$tt' + r^2 = 1, \qquad r = -r'. \tag{4.6}$$

which can easily be verified from the dielectric interference equations (Fresnel equations). Eqs.(4.2) and (4.4) yield

$$\frac{E_1}{E_{in}} = \frac{t'}{1 - r^2 e^{2ikL}}. \tag{4.7}$$

while Eq.(4.3) and Eq.(4.7) imply

$$\frac{E_t}{E_{in}} = \frac{tt' e^{ikL}}{1 - r^2 e^{2ikL}} = \frac{T e^{ikL}}{1 - r^2 e^{2ikL}}, \tag{4.8}$$

where T represents the power transmission coefficient $T = tt' = t^2$ and the field intensity is given by

$$I = \frac{1}{2}\epsilon_o nc|E|^2. \tag{4.9}$$

The light transmitted through and measured in the vacuum outside the cavity is then $T_{cav}(\omega)$ obtained by multiplying Eq.(4.8) with its conjugate part

$$T_{cav}(\omega) = \frac{I_t}{I_{in}} = \left|\frac{E_t}{E_{in}}\right|^2 = \left|\frac{T e^{ikL}}{1 - r^2 e^{2ikL}}\right|^2 = \frac{T^2}{T^2 + 4R\sin(kL)^2}, \tag{4.10}$$

where $R = r^2$. The cavity reflection, $R_{cav}(\omega)$ is then obtained from Eqs.(4.5, 4.2) and Eq.(4.7). The result finally reads

$$R_{cav}(\omega) = \frac{I_r}{I_{in}} = \left|\frac{E_r}{E_{in}}\right|^2 = \left|\frac{r(1 - e^{2ikL})}{1 - r^2 e^{2ikL}}\right|^2 = \frac{4R\sin(kL)^2}{T^2 + 4R\sin(kL)^2}. \tag{4.11}$$

Note that $T_{cav}(\omega)$ and $R_{cav}(\omega)$ satisfy the energy conservation law $R_{cav}(\omega) + T_{cav}(\omega) = 1$ since the mirrors and the medium are lossless. For medium with absorption or gain the wave vector is complex $k = k_r + ik_i$ and the cavity transmission and reflection coefficients are instead

$$T_{cav}(\omega) = \left|\frac{T e^{ikL}}{1 - R e^{2ikL}}\right|^2, \qquad R_{cav}(\omega) = \left|\frac{\sqrt{R}(1 - e^{2ikL})}{1 - R e^{2ikL}}\right|^2. \tag{4.12}$$

Fig.(4.2) displays the cavity transmission spectrum $T_{cav}(\omega)$ as a function of R where T are calculated from $T = 1 - R$.

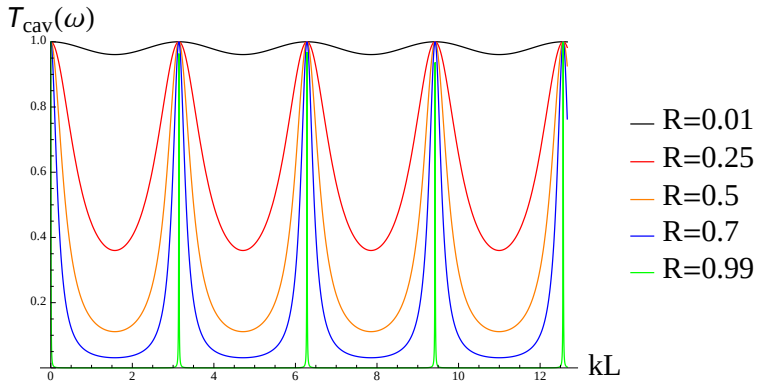

Figure 4.2: The cavity transmission coefficient $T_{cav}(\omega)$ of the Fabry-Pérot cavity as a function of R.

From the figure, we can see that for all values of R, the cavity transmission reach 1 for some certain values of kL. These values are called the resonant wave vectors (frequencies) which equal

$$k_m L = m\pi, \qquad m = 0, \pm 1, \pm 2, \pm 3, \cdots \tag{4.13}$$

We also can see for small values of R, the spectrum tends to be closer to 1 in all values of kL. This behavior is expected because in this limit the cavity cannot save the light for a long time, but instead, the light shortly escapes from the cavity, so the cavity appears to be closer to the vacuum. In the opposite limit when R becomes close to unity, the line shapes become very narrow. In this limit, the cavity is highly resonant, and almost for all values of kL, the destructive interference occurs. Except in the resonant values where constructive interference occurs.

If a material of a refractive index n is present inside the cavity so that $k = \omega n/c$ the resonant frequencies become

$$\omega_m \mathrm{Re}(n) = \frac{m\pi c}{L}, \qquad m = 0, \pm 1, \pm 2, \pm 3, \cdots \tag{4.14}$$

which indicates that while the resonant wave vectors in Eq.(4.13) are unaltered the resonant frequencies ω_m differ.

Accordingly, a cavity can alter the transmission and reflection spectrum of a given medium, which is clear even for an empty cavity for which the transmission spectrum is described by Fig.(4.2). In the next section, we therefore examine the transmission spectrum of a cavity filled with two-level atoms.

4.1.1 Two-level system

While in the previous chapter the susceptibility of the two-level system was evaluated in Eq.(3.38), to obtain the cavity transmission coefficient, the refractive index must additionally be obtained as a function of χ. Recalling that the electric displacement field is given by $D = \epsilon_0 E + P = \epsilon_0(1+\chi)E = \epsilon_0 \epsilon E$, where ϵ is the relative dielectric constant. Comparing the two expressions yields

$$1 + \chi = \epsilon. \tag{4.15}$$

Let us now specify the real and imaginary parts of ϵ and χ as $\epsilon = \epsilon_r + i\epsilon_i$ and $\chi = \chi_r + \chi_i$. Matching the real parts and the imaginary parts of Eq.(4.15) yields

$$\epsilon_r = 1 + \chi_r, \qquad \epsilon_i = \chi_i. \tag{4.16}$$

Since for nonmagnetic materials $n^2 = \epsilon$,

$$n^2 = (n_r + in_i)^2 = (n_r^2 - n_i^2) + i(2n_r n_i) = \epsilon_r + i\epsilon_i, \tag{4.17}$$

where n_r and n_i are the real and imaginary parts of n. Equating the real parts and imaginary parts of Eq.(4.17) yields

$$n_r^2 - n_i^2 = \epsilon_r, \qquad 2n_r n_i = \epsilon_i. \tag{4.18}$$

from which

$$n_r = \sqrt{\frac{|\epsilon| + \epsilon_r}{2}}, \qquad n_i = \sqrt{\frac{|\epsilon| - \epsilon_r}{2}}. \tag{4.19}$$

Eq.(4.16) then implies

$$n_r = \sqrt{\frac{\sqrt{(1+\chi_r)^2 + \chi_i^2} + 1 + \chi_r}{2}}, \qquad n_i = \sqrt{\frac{\sqrt{(1+\chi_r)^2 + \chi_i^2} - 1 - \chi_r}{2}}. \tag{4.20}$$

corresponding to the real and imaginary expressions of the refractive index. In Fig.(4.3), we plotted the real and imaginary parts of n as a function of ω for the two-level using Eqs.(3.38) and (4.20). Evidently the real part $n_r(\Delta)$ is positive and its value is around 1, while the imaginary part $n_i(\Delta)$ is peaked at $\Delta = 0$.

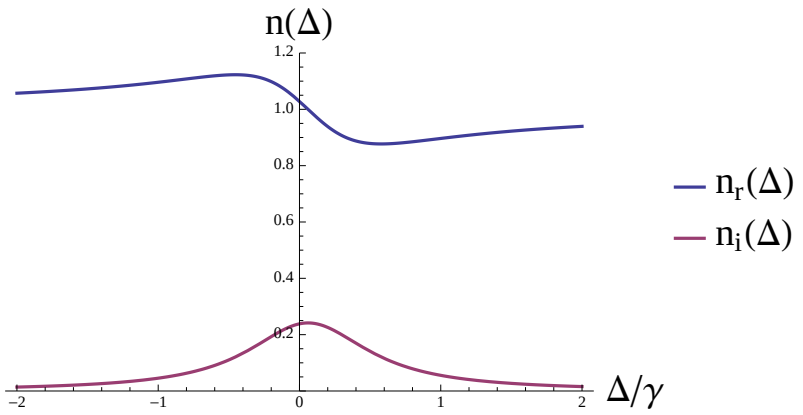

Figure 4.3: The refractive index of the two-level scheme. The blue and red curves correspond to the real and imaginary parts of the refractive index respectively.

The effect of the cavity on the two-level system can now be determined. Since the refractive index of the system is complex, Eq.(4.12) must be employed to calculate the cavity transmission. Expressing the wave vector in terms of $\Delta = \omega - W$ as

$$k(\Delta)L = \omega[n_r(\Delta) + in_i(\Delta)]L/c, \tag{4.21}$$

and assuming that a resonant frequency is located at $\Delta = 0$, we have

$$k(\Delta)L = (\Delta + W)n_r(\Delta)\frac{L}{c}|_{\Delta=0} = \frac{WL}{c}n_r(0) = m\pi. \tag{4.22}$$

Setting the length of the cavity to $L = M\pi c/W$, yields

$$k(0)L = Mn_r(0) = m. \tag{4.23}$$

Approximating $n_r(0)$ by unity implies that $k(0)L \approx M = m$ in order for the cavity to be in resonance at $\Delta = 0$. Thus for example if $M = 80$ and $W = 10^5\gamma$,

$$k(\Delta)L = [n_r(\Delta) + in_i(\Delta)]80\pi\left(\frac{\Delta}{10^5\gamma} + 1\right). \tag{4.24}$$

Selecting a different set of values for these variables below leads to the same qualitative behavior.

The results of $T_{cav}(\omega)$ for different values of R are shown in Fig(4.4). All the values yield zero transmission in the center of the graph where the absorption is maximized, and therefore the

resonance cannot increase the transmission. Further the transmission increases as R approaches zero as the light is then not confined and can exit the cavity with a minimum loss. Hence a two-level system, in general, cannot function as an optical switch as the transmission spectrum cannot be easily shifted while the absorption is large.

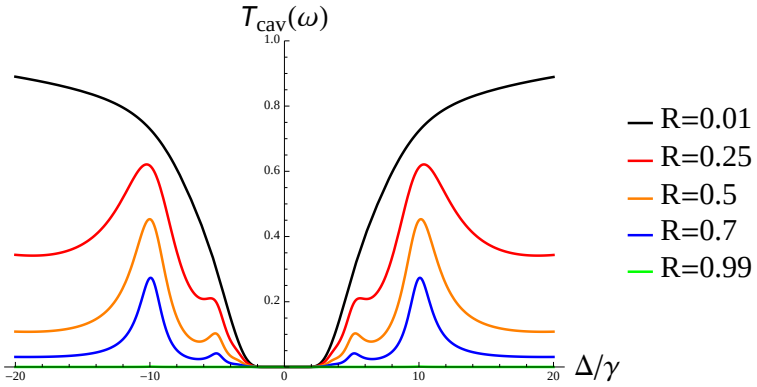

Figure 4.4: The transmission coefficient $T_{cav}(\omega)$ of a two-level atomic Fabry-Pérot cavity for different values of R.

4.2 Optical switches

Optical switching can be achieved via atom-light interactions in a cavity by controlling the transmission/reflection of light. Many methods have been proposed to realize this goal; among these are a two level atomic gas adding a driving field [86], a Λ three level atomic gas along with two coupling fields [87, 88], and a low light output confocal cavity containing a double Λ four-level atom system utilizing a rubidium atomic vapor cell [89]. Other suggestions include application of a microtoroid resonator coupled to an optical fiber [90] and an electromagnetically induced grating (EIG) [91–93]. However, most of these methods suffer from instability due to mechanical effects or from narrow frequency band. Additionally, only one switched transmission band is present.

In a recent article, the authors of [94] theoretically proposed generating controllable wide frequency band via using Λ gas atoms in an optically pumped white light Fabry-Pérot cavity [95–98]. In particular, by changing the intensity of the driving field and the atomic density, the width of the reflectivity can be reduced to zero; hence the optical signal can be switched by modulating the driving field.

All the above methods for controlling the transmission of a frequency band are limited to a single band with a center frequency that is typically determined by the system parameters. This

center frequency is further effectively determined by the atomic spacing, decay rates and associated constants of the scheme which cannot easily be controlled in a fixed physical system.

Broad spectrum white light results if certain phase conditions are satisfied and the cavity is therefore in resonance with a continuous band of frequencies [95–100]. In this project, we accordingly propose three independent procedures, each of which possesses certain unique advantages, for generating up to three broad frequency bands with tunable center frequencies in place of a single band. To accomplish this, a four level double Λ atomic gas within a Fabry-Pérot cavity together with a pumping mechanism and two driving fields with adjustable amplitudes are considered.

4.3 Model description

As mentioned in the previous chapter, by controlling optical parameters such as the susceptibility and the refractive index in an atomic gas, applications such as electromagnetic induced transparency (EIT) [101, 102], negative refractive index [2, 67], and reflective index enhancement without absorption [103] can be achieved. However we demonstrate below that by altering the susceptibility, the transmission bands emitted by an atomic gas confined inside a Fabry-Pérot cavity can be shifted, broadened and increased in number. Several fields are employed inside the cavity to modify the susceptibility of the atomic gas which interacts with electromagnetic radiation according to the four level double Λ scheme of Fig.(4.5).

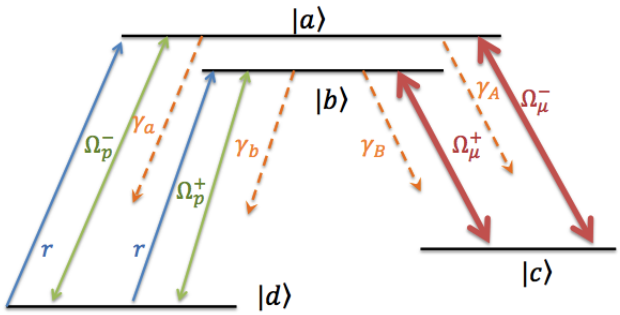

Figure 4.5: The level structures, decay rates and external fields of the double Λ scheme.

The scheme has four levels $|a\rangle$,$|b\rangle$,$|c\rangle$ and $|d\rangle$ where $|a\rangle$ denotes the upper level. Two weak probe fields couple three levels; level $|a\rangle$ and $|d\rangle$ characterized by the Rabi frequency Ω_p^-, and levels $|b\rangle$ to $|d\rangle$ with Rabi frequency Ω_p^+. One strong driving field additionally couples $|a\rangle$ and $|c\rangle$ with Rabi frequency Ω_μ^- while a second applies $|b\rangle$ and $|c\rangle$ with Rabi frequency Ω_μ^+. Two incoherent pumping

mechanisms additionally couple levels $|a\rangle$ and $|d\rangle$ and $|b\rangle$ and $|d\rangle$ with a pumping rate denoted by r. The decay rates from the exited states equal γ_a from $|a\rangle$ to $|d\rangle$, γ_b from $|b\rangle$ to $|d\rangle$, γ_A from $|a\rangle$ to $|c\rangle$ and finally γ_B from $|b\rangle$ to $|c\rangle$. The decay rates from $|c\rangle$ and $|d\rangle$ are assumed to be zero.

Various experimental implementations of the above double Λ scheme exist [104–106]. For example, in the rubidium [107] or sodium [108] gas two hyperfine ground levels with $F = 1$ and $F = 2$ are present and the states $|d\rangle$ and $|c\rangle$ then correspond to the $M_F = -1$ and $M_F = 1$ magnetic sublevels of the $F = 1$ hyperfine ground level while the upper states $|a\rangle$ and $|b\rangle$ in our notation are the $M_F = 0, F = 1$ and $M_F = 0, F = 2$ excited states. In this case, two oppositely circularly polarized counter propagating fields $\sigma^{\pm}$ must be employed for the drive and probe fields.

4.4 Analytic formulation

After applying the dipole approximation and the rotating wave approximation (RWA) the Hamiltonian of the double Λ scheme becomes

$$\hat{H} = \hbar \left[\sum_i^{a,b,c,d} \omega_i |i\rangle\langle i| - \frac{\Omega_p^-}{2} e^{i\Delta_1 t} |a\rangle\langle d| - \frac{\Omega_p^+}{2} e^{i\Delta_2 t} |b\rangle\langle d| - \frac{\Omega_\mu^+}{2} e^{i\Delta_3 t} |b\rangle\langle c| - \frac{\Omega_\mu^-}{2} e^{i\Delta_4 t} |a\rangle\langle c| + H.c. \right], \tag{4.25}$$

in which $\hbar\omega_i$ is the energy of the level $|i\rangle$ and the Rabi frequencies of the probe fields are $\Omega_p^- = |d_{ad}|E/\hbar$ and $\Omega_p^+ = |d_{bd}|E/\hbar$ in which E is the electric field of the probe field and the driving field Rabi frequencies are $\Omega_\mu^+ = |d_{bc}|E_\mu^+/\hbar$, $\Omega_\mu^- = |d_{ac}|E_\mu^-/\hbar$. The detuning parameters Δ_i are given by $\Delta_1 = \omega_{ad} - \omega_p^-$, $\Delta_2 = \omega_{bd} - \omega_p^+$, $\Delta_3 = \omega_{bc} - \omega_\mu^+$ and $\Delta_4 = \omega_{ac} - \omega_\mu^-$. Here $\omega_{ij} = \omega_j - \omega_i$ while $\omega_p^{\pm}$ and $\omega_\mu^{\pm}$ denote the frequencies of the probe and driving fields, respectively.

A stable steady state only exists in the double Λ scheme if the frequencies of the interacting beams satisfy the condition [109, 110]

$$\omega_p^- - \omega_p^+ = \omega_\mu^- - \omega_\mu^+, \tag{4.26}$$

as is easily verified by applying Hamiltonian of Eq.(4.25) to the master equation below. In the following analysis the frequencies of the probe and driving beams are set to $\omega_p^- = \omega_p^+ = \omega$, and $\omega_\mu^+ = \omega_\mu^- = \omega_\mu$. Accordingly only one probe field with frequency ω is present while the frequency of both driving fields equals ω_μ. The detuning parameters Δ_i are then $\Delta_1 = \omega_{ad} - \omega$, $\Delta_2 = \omega_{bd} - \omega$,

$\Delta_3 = \omega_{bc} - \omega_\mu$, and $\Delta_4 = \omega_{ac} - \omega_\mu$. The master equation then takes the form

$$\dot{\hat{\rho}} = -\frac{i}{\hbar}[\hat{H}, \hat{\rho}], \tag{4.27}$$

in terms of the density matrix operator $\hat{\rho}$. After applying the Hamiltonian of Eq.(4.25) to the master equation, inserting the expressions for the decay rates and the pumping rates and transforming in standard fashion one obtains,

$$\dot{\rho}_{aa} = -(\gamma_a + \gamma_A)\rho_{aa} + r\rho_{dd} + \frac{i}{2}(\tilde{\rho}_{ac}\Omega_\mu^{-*} - \tilde{\rho}_{ad}\Omega_p^{-*} + H.c.), \tag{4.28}$$

$$\dot{\rho}_{bb} = -(\gamma_b + \gamma_B)\rho_{bb} + r\rho_{dd} + \frac{i}{2}(\tilde{\rho}_{bd}\Omega_p^{+*} - \tilde{\rho}_{bc}\Omega_\mu^{+*} + H.c), \tag{4.29}$$

$$\dot{\rho}_{cc} = \gamma_A\rho_{aa} + \gamma_B\rho_{bb} + \frac{i}{2}(\tilde{\rho}_{bc}\Omega_\mu^{+*} + \tilde{\rho}_{ac}\Omega_\mu^{-*} + H.c.), \tag{4.30}$$

$$\dot{\rho}_{dd} = -2r\rho_{dd} + \gamma_a\rho_{aa} + \gamma_b\rho_{bb} + \frac{i}{2}(\tilde{\rho}_{ad}\Omega_p^{-*} + \tilde{\rho}_{bd}\Omega_p^{+*} + H.c.), \tag{4.31}$$

$$\dot{\tilde{\rho}}_{ab} = -\gamma_{ab}\tilde{\rho}_{ab} - 2i\omega_{ab}\tilde{\rho}_{ab} + \frac{i}{2}(\tilde{\rho}_{cb}\Omega_\mu^- + \tilde{\rho}_{db}\Omega_p^- - \tilde{\rho}_{ad}\Omega_p^{+*} - \tilde{\rho}_{ac}\Omega_\mu^{+*}), \tag{4.32}$$

$$\dot{\tilde{\rho}}_{ac} = -\gamma_{ac}\tilde{\rho}_{ac} - i(\Delta_\mu + \omega_{ab})\tilde{\rho}_{ac} + \frac{i}{2}(-\tilde{\rho}_{ab}\Omega_\mu^+ + (\rho_{cc} - \rho_{aa})\Omega_\mu^- + \tilde{\rho}_{dc}\Omega_p^-), \tag{4.33}$$

$$\dot{\tilde{\rho}}_{ad} = -\gamma_{ad}\tilde{\rho}_{ad} + i(\Delta - \omega_{ab})\tilde{\rho}_{ad} + \frac{i}{2}(-\tilde{\rho}_{ab}\Omega_p^+ + \tilde{\rho}_{cd}\Omega_\mu^- - (\rho_{aa} - \rho_{dd})\Omega_p^-), \tag{4.34}$$

$$\dot{\tilde{\rho}}_{bc} = -\gamma_{bc}\tilde{\rho}_{bc} - i(\Delta_\mu - \omega_{ab})\tilde{\rho}_{bc} + \frac{i}{2}(\tilde{\rho}_{dc}\Omega_p^- - (\rho_{bb} - \rho_{cc})\Omega_\mu^+ - \tilde{\rho}_{ba}\Omega_\mu^-), \tag{4.35}$$

$$\dot{\tilde{\rho}}_{bd} = -\gamma_{bd}\tilde{\rho}_{bd} + i(\Delta + \omega_{ab}) + \frac{i}{2}(\tilde{\rho}_{cd}\Omega_\mu^+ - \tilde{\rho}_{ba}\Omega_p^- - (\rho_{bb} - \rho_{dd})\Omega_p^+), \tag{4.36}$$

$$\dot{\tilde{\rho}}_{cd} = -\gamma_{cd}\tilde{\rho}_{cd} + i(\Delta_\mu + \Delta)\tilde{\rho}_{cd} + \frac{i}{2}(-\tilde{\rho}_{cb}\Omega_p^+ - \tilde{\rho}_{ca}\Omega_p^- + \tilde{\rho}_{bd}\Omega_\mu^{+*} + \tilde{\rho}_{ad}\Omega_\mu^{-*}), \tag{4.37}$$

where $\tilde{\rho}_{ij}$ is the density matrix element after the transformations and $\gamma_{ij} \equiv (\gamma_i + \gamma_j)/2$. The detuning parameters appearing in the above equation are defined by $\Delta = \omega - W = \omega - \omega_{ad} - \omega_{bd}$ and $\Delta_\mu = Q - \omega_\mu = \omega_{ac} + \omega_{bc} - \omega_\mu$, where W is $\omega_{ad} + \omega_{bd}$ and $Q = \omega_{ac} + \omega_{bc}$. In this manner, the values of the energies ω_{ad}, ω_{bc}, ω_{bc} and ω_{bd}, not need to be determine individually as only ω_{ab} appears.

To find the steady state matrix elements, $\dot{\tilde{\rho}}_{ij} = 0$, and the two associated elements of the probe field, $\tilde{\rho}_{ad}$ and $\tilde{\rho}_{bd}$, the above equations are solved algebraically. Since the probe field is weak, $\Omega_p^\pm$ is

only retained to first order, while the strong driving fields $\Omega_\mu^\pm$ are kept to the second order. Solving Eqs.(4.32-4.37) then yields

$$\tilde{\rho}_{bd}^{(1)} = \frac{i}{D_{bd} + \frac{|\Omega_\mu^+|^2}{4D_{cd}}} \left[\Omega_p^+ \left(\frac{|\Omega_\mu^+|^2}{8D_{cd}D_{bc}^*} P_{bc} - \frac{1}{2} P_{bd} \right) - \Omega_p^- \left(\frac{\Omega_\mu^+ \Omega_\mu^{-*}}{8D_{cd}D_{ac}^*} P_{ca} \right) \right], \tag{4.38}$$

$$\tilde{\rho}_{ad}^{(1)} = \frac{i}{D_{ad} + \frac{|\Omega_\mu^-|^2}{4D_{cd}}} \left[\Omega_p^+ \left(\frac{\Omega_\mu^- \Omega_\mu^{+*}}{8D_{cd}D_{bc}^*} P_{bc} \right) - \Omega_p^- \left(\frac{|\Omega_\mu^-|^2}{8D_{cd}D_{ac}^*} P_{ca} + \frac{1}{2} P_{ad} \right) \right], \tag{4.39}$$

where $P_{ij} = \rho_{ii} - \rho_{jj}$ and $\tilde{\rho}_{ij}^{(1)}$ denote the population difference and the first order approximation of the probe field of element $\tilde{\rho}_{ij}$ while the different D_{ij} parameters are defined by $D_{bd} = \gamma_{bd} - i(\Delta + \omega_{ab})$, $D_{ad} = \gamma_{ad} - i(\Delta - \omega_{ab})$, $D_{cd} = \gamma_{cd} - i(\Delta_\mu + \Delta)$, $D_{bc} = \gamma_{bc} + i(\Delta_\mu - \omega_{ab})$ and $D_{ac} = \gamma_{ac} + i(\Delta_\mu + \omega_{ab})$.

The electric susceptibility, χ, is the sum of the contributions, χ_{ad} and χ_{bd}, from each of the interactions of the probe field as

$$\begin{aligned} \chi\epsilon_0 E/2 &= |d_{ad}|\tilde{\rho}_{ad}^{(1)} + |d_{bd}|\tilde{\rho}_{bd}^{(1)}, \\ \chi &= 2|d_{ad}|\tilde{\rho}_{ad}^{(1)}/(\epsilon_0 E) + 2|d_{bd}|\tilde{\rho}_{bd}^{(1)}/(\epsilon_0 E), \\ \chi &= \chi_{ad} + \chi_{bd}, \end{aligned} \tag{4.40}$$

Substituting Eqs.(4.38,4.39) into Eq.(4.40) then yields

$$\chi_{bd} = \frac{i}{D_{bd} + \frac{|\Omega_\mu^+|^2}{4D_{cd}}} \left[\mathcal{C} \left(\frac{|\Omega_\mu^+|^2}{4D_{cd}D_{bc}^*} P_{bc} - P_{bd} \right) - \mathcal{B} \left(\frac{\Omega_\mu^+ \Omega_\mu^{-*}}{4D_{cd}D_{ac}^*} P_{ca} \right) \right], \tag{4.41}$$

$$\chi_{ad} = \frac{i}{D_{ad} + \frac{|\Omega_\mu^-|^2}{4D_{cd}}} \left[\mathcal{B} \left(\frac{\Omega_\mu^- \Omega_\mu^{+*}}{4D_{cd}D_{bc}^*} P_{bc} \right) - \mathcal{A} \left(\frac{|\Omega_\mu^-|^2}{4D_{cd}D_{ac}^*} P_{ca} + P_{ad} \right) \right]. \tag{4.42}$$

Here the strength parameters are defined by

$$\mathcal{A} = \frac{N|d_{ad}|^2}{\hbar\epsilon_0}, \quad \mathcal{B} = \frac{N|d_{ad}||d_{bd}|}{\hbar\epsilon_0}, \quad \mathcal{C} = \frac{N|d_{bd}|^2}{\hbar\epsilon_0}. \tag{4.43}$$

The contribution from all atoms is obtained by multiplying the atomic susceptibility by the number of atoms per unit volume, N. The exact expressions for the atomic populations ρ_{ii} are then derived by solving Eqs.(4.28-4.31) together with the normalization condition $\rho_{aa} + \rho_{bb} + \rho_{cc} + \rho_{dd} = 1$ which give

$$\rho_{aa}^{(0)} = r \frac{R_a(\gamma_b + \gamma_B) + \gamma_B R_a + \gamma_b R_b + 2R_a R_b}{a_1 R_a + a_2 R_b + a_3 R_a R_b + a_4}, \tag{4.44}$$

$$\rho_{bb}^{(0)} = r\frac{R_b(\gamma_a+\gamma_A)+\gamma_a R_a+\gamma_A R_b+2R_aR_b}{a_1R_a+a_2R_b+a_3R_aR_b+a_4}, \tag{4.45}$$

$$\rho_{dd}^{(0)} = \frac{\gamma_a\rho_{aa}^{(0)}+\gamma_b\rho_{bb}^{(0)}}{2r}, \tag{4.46}$$

$$\rho_{cc}^{(0)} = 1-\rho_{aa}^{(0)}-\rho_{bb}^{(0)}-\rho_{cc}^{(0)}, \tag{4.47}$$

in which $\rho_{ii}^{(0)}$ designates the zero order probe field, and

$$R_a = \frac{\gamma_{ac}|\Omega_\mu^-|^2}{2[\gamma_{ac}^2+(\Delta_\mu+\omega_{ab})]}, \quad R_b = \frac{\gamma_{bc}|\Omega_\mu^+|^2}{2[\gamma_{bc}^2+(\Delta_\mu-\omega_{ab})]}, \tag{4.48}$$

$a_1 = \gamma_a(\gamma_b+\gamma_B)+r(4\gamma_B+2\gamma_b+\gamma_a)$, $a_2 = \gamma_b(\gamma_a+\gamma_A)+r(4\gamma_A+2\gamma_a+\gamma_b)$, $a_3 = 6r+\gamma_b+\gamma_a$, and $a_4 = r(2\gamma_A\gamma_B+\gamma_A\gamma_b+\gamma_B\gamma_a)$.

To illustrate the behavior of the susceptibility, the above equations are evaluated with standard parameter values. With $\gamma = 10^7$ the decay parameters employed here are $\gamma_a = \gamma_b = \gamma$, $\gamma_A = \gamma_B = 0.2\gamma$, $\gamma_{ab} = \gamma_{cd} = 0$ and $\gamma_{ac} = \gamma_{bc} = \gamma_{ad} = \gamma_{bd} = (\gamma_a+\gamma_A)/2 = 0.6\gamma$. The density parameters are similarly given in terms of $\mathcal{C}$ by $\mathcal{A} = \theta\mathcal{C}$ and $\mathcal{B} = \Phi\mathcal{C}$, with θ and Φ set to 1.1 and 1.05 respectively. The driving fields are expressed in terms of Ω_μ^- by $\Omega_\mu^+ = \Omega_\mu^-/\alpha$ where α corresponds to the ratio between the two fields. These fields are assumed to be well detuned so that $\Delta_\mu = 0$, while the level spacing $\omega_{ab} = \gamma$. A detuning parameter is additionally defined as $\Delta = \omega - W$, where for typical gases in the optical limit $W = 10^6\gamma$. Accordingly, the following sections examine the dependence of the susceptibility on the free parameters r, Ω_μ^-, α and $\mathcal{C}$.

4.5 Susceptibility

To evaluate the susceptibility, Eq.(4.40), it is convenient to set $\mathcal{C} = \gamma$ since the suceptibility scales linearly with $\mathcal{C}$. The following cases are then distinguished

4.5.1 $\Omega_\mu^- = \Omega_\mu^+$, $\alpha = 1$

Since all systems with $r < \gamma$ possess the same inversion properties, they can be analyzed by setting the pumping rate r to zero such that only the state $|d\rangle$ is populated and then increasing the pumping rate up to a value of γ. This insures that the atomic population is primarily in the ground state

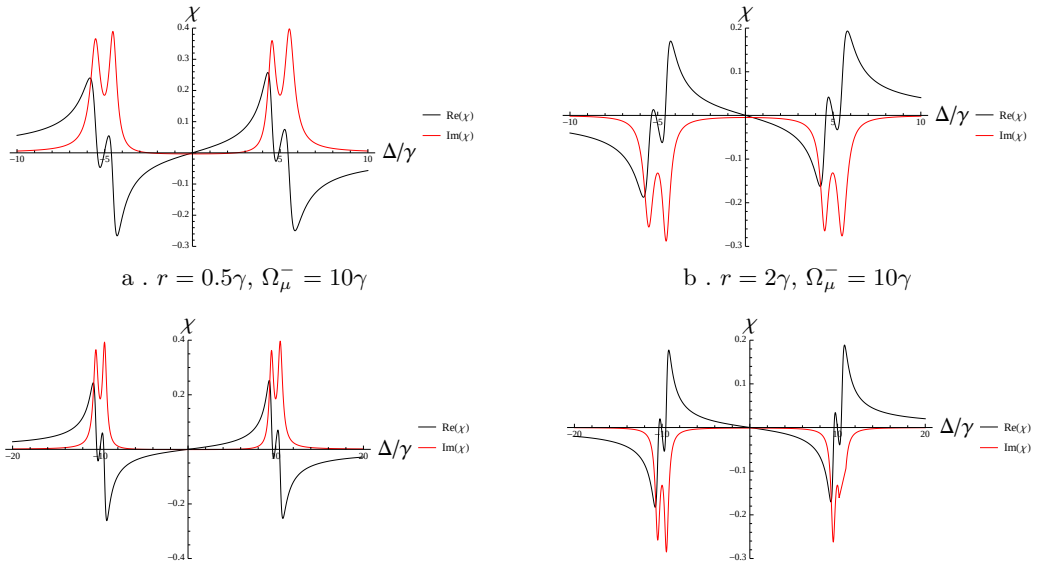

a . $r = 0.5\gamma$, $\Omega_\mu^- = 10\gamma$ b . $r = 2\gamma$, $\Omega_\mu^- = 10\gamma$

c . $r = 0.5\gamma$, $\Omega_\mu^- = 20\gamma$ d . $r = 2\gamma$, $\Omega_\mu^- = 20\gamma$

Figure 4.6: The real and imaginary parts of χ for different r and Ω_μ^- with $\alpha = 1$. The real and imaginary parts of χ are show as the black and red curves, respectively.

and therefore $\rho_{aa}^{(0)}, \rho_{bb}^{(0)} - \rho_{dd}^{(0)} < 0$. For the two driving fields with $\alpha = 1$, a pumping rate $r < \gamma$, the susceptibility exhibits EIT as evident from Fig.4.6(a) for which the driving field $\Omega_\mu^- = 10\gamma$ and the pumping rate $r = 0.5\gamma$. Evidently the absorption, which is proportional to $\mathrm{Im}(\chi) \approx 0$ over an interval given approximately by $-4\gamma < \Delta < 4\gamma$ while $\mathrm{Re}(\chi)$ displays a linear dispersion with positive slope. In Fig.4.6(c), the driving field is set instead to $\Omega_\mu^- = 20\gamma$ with the identical pumping rate as Fig.4.6(a) leading to an increase in the width of the near zero absorption region to $-9\gamma < \Delta < 9\gamma$ but otherwise the same behavior as Fig.4.6(a). In fact if the near zero absorption width is denoted by T for large driving fields in our system $T \approx \Omega_\mu^-$ over a region from $\Delta \approx -\Omega_\mu^-/2$ and to $\Delta \approx \Omega_\mu^-/2$. That is, the width of the EIT can be manipulated by modulating the amplitude of the driving fields.

For $r > \gamma$, the population inversion becomes positive, with the result that both $\rho_{aa}^{(0)}$ and $\rho_{bb}^{(0)}$ exceed $\rho_{dd}^{(0)}$. In this case, Figs.4.6(b), 4.6(d), indicate that EIT is again present but that the dispersion slope reverses sign. As in the $r < \gamma$ case, the width of the negative absorption region is given by $T \approx \Omega_\mu^-$. Note that in all of the figures in Figs.4.6 two peaks are present on each side of the absorption line. Since these are associated with ω_{ab}, their positions can be altered by changing the value of ω_{ab}. Finally, the width of the EIT and the sign of the dispersion slope can be easily controlled by adjusting the amplitude of the driving fields.

4.5.2 $\Omega_\mu^- \neq \Omega_\mu^+$, $\alpha \neq 1$

Next the case that α differs from unity (and $\alpha \neq 0, \infty$) so that the intensities of the driving fields differ (note that systems with reciprocal values of α are nearly equivalent) is investigated. In Figs.4.7(a), 4.7(b) χ is plotted for $\alpha = 2$, $\Omega_\mu^- = 20\gamma$ and $r = 0.5\gamma$ and $r = 2\gamma$, respectively. In both figures three separate regions exist in which $\mathrm{Im}(\chi)$ and hence the absorption is nearly zero. The width of the middle region is $\approx 10\gamma$, while the widths of the left and right regions are $\approx 5\gamma$. However in Fig.4.7(a) with $r = 0.5\gamma$, the three regions exhibit EIT behavior, while in Fig.4.7(b) the dispersion slope is negative. In both cases, the width of the middle region is $T \approx \Omega_\mu^-/\alpha$, while that of the two side regions is $T \approx \Omega_\mu^-(\alpha - 1)/(2\alpha)$.

If one of the driving fields is absent, $\alpha \to 0, \infty$, only two zero absorption regions exist as evident from Figs.4.7(c), 4.7(d). Similarly whether the EIT or the negative dispersion behavior is present depends on the value of r. Therefore, changing the ratio of the driving fields strongly influences the widths of the low absorption regions. In the following we will focus on systems with finite values of α and hence three EIT or negative dispersion regions. The two region $\alpha \to \infty, 0$ case however is entirely analogous.

To describe Figs.4.7(a), 4.7(b) and other cases with $\alpha > 1$ we denote the left, middle and right negative dispersion regions of Δ with negligible absorption by (-1), (0) and $(+1)$ respectively. The point within each region at which $\mathrm{Re}(\chi) = 0$ is further termed the center point of the region and are labeled as Δ_- , Δ_0, and Δ_+ with $\Delta_- \approx -|\Omega_\mu^-|(\alpha + 1)/(4\alpha)$, 0 and $\Delta_+ \approx +|\Omega_\mu^-|(\alpha + 1)/(4\alpha)$, respectively. In summary, by manipulating the relative amplitude of the driving fields one, two or three regions exhibiting EIT or negative dispersion can be obtained. These regions will be employed to generate three white bands in the following sections.

4.6 White cavity conditions

While a Fabry-Pérot cavity supports discrete resonant frequencies as Eq.(4.14) showed, for a white light cavity (WLC) such as that generated by bifrequency Raman gain [95,97,100], a continuous band of frequencies is resonant simultaneously inside the cavity. In a WLC the cavity condition Eq.(4.14) must be satisfied for the center points together with a negative and roughly linear dispersion and phase delay cancellation. As seen already in Figs.4.6(b),4.6(d), 4.7(b), 4.7(d), the negative dispersion condition is realized within adjustable wavelength bands if the pumping $r > \gamma$.

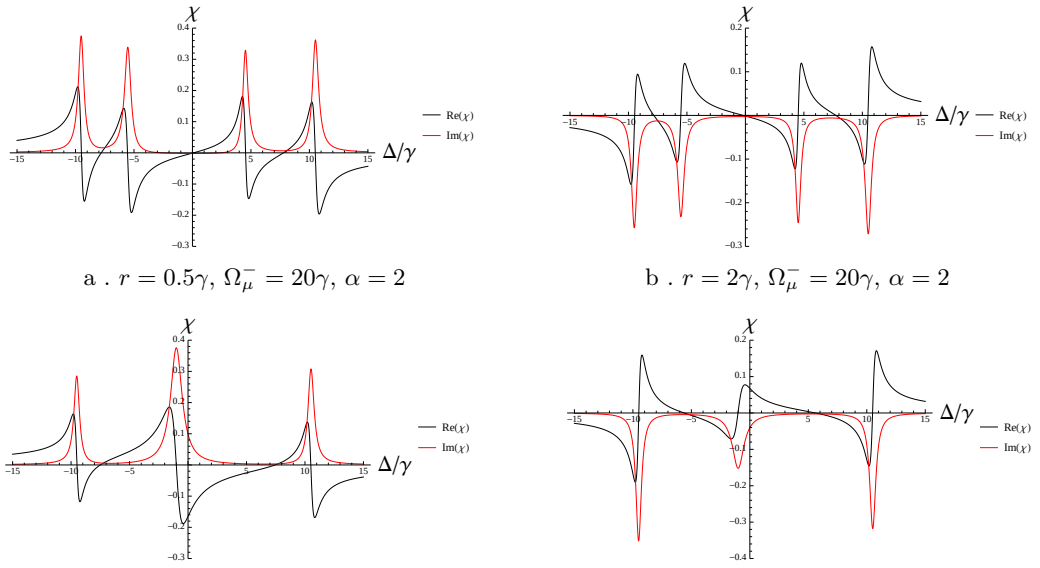

a . $r = 0.5\gamma$, $\Omega_\mu^- = 20\gamma$, $\alpha = 2$

b . $r = 2\gamma$, $\Omega_\mu^- = 20\gamma$, $\alpha = 2$

c . $r = 0.5\gamma$, $\Omega_\mu^- = 20\gamma$, $\alpha \to \infty$

d . $r = 2\gamma$, $\Omega_\mu^- = 20\gamma$, $\alpha \to \infty$

Figure 4.7: The real (black) and imaginary (red) parts of χ for different values of r and Ω_μ^- for $\alpha > 1$.

The phase delay condition is derived from Eq.(4.14) which, however, yields discrete frequencies rather than the continuous band of a WLC. Accordingly Eq.(4.14) must first be differentiated with respect to ω where

$$\frac{d\{\omega \mathrm{Re}[n(\omega)]\}}{d\omega} = \omega \frac{d\{\mathrm{Re}[n(\omega)]\}}{d\omega} + \mathrm{Re}[n(\omega)] = 0. \tag{4.49}$$

In the presence of negative dispersion $\mathrm{Re}[n(\omega)]$ can equal the negative of the first term. For the cases when the two driving fields possess equal amplitudes, $\alpha = 1$, the centre point of the negative dispersion is $\Delta = 0$ corresponding to $\omega = W$. Since $\chi(W) \approx 0$ near this point the refractive index $n(\omega) \approx 1$ and Eq.(4.49) implies

$$\frac{d\{\mathrm{Re}[n(\omega)]\}}{d\omega}|_{\omega=W} = -\frac{1}{W}. \tag{4.50}$$

The slope near the center point is roughly linear, hence the derivative can be approximated as

$$\frac{d\{\mathrm{Re}[n(\omega)]\}}{d\omega}|_{\omega=W} \approx \frac{\mathrm{Re}[n(W+\gamma)] - \mathrm{Re}[n(W-\gamma)]}{2\gamma}. \tag{4.51}$$

Next the refractive index can be approximately expanded as $n(\omega) = \sqrt{1+\chi(\omega)} \approx 1 + \chi'(\omega)/2 + i\chi''(\omega)/2$, in which $\chi'(\omega)$ and $\chi''(\omega)$ are the real and imaginary parts of the susceptibility, respec-

tively. The final form of the white light condition for equal driving fields is then

$$\chi'(W+\gamma) - \chi'(W-\gamma) = -\frac{4\gamma}{W}. \tag{4.52}$$

This equation can be employed to determine the required value of Ω_μ^- for the driving field that satifies the WLC.

Repeating the above derivation for unequal driving field amplitudes, yields separate conditions for each negative dispersion region. These can be expressed as

$$\chi'(\Delta_C + W + \gamma) - \chi'(\Delta_C + W - \gamma) = -\frac{4\gamma}{\Delta_C + W}. \tag{4.53}$$

Here $\Delta_C = \omega_C - W$ denotes the centre point of each region or the point at which $\chi'(\omega_C) = 0$ in the case of a negative dispersion slope. For example, for each of the three near-zero absorption and negative dispersion regions in Fig. 4.7(b), Eq.(4.53) yields a separate result for the driving fields at each centre point to satisfy the WLC. These can then be employed to generate three different resonant bands.

Observe next that when $\omega_{ab} \ll \Omega_\mu^\pm$, the populations $\rho_{aa} \approx \rho_{bb} \approx \rho_{cc}$. Hence for simplicity both P_{bc} and P_{ca} can be set to zero in Eqs.(4.41, 4.42) so that only the second term of Eq.(4.41) and the third term of Eq.(4.42) remain. The real and imaginary parts of the susceptibility, $\chi = \chi' + \chi''$, are then

$$\chi'(\omega) = -\frac{\theta\mathcal{C}\left[-\Delta + \omega_{ab} + \frac{|\Omega_\mu^-|^2}{4\Delta}\right] P_{ad}}{\gamma_{ad}^2 + \left[-\Delta + \omega_{ab} + \frac{|\Omega_\mu^-|^2}{4\Delta}\right]^2} - \frac{\mathcal{C}\left[-\Delta - \omega_{ab} + \frac{|\Omega_\mu^-|^2}{4\alpha^2\Delta}\right] P_{bd}}{\gamma_{bd}^2 + \left[-\Delta - \omega_{ab} + \frac{|\Omega_\mu^-|^2}{4\alpha^2\Delta}\right]^2}, \tag{4.54}$$

$$\chi''(\omega) = -\frac{\theta\mathcal{C}\gamma_{ad}P_{ad}}{\gamma_{ad}^2 + \left[-\Delta + \omega_{ab} + \frac{|\Omega_\mu^-|^2}{4\Delta}\right]^2} - \frac{\mathcal{C}\gamma_{bd}P_{bd}}{\gamma_{bd}^2 + \left[-\Delta - \omega_{ab} + \frac{|\Omega_\mu^-|^2}{4\alpha^2\Delta}\right]^2}, \tag{4.55}$$

where as usual Δ is $\omega - W$. In driving these equations we assumed that $\gamma_{cd} = 0$ and $\Delta_\mu = 0$. Replotting Figs.(4.6,4.7) using these expressions leads to almost the same set of curves.

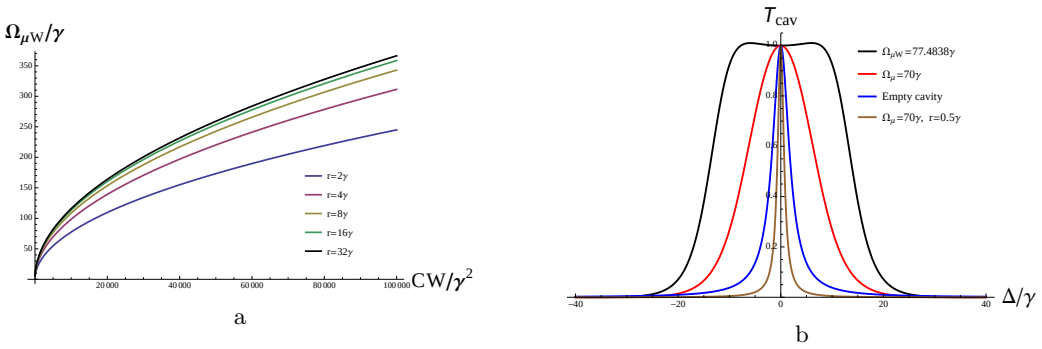

Figure 4.8: (a) The driving field $\Omega_{\mu W}$ required to satisfy the WLC condition Eq.(4.52). (b) The dependence of the cavity transmission on the driving field for $r = 2\gamma$ (except for the inner curve).

4.7 Single white band

As noted above, for equal amplitudes of the driving fields $\Omega_\mu^\pm$, e.g. $\alpha = 1$, a single giant resonant frequency band is obtained when the driving field value satisfies a condition corresponding to the WLC of Eq.(4.52). Fig.4.8(a), which plots this required field, $\Omega_{\mu W}^-$, against $\mathcal{C}$ and r, demonstrates that $\Omega_{\mu W}^-$ is nearly proportional to $\sqrt{\mathcal{C}W}$. For example, for $r = 2\gamma$, a graph of $\Omega_{\mu W}^- = 0.774741\sqrt{\mathcal{C}W}$ almost coincides with the plot in Fig.4.8(a). As well, $\Omega_{\mu W}^-$ generally increases monotonically with the pumping r; however the $r = 16\gamma$ and $r = 32\gamma$ curves are nearly identical since the population saturates for large r values.

For $r = 2\gamma$, while previously our calculations employed $\mathcal{C} = \gamma$ as in a standard gas, the previous plot indicates that $\Omega_{\mu W}^- = 774\gamma$. Since this value is unacceptably large, the gas density is decreased by setting $\mathcal{C} = 0.01\gamma$ which yields a more reasonable value of $\Omega_{\mu W}^- = 77.48\gamma$. Hence this scheme for generating a white driving field requires lower pressure compared to previous experiments.

The effect of the white driving field is apparent from the transmission T_{cav} of the Fabry-Perot cavity of Eq.(4.12). The cavity length must equal $L = m\lambda/2 = \pi cm/W$, where m is any integer, to satisfy Eq.(4.14). The upper exponent is then a function of Δ as $i\pi m(W + \Delta)n(\Delta)/W$ where in Fig.4.8(b) $T = 0.001$, $R = 0.999$, $m = 100$ and $W = 10^6\gamma$.

Evidently in Fig.4.8(b) for $\Omega_{\mu W}^-$ the transmission band is broadened significantly compared to that of an empty cavity. The linewidth is additionally nearly 40γ, while additional calculations indicate that the linewidth of the white driving fields are nearly proportional to $\Omega_{\mu W}^{2/3}$. For comparison, the transmission is also plotted for a second value of the driving field, namely $\Omega_\mu^- = 70\gamma$. The linewidth for this value is less than for the white driving field. We further plot the transmission for

$\Omega_\mu^- = 70\gamma$, but with pumping $r = 0.5\gamma$. The pumping clearly reduces the linewidth of the band compared to the empty cavity band since for pumping strengths $r < \gamma$, EIT, which in our scheme leads to a reduced linewidth, is the dominant physical effect in this case.

To summarize, the propagation of light though a cavity with a wide transmission band can be controlled by adjusting the amplitudes of the two driving fields. To activate a white band, the value of Ω_μ^- must be within a certain range that depends on the gas density and the pumping rate according to Fig.4.8(a). The linewidth of the transmission band can further be controlled by varying the pumping, gas density and the white driving field amplitude.

4.8 Generation of three white bands

4.8.1 Method A

When the two driving fields are unequal, three negative dispersion regions can be supported as Figs.4.7(b), 4.7(d) demonstrate. While the procedure in the previous section can be employed to create a white band in one of the regions, this is not as efficient as white light generation for $\alpha = 1$. Therefore, we here consider activating all three regions. However, each of these, in principle requires a different length. This length must be a half integer multiple of the centre wavelength according to Eq.(4.14) which, noting that χ' equal to zero at the centre points (Δ_0 and $\Delta_\pm$) yields

$$L\omega_m = cm\pi. \tag{4.56}$$

for $Re(n(\omega_C)) = 1$.

Since the cavity length is the product of an integer k with a half wavelength at frequency $\omega = W$, that is, $L = k\lambda/2 = \pi ck/W$, where k is an integer, this yields the condition

$$\omega_m = \frac{mW}{k}. \tag{4.57}$$

Since the center point of region (0) is found to be $\Delta_0 = 0$, ω_m must equal W, and therefore $m = k$. To insure that the centre points of the regions (± 1) coincide with $\omega_{m\pm1}$, observe that the centre point frequencies $\Delta_\pm$ are $W + \Delta_\pm$ and hence $\omega_{m\pm1} = W + \Delta_\pm$ leading to the conditions $\omega_{m\pm1} = W + \Delta_\pm = \frac{W(m\pm1)}{k} = \frac{W(m\pm1)}{m} = W \pm \frac{W}{m}$ and therefore

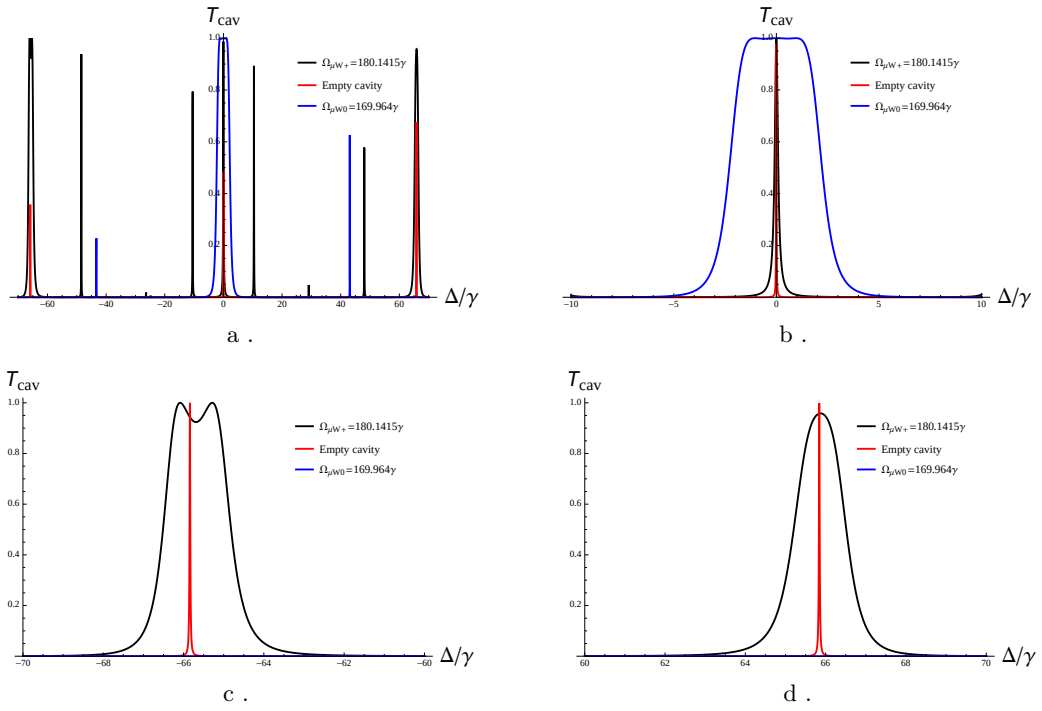

Figure 4.9: Cavity transmission frequencies for different driving field values with $\alpha = 3$. (a) All bands together. (b) The band of region (0). (c) The band of region (-1). (d) The band of region $(+1)$.

$$\Delta_{\pm} = \pm\frac{W}{m}. \tag{4.58}$$

Since $W = 10^6\gamma$, $\Delta_{\pm}$ can be approximated by an integer m to satisfy the above equation, however the condition that $|\Delta_+| = |\Delta_-|$ still remains.

The above results for χ for a given α and Ω_μ^- yield $|\Delta_+| \approx |\Delta_-|$, however, the WLC Eq.(4.53) requires that the field amplitudes differ in order to generate the regions (±1), implying $|\Delta_+| \neq |\Delta_-|$. For example, employing our current parameter values with $\omega_{ab} = \gamma$ and $\alpha = 3$, we find that the fields required to satisfy the WLC:s in Eq.(4.53) with $\chi'(\omega) = 0$ for the regions (±1) are given by $(\Omega_{\mu W+} = 177.1385\gamma, \Omega_{\mu W-} = 183.7735\gamma)$, where $\Omega_{\mu W\pm}$ are the Ω_μ^- values in the regions (±1). These two values yield $(\Delta_+ = 64.71\gamma, \Delta_- = -67.18\gamma)$. Hence Eq.(4.58) is not fulfilled and only the regions $((0),(+1))$ or $((0),(-1))$ will satisfy the WLC.

To circumvent this difficulty we instead set $\omega_{ab} = 0.1\gamma$, and solve the two equations (Eq.(4.53) with $\chi'(\omega) = 0$). This gives for region $(+1)$, $\Omega_\mu^- = \Omega_{\mu W+} = 180.1415\gamma$ and $\Delta_+ = 65.8392\gamma$ while for region (-1), $\Omega_\mu^- = \Omega_{\mu W-} = 180.7945\gamma$ and $\Delta_- = -66.0827\gamma$. Here both $|\Delta_\pm|$ are nearly identical indicating that in general for small ω_{ab}, the values of $|\Delta_\pm|$ are nearly identical so that Eq.(4.58) is

approximately fulfilled.

Since the two values of $|\Delta_\pm|$ are not precisely identical, we impose Eq.(4.58) in region $(+1)$ while approximately satisfying this equation in region (-1). This yields for m in Eq.(4.58) $k = m = W/\Delta_+ \approx 15188$. The WLC for the region (0) from Eq.(4.52) then gives $\Omega_{\mu W0} = 169.964\gamma$. Accordingly, the three regions (0), (±1) can be activated in the same cavity.

For simplicity, neglecting the small gain associated with regions (±1) yields the transmission T_{cav} for the white bands in the three separate wavelength regions with $T_{cav} \approx 1$ illustrated in Fig.4.9(a). Of these, the band in region (0) is the widest with a linewidth of $\approx 6\gamma$ Hz, while the linewidth in the (±1) regions is $\approx 3\gamma$ Hz. The three bands are shown indivdually in Figs.4.9(b, c, d). Evidently the band of region (-1) in Fig.4.9(c) that is slightly less broad than that associated with region $(+1)$, since we have employed the driving field corresponding to the latter region. The small depressions in Fig.4.9(a) occur in regions of high absorption and can therefore be neglected.

Accordingly the procedure of this section efficiently produces three different white light bands in a single cavity. Additionally, the white light band of region (0) is activated though a driving field of 169.96γ while to activate the (±1) regions the driving field is found to equal 180.1415γ. This enables the optical switching of the bands.

4.8.2 Method B

In the last section 4.8.1, three white bands were generated subject to the condition $\omega_{ab} \approx 0$. This and the following section instead outline two procedures for generating three bands in which the value of ω_{ab} is not constrained. The first of these procedures assumes that the length of the cavity can be altered. In this case, the cavity condition, Eq.(4.14), for region (0) reads

$$L_0 W = cm\pi, \quad L_0 = \frac{m\pi c}{W}. \tag{4.59}$$

while the condition for the other two regions (±1) with varying length can be written as

$$L_\pm(W + \Delta_\pm) = cm\pi, \quad L_\pm = \frac{cm\pi}{W + \Delta_\pm}\frac{W}{W}, \tag{4.60}$$

and therefore

$$L_\pm = L_0\left(\frac{1}{1 + \frac{\Delta_\pm}{W}}\right) = L_0 X_\pm, \tag{4.61}$$

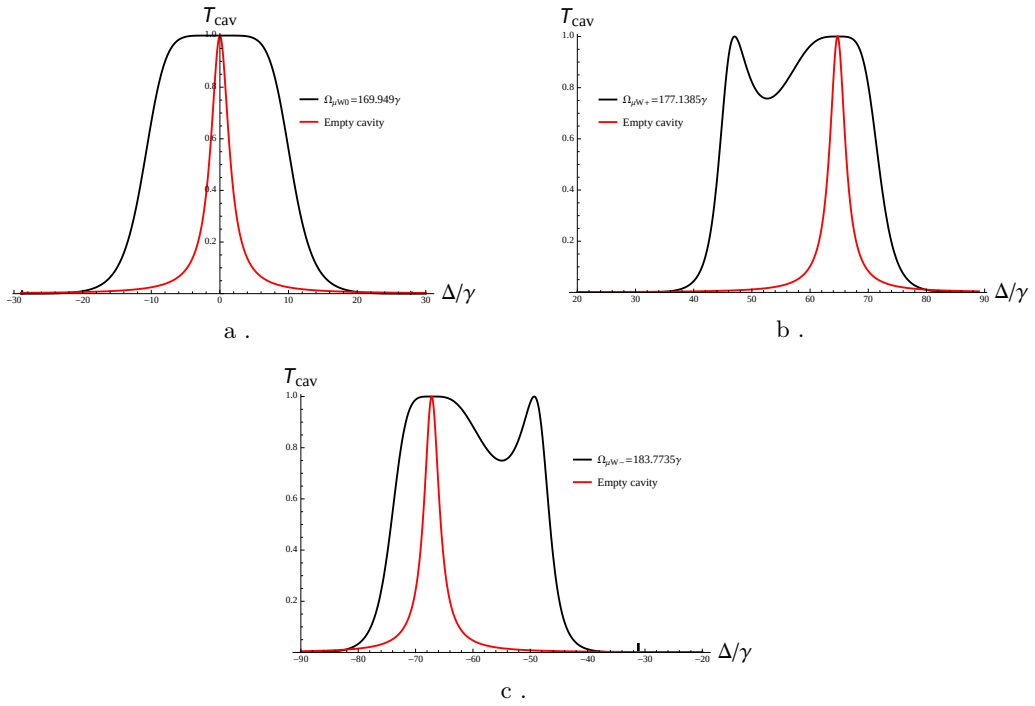

Figure 4.10: Magnified plots of the transmission bands of the cavity for differing driving field amplitudes with $\alpha = 3$ for cavity lengths (a) L_0 (b) $L_+ = L_0 X_+$ (c) $L_- = L_0 X_-$.

where $X_\pm$ are multiplicative factors that express the required length modifications. Setting ω_{ab} to its previous value, γ and calculating the driving fields that satisfy the white cavity condition for $\alpha = 3$ yields ($\Omega_{\mu W0} = 169.94\gamma$ $\Omega_{\mu W+} = 177.13\gamma$, $\Omega_{\mu W-} = 183.77\gamma$) for the [(0), (+1), (−1)] regions respectively. If the length of region (0) is set to $L_0 = 100\pi c/W$ the required lengths of the ($\pm$1) regions are $L_+ = 0.99993528 L_0$ and $L_- = 1.00006719 L_0$, which are sufficiently close to L_0 to enable the tuning of the cavity length.

The cavity transmission is plotted in Fig.(4.10) demonstrating three bands with very large linewidth ($\approx$ 1.0Ghz) compared to that of the previous method since the cavity length is reduced. Recall as well that for $\alpha = 1$, the band of region (0) is nearly unchanged but requires a smaller amplitude driving field as evident from Fig.4.8(b). Further, as in the previous section, the centre frequency of the ($\pm$1) bands can be shifted by adjusting the $\mathcal{C}$ parameter. Hence here again both the linewidth and the centre of the transmitted bands can be easily manipulated.

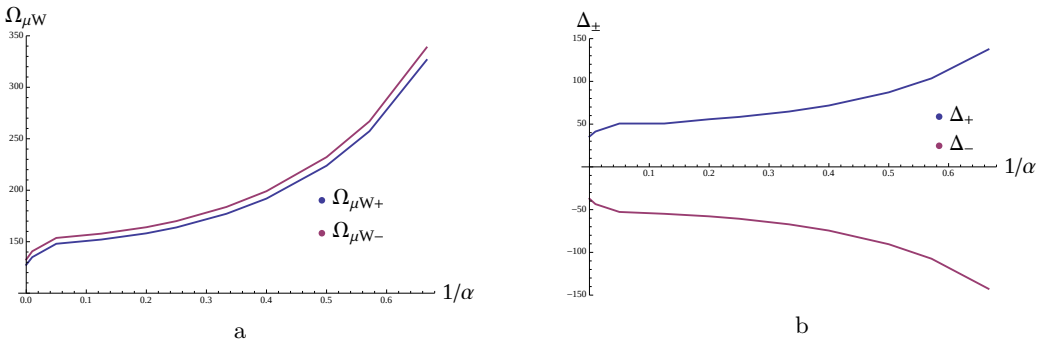

Figure 4.11: The (a) driving fields $\Omega_\mu^- = \Omega_{\mu W\pm}$ and (b) center point positions $\Delta_\pm$ resulting from the white light condition for the (± 1) regions plotted as a function of the ratio $1/\alpha$.

4.8.3 Method C

A third procedure for generating three white bands which employs $\alpha = 1$ is to tune the spacing energy ω_{ab}. We notice in Figs.4.7 that there are two peaks on either side of the transmission maximum. These peaks are related to ω_{ab} as they vanish for $\omega_{ab} = 0$. Increasing ω_{ab} therefore results in three white bands similar to the $\alpha \neq 1$ case. The width of both regions (± 1) approximately equals ω_{ab}, while the bandwidth of the middle region (0) is $\Omega_\mu^- \approx \omega_{ab}$. Therefore, when $\Omega_\mu^- \approx 2\omega_{ab}$, the three regions will possess almost the same width. This method could be highly efficient if ω_{ab} is easily tunable and illustrates that three bands can be generated even for equal amplitude driving fields.

4.9 One white band with adjustable center frequency

Finally, we propose a technique for generating a single large white band with a centre frequency that can be displaced by adjusting the parameter α. We specialize here to **method B**, for which $\omega_{ab} = \gamma$. Solving for the white cavity condition Eq.(4.53) along with $\chi' = 0$, yields the value of the field that satisfies the WLC condition $\Omega_{\mu W\pm}$ as well as the centre point $\Delta_\pm$ for each value of α. These results are shown in Fig.(4.11), where the left figure Fig.4.11(a), plots $\Omega_{\mu W\pm}$ against the ratio $1/\alpha$ while the right figure, Fig.4.11(b), displays the dependence of the centre point location on of the same ratio. Fig.4.11(a) demonstrates that there is almost a constant spacing between $\Omega_{\mu W-}$ and $\Omega_{\mu W+}$, which is expected since ω_{ab} is not negligible, as discussed in Sec.(4.8.1). Further, both $\Omega_{\mu W\pm}$ increase rapidly as α approaches 1 as the widths of the (± 1) regions decrease in this limit and vanish when $\alpha = 1$. The position of the center points in Fig.4.11(b) behaves similarly.

The above figures can be employed as follows. To position the white light band around a given centre point, e.g. $\Delta_{\pm} = x$ the value of α can be determined from Fig.4.11(b) and the required driving fields Ω_{μ}^{-} and $\Omega_{\mu}^{+} = \Omega_{\mu}^{-}/\alpha$ are then obtained from Fig.4.11(a). Finally, the cavity length must be adjusted to equal $L = X_{\pm}L_0$. A similar procedure for displacing the white band position can be formulated for **method A** however the resulting curves differ since ω_{ab} is altered in this scenario. The only positions which cannot be accessed fall in the interval $\approx -37.2\gamma$ to 35.5γ as evident from Fig.4.11(b). The two edges of this range correspond to $\alpha \to \infty$, which limits the two regions present in Fig.4.7(d).

4.10 Conclusion

This chapter has demonstrated that one, two or three white bands can be generated in a single cavity simply by adjusting the magnitude of the driving fields and the cavity length. Three separate techniques were given for three white band production, each of which has certain relative advantages and drawbacks. As well, the wavelength positions of the white light bands can be displaced through optical or mechanical tuning. These results can be employed to manipulate and control such systems in a more efficient fashion than previous techniques for single white light band systems in which the centre frequency could not be easily adjusted.

Future extensions of this work could include the generation of three simultanous white bands with only a single driving field amplitude. Additionally, for a larger set of interactions between the probe beam and the atom, the number of white cavity bands could in principle be further increased.

Chapter 5

N-Type Full Quantum Model

This chapter presents the full quantum theory of light-matter interactions from which quantum phenomena such as negative values of the Wigner function, collapse and revival phenomenon, squeezed states, entanglement and anti-bunching can be studied [111, 112]. Such nonclassical properties are often exploited in quantum optics and other fields [51, 53, 113, 114] and will be examined in detail in this and the following chapter. Here we first introduce quantized light (photons) and the quantized version of the two-level system and then present our proposed scheme which consists of N-type atom interacting with a single light mode. After examining the inversion dynamics, linear entropy, Q-function and squeezing the chapter ends with a summary and conclusions.

5.1 Background

In this section, we are interested in deriving the quantum equations for single light mode confined in a one-dimensional cavity with perfect mirrors at the boundaries, c.f. Fig.(5.1)

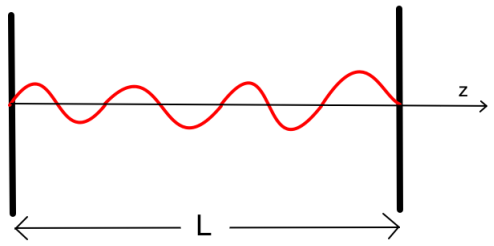

Figure 5.1: The one-dimensional cavity.

For an e.g. x-polarized electric field $E(z,t)$ with perfect mirrors at the boundaries so that

$E_x(0,t) = E_x(L,t)$. A longitudinal modal is given from Maxwell's equations as

$$E_x(z,t) = A_0 \sin(k_m z) q(t), \tag{5.1}$$

where A_0 is the amplitude of the field , $q(t)$ is the time-dependent function of the field which has a unit of length with $k_m = m\pi/L$ (see Eq.(4.13)). The value of m can be zero or any positive or negative integer. There is an infinite number of modes which can fit inside the cavity. However, here we only consider one mode of these. The accompanying magnetic induction from Maxwell's equations is then

$$B_y(z,t) = \frac{\mu_0 \epsilon_0}{k_m} A_0 \cos(k_m z) \dot{q}(t). \tag{5.2}$$

Now, the classical Hamiltonian of the fields in our system can be written as

$$H = \frac{1}{2} \int dV \left[\epsilon_0 E_x^2(z,t) + \frac{1}{\mu_0} B_y^2(z,t) \right]. \tag{5.3}$$

Substituting our fields and considering the volume of the cavity to be $V = L \int dxdy$, Eq.(5.3) becomes

$$H = \frac{\epsilon_0 V A_0^2}{4\omega^2} [\dot{q}(t)^2 + \omega^2 q(t)^2]. \tag{5.4}$$

Here $\int dxdy$ represents the cross-sectional area of the mode, so that V is the total volume of the mode inside the cavity. To transform this classical expression into a quantum mechanics formula, consider $q(t) = q$ as a canonical position, so that $\dot{q}(t) = p$ is the canonical momentum with unit mass. Also, to simplify the analogy with quantum mechanics rewrite the amplitude A_0 as $\sqrt{2\omega^2/(V\epsilon_0)}$. After the substitution, H will be

$$H = \frac{1}{2}(p^2 + \omega^2 q^2). \tag{5.5}$$

The Hamiltonian now is equivalent to that of a unit mass harmonic oscillator. The Hamiltonian in this form is still classical, but to quantize it, we need to impose the canonical commutation relation (first quantization)

$$[\hat{q}, \hat{p}] = \hat{q}\hat{p} - \hat{p}\hat{q} = i\hbar. \tag{5.6}$$

Inserting this commutation relation to the Hamiltonian yields

$$\hat{H} = \frac{1}{2}(\hat{p}^2 + \omega^2 \hat{q}^2). \tag{5.7}$$

This differs from the classical Eq.(5.5) in that $\hat{q}$ and $\hat{p}$ are now Hermitian operators that satisfy the commutation relations. It is more convenient however to write the Hamiltonian in terms of the non-Hermitian annihilation ($\hat{a}$) and creation ($\hat{a}^\dagger$) operators defined as

$$\hat{a} = \frac{1}{\sqrt{2\hbar\omega}}(\omega\hat{q} + i\hat{p}), \qquad \hat{a}^\dagger = \frac{1}{\sqrt{2\hbar\omega}}(\omega\hat{q} - i\hat{p}). \tag{5.8}$$

which from Eq.(5.6) satisfy the commutation relation

$$[\hat{a}, \hat{a}^\dagger] = 1. \tag{5.9}$$

In terms of these non-Hermitian operators, the Hamiltonian reads

$$\hat{H} = \hbar\omega\left(\hat{a}^\dagger\hat{a} + \frac{1}{2}\right). \tag{5.10}$$

Following the same procedure, the electric and magnetic fields become

$$\hat{E}_x(z,t) = \mathcal{E}_0(\hat{a} + \hat{a}^\dagger)\sin(kz), \qquad \hat{B}_y(z,t) = -i\mathcal{B}_0(\hat{a} - \hat{a}^\dagger)\cos(kz), \tag{5.11}$$

in which $\mathcal{E}_0 = \sqrt{\hbar\omega/(\epsilon_0 V)}$ and $\mathcal{B}_0 = (\mu_0/k)\sqrt{\epsilon_0\hbar\omega^3/V}$ with units of electric and magnetic field respectively. These fields are now represented as operators implying that only their expectation values can be measured.

The eigenvalue equation corresponding to the Hamiltonian $\hat{H}$ is then

$$\hat{H}|n\rangle = \hbar\omega\left(\hat{a}^\dagger\hat{a} + \frac{1}{2}\right)|n\rangle = \hbar\omega\left(n + \frac{1}{2}\right)|n\rangle = E_n|n\rangle, \tag{5.12}$$

where the eigenfunctions, $|n\rangle$, they termed Fock states, and the eigenvalues E_n represent the energy of the corresponding state. Here n varies from 0 to infinity, where 0 represents the vacuum state $|0\rangle$ (no photons). Hence n photons can exist in a single frequency and polarization light mode with energy E_n. In deriving Eq.(5.12) we employed that $\hat{a}^\dagger\hat{a}$ is the number operator $\hat{n}$ which satisfies

$$\hat{n}|n\rangle = \hat{a}^\dagger\hat{a}|n\rangle = n|n\rangle. \tag{5.13}$$

The Fock states will be discussed in the next section.

Our previous derivations were mostly limited to a single mode inside a cavity. But for travelling modes or multi-modes, additional expressions need to be introduced. Writing the quantized electric field as [51, 53, 115],

$$\hat{\mathbf{E}}(\mathbf{r},t) = \sum_{\mathbf{k},s} \sqrt{\frac{\hbar\omega_k}{2\epsilon_0 V}} \mathbf{e}_{\mathbf{k},s} \left[\hat{a}_{\mathbf{k},s} e^{i(\mathbf{k}\cdot\mathbf{r}-\omega_k t)} + \hat{a}^\dagger_{\mathbf{k},s} e^{-i(\mathbf{k}\cdot\mathbf{r}-\omega_k t)} \right], \tag{5.14}$$

where $\mathbf{k}$ is a wavevector, s denotes the electric field polarization and $\mathbf{e}_{\mathbf{k},s}$ is a unit vector in the direction of polarization of the mode. And $\hat{a}_{\mathbf{k},s}$ ($\hat{a}^\dagger_{\mathbf{k},s}$) is the corresponding annihilation (creation) operator. These non-Hermitian operators satisfy the following commutation relations

$$[\hat{a}_{\mathbf{k},s}, \hat{a}_{\mathbf{k}',s'}] = [\hat{a}^\dagger_{\mathbf{k},s}, \hat{a}^\dagger_{\mathbf{k}',s'}] = 0, \qquad [\hat{a}_{\mathbf{k},s}, \hat{a}^\dagger_{\mathbf{k}',s'}] = \delta_{\mathbf{k}\mathbf{k}'}\delta_{ss'}. \tag{5.15}$$

which again result from the first quantization of the canonical variables $\hat{q}$ and $\hat{p}$. Similarly, the magnetic field operator is

$$\hat{\mathbf{B}}(\mathbf{r},t) = \frac{1}{\mu_0} \sum_{\mathbf{k},s} \sqrt{\frac{\hbar\omega_k}{2\epsilon_0 V}} \left(\frac{\mathbf{k} \times \mathbf{e}_{\mathbf{k},s}}{\omega_k} \right) \left[\hat{a}_{\mathbf{k},s} e^{i(\mathbf{k}\cdot\mathbf{r}-\omega_k t)} + \hat{a}^\dagger_{\mathbf{k},s} e^{-i(\mathbf{k}\cdot\mathbf{r}-\omega_k t)} \right]. \tag{5.16}$$

To take into account a continuous distribution of travelling modes, the summation must be replaced by an integral as

$$\sum_{\mathbf{k},s} \to 2\frac{V}{(2\pi)^3} \int dk^3. \tag{5.17}$$

5.1.1 Fock states

Examining next the Fock or number states, which are simultaneous eigenfunctions of the field Hamiltonian $\hat{H}$ and the number operator $\hat{n}$ according to Eqs.(5.12) and (5.13), we can derive

$$\hat{a}|n\rangle = \sqrt{n}|n-1\rangle, \qquad \hat{a}^\dagger|n\rangle = \sqrt{n+1}|n+1\rangle, \qquad \hat{a}|0\rangle = 0. \tag{5.18}$$

From the first two equations, we can see that operator $\hat{a}$ annihilates one photon, while $\hat{a}^\dagger$ creates one photon. Further, applying the annihilation operator to the vacuum yields $\hat{a}|0\rangle = 0$ as expected.

Starting from the vacuum state $|0\rangle$ all Fock states can be obtained through the following relation

$$|n\rangle = \frac{(\hat{a}^\dagger)^n}{\sqrt{n}}|0\rangle. \tag{5.19}$$

The Fock states further form a complete and orthogonal basis since

$$\sum_{n=0}^{\infty} |n\rangle\langle n| = 1, \qquad\qquad \langle n|m\rangle = \delta_{nm}. \tag{5.20}$$

Therefore, any state of a single mode can be expressed as a superposition of Fock states as $|\psi\rangle = \sum_{n=0}^{\infty} c_n|n\rangle$, where the coefficients c_n obey the normalization condition, $\langle\psi|\psi\rangle = \sum_{n=0}^{\infty} |c_n|^2 = 1$.

Further, the quadrature operators $\hat{X}$ and $\hat{Y}$ defined as

$$\hat{X} = \frac{\hat{a} + \hat{a}^\dagger}{2}, \qquad\qquad \hat{Y} = \frac{\hat{a} - \hat{a}^\dagger}{2i}. \tag{5.21}$$

are directly related to the position ($\hat{q}$) and momentum ($\hat{p}$) operators which is evident if Eq.(5.8) is solved for these operators. They are also directly related to the electric and magnetic fields according to Eqs.(5.11). Although the expectation value of these two operators with respect to the number states $\langle n|\hat{X}|n\rangle = \langle n|\hat{Y}|n\rangle = 0$, yields zero. However, the expectation of their squares yields

$$\langle \hat{X}^2\rangle = \frac{1}{4}(2n+1), \qquad\qquad \langle \hat{Y}^2\rangle = \frac{1}{4}(2n+1), \tag{5.22}$$

where $\langle\hat{\mathcal{O}}\rangle = \langle n|\hat{\mathcal{O}}|n\rangle$. Since the uncertainty of an operator is given by $\langle(\Delta\hat{\mathcal{O}})^2\rangle = \langle\hat{\mathcal{O}}^2\rangle - \langle\hat{\mathcal{O}}\rangle^2$, the uncertainty of the quadrature operators of the number states equals

$$\langle(\Delta\hat{X})^2\rangle = \langle(\Delta\hat{Y})^2\rangle = \frac{1}{4}(2n+1). \tag{5.23}$$

Hence the fluctuations of both $\hat{X}$ and $\hat{Y}$ are increaseing as the number of photons n is increased so that the minimum uncertainty, 1/4, occurs when $n = 0$ (the vacuum state). Multiplying the uncertainties $\langle(\Delta\hat{X})^2\rangle\langle(\Delta\hat{Y})^2$ of the vacuum state yields 1/16, which equals the minimum fluctuations of the quadrature operators of any quantum state as the following inequality shows

$$\langle(\Delta\hat{X})^2\rangle\langle(\Delta\hat{Y})^2\rangle \geq \frac{1}{16}. \tag{5.24}$$

This inequality is a quantum mechanical property as it constitutes one form of the Heisenberg uncertainty principle.

5.1.2 Coherent states

Coherent states are the states that are most similar to classical coherent states. In contrast, the expectation value of the quadrature operators, which related to electric and magnetic fields, for the number states are always zero, which is far from classical since we classically expect that the electric field increases with the number of photons. Therefore, the number state does not possess the properties of classical states.

The coherent states can be calculated from the eigenvalue equation

$$\hat{a}|\alpha\rangle = \alpha|\alpha\rangle, \tag{5.25}$$

where $|\alpha\rangle$ is the coherent state, and α is a parameter that can take any complex value. Solving this equation together with the normalization condition yields

$$|\alpha\rangle = e^{-\frac{|\alpha|^2}{2}} \sum_{n=0}^{\infty} \frac{\alpha^n}{\sqrt{n!}}|n\rangle. \tag{5.26}$$

This state, which is normalized such that $\langle\alpha|\alpha\rangle = 1$, constitutes an infinite superposition of Fock states. It first introduced by Glauber in 1963 and sometimes called the Glauber coherent state [116]. The average number of photons in the coherent state is $\langle\alpha|\hat{n}|\alpha\rangle = \langle\hat{n}\rangle = |\alpha|^2$, so the parameter α is related to the number of photons.

The quadrature operators follow from Eq.(5.25) which yields for coherent states,

$$\langle\hat{X}\rangle = \mathrm{Re}(\alpha), \qquad \langle\hat{Y}\rangle = \mathrm{Im}(\alpha). \tag{5.27}$$

with fluctuations

$$\langle(\Delta\hat{X})^2\rangle = \langle(\Delta\hat{Y})^2\rangle = \frac{1}{4}. \tag{5.28}$$

The equations (5.27) and (5.28) again are similar to the properties of the classical coherent state as the averages are proportional to the real and imaginary value of α. Hence increasing the number of photons increases the quadrature $\langle\hat{X}\rangle$ or $\langle\hat{Y}\rangle$ and thus the electric and magnetic fields consistent with the properties of coherent classical fields. Further the fluctuations are a minimum as in classical fields.

Since the coherent state consists of a superposition of an infinite number of states, the probability

of finding n photons in the state is given by

$$P_n = |\langle n|\alpha\rangle|^2 = e^{-|\alpha|^2}\frac{|\alpha|^{2n}}{n!} = e^{-\langle\hat{n}\rangle}\frac{\langle\hat{n}\rangle^n}{n!}. \tag{5.29}$$

which is a Poisson distribution for which the mean number of photons equals $\langle\hat{n}\rangle$. The fluctuations of the number operator is found to be $\langle(\Delta\hat{n})\rangle = \sqrt{\langle\hat{n}\rangle} = |\alpha|$. Since the Poisson distribution is expected for a classical coherent state [117], this further confirms that the coherent state is the quantum analogue of the classical coherent state and in fact coincides with the classical coherent state in the $\alpha \to \infty$ limit.

It should be noted that the coherent state can also be defined as

$$|\alpha\rangle = \hat{D}(\alpha)|0\rangle = e^{\alpha\hat{a}^\dagger - \alpha^*\hat{a}}|0\rangle, \tag{5.30}$$

where $\hat{D}(\alpha)$ is the displacement operator, which is is equivalent to Eq.(5.25). The displacement operator is unitary since $\hat{D}(\alpha)\hat{D}^\dagger(\alpha) = \hat{D}^\dagger(\alpha)\hat{D}(\alpha) = 1$. While we have briefly illustrated above the quantum states that are most relevant to this thesis, numerous other important quantum states exist, such as those generated by thermal fields, single and two mode squeezed states, and so on.

5.1.3 Jaynes-Cummings model (JCM)

To introduce the quantized description of light-matter interactions we first describe the Jaynes-Cummings model (JCM) [118] which relates to a single electromagnetic mode interacting with a two-level atom in a cavity. The model, which applies the rotating wave approximation (RWA) and the dipole approximation within a full quantum description is exactly solvable, and reproduces numerous experimental observations [119]. The Hamiltonian of an atom interacting with electromagnetic fields can be written as

$$\hat{H} = \hat{H}_{atom} + \hat{H}_{field} + \hat{H}_{interaction}. \tag{5.31}$$

in which the first term $\hat{H}_{atom}$ is the atomic Hamiltonian. Considering only N levels the atom yields, by extending the analysis of the two-level system, c.f. for example Eq.(3.24) in Ch.(3),

$$\hat{H}_{atom} = \hbar\sum_{i=1}^{N}\omega_i|i\rangle\langle i|, \tag{5.32}$$

where $\hbar\omega_i$ is the energy of the state $|i\rangle$. The field Hamiltonian for K modes is

$$\hat{H}_{field} = \hbar \sum_{j=1}^{K} \Omega_j \left(\hat{a}_j^\dagger \hat{a}_j + \frac{1}{2} \right), \tag{5.33}$$

where Ω_j and $\hat{a}_j$ are the frequency and creation operator of mode j. The interaction Hamiltonian, as in Eq.(3.13), can then be written as $\hat{H}_{interaction} = -e\mathbf{r} \cdot \mathbf{E}(t)$. Inserting the identity operator $\sum_{i=1}^{N} |i\rangle\langle i| = 1$, the operator $e\mathbf{r}$ can be expressed as

$$e\mathbf{r} = \sum_{i=1}^{N} \sum_{j=1}^{N} |i\rangle\langle i|e\mathbf{r}|j\rangle\langle j| = \sum_{i=1}^{N} \sum_{j=1}^{N} \mathbf{d}_{ij}|i\rangle\langle j|, \tag{5.34}$$

where $\mathbf{d}_{ij}$ are dipole moment elements $e\langle i|\mathbf{r}|j\rangle$. In the full quantum description, the electric field $\mathbf{E}(t)$, analogous to Eq.(5.11) is given by

$$\mathbf{E} = \sum_{i=0}^{K} \mathcal{E}_i \mathbf{e}_i (\hat{a}_i + \hat{a}_i^\dagger), \tag{5.35}$$

where $\mathbf{e}_i$ and $\mathcal{E}_i$ are the polarization and electric amplitude of the ith field. We here assumed that the atom is at the origin $\mathbf{r}_0 = 0$. Then, the interaction Hamiltonian reads

$$\hat{H}_{interaction} = -e\mathbf{r} \cdot \mathbf{E}(t) = \hbar \sum_{i=1}^{N} \sum_{j=1}^{N} \sum_{s=1}^{K} g_s^{i,j} (\hat{a}_s + \hat{a}_s^\dagger)|i\rangle\langle j|, \tag{5.36}$$

where $g_s^{i,j}$ are the coupling constants which equal

$$g_s^{i,j} = -\frac{\mathbf{d}_{ij} \cdot \mathbf{e}_s \, \mathcal{E}_s}{\hbar}. \tag{5.37}$$

The Hamiltonian of the entire system is then

$$\hat{H} = \hbar \left(\sum_{i=1}^{N} \omega_i |i\rangle\langle i| + \sum_{j=1}^{K} \Omega_j \hat{a}_j^\dagger \hat{a}_j + \sum_{i=1}^{N} \sum_{j=1}^{N} \sum_{s=1}^{K} g_s^{i,j} (\hat{a}_s + \hat{a}_s^\dagger)|i\rangle\langle j| \right). \tag{5.38}$$

The energy of the vacuum, Eq.(5.33), is not present in the Hamiltonian as it is simply an additive constant.

We now specialize to the two-level scheme for which $N = 2$ and $K = 1$. Here we associate $|2\rangle$ with a single excited state, and $|1\rangle$ with the ground state. For simplicity, we assume the coupling

constants are real as $g_s^{i,j} = g_s^{j,i} = g$. The Hamiltonian then simplifies to

$$\hat{H} = \hbar \left[\omega_1 |1\rangle\langle 1| + \omega_2 |2\rangle\langle 2| + \Omega \hat{a}^\dagger \hat{a} + g(\hat{a} + \hat{a}^\dagger)(|1\rangle\langle 2| + |2\rangle\langle 1|\right]. \tag{5.39}$$

The interaction term (the term containing g) consists of four terms, $\hat{a}|1\rangle\langle 2|$, $a|2\rangle\langle 1|$, $\hat{a}^\dagger|1\rangle\langle 2|$ and $\hat{a}^\dagger|2\rangle\langle 1|$. Here $|2\rangle\langle 1|$ raises the ground state to the excited state, while $|1\rangle\langle 2|$ instead lowers the exited state. Therefore, to conserve energy, the energy nonconserving terms $\hat{a}^\dagger|2\rangle\langle 1|$ and $\hat{a}|1\rangle\langle 2|$ which respectively create a photon while exciting the atom and destroy a photon while deexciting the atom, are omitted. This corresponds in practice to applying the RWA to the full quantum models. The Hamiltonian then adopts the form

$$\hat{H} = \hbar \left[\omega_1 |1\rangle\langle 1| + \omega_2 |2\rangle\langle 2| + \Omega \hat{a}^\dagger \hat{a} + g(\hat{a}|2\rangle\langle 1| + \hat{a}^\dagger|1\rangle\langle 2|)\right]. \tag{5.40}$$

which is termed the Jaynes-Cummings model (JCM).

The Hamiltonian of Eq.(5.40) can now be expressed as a sum of two terms

$$\hat{H} = \hat{H}_0 + \hat{H}_I, \qquad \hat{H}_0 = \hbar(\omega_1 |1\rangle\langle 1| + \omega_2 |2\rangle\langle 2| + \Omega \hat{a}^\dagger \hat{a}), \qquad \hat{H}_I = g\hbar(\hat{a}|2\rangle\langle 1| + \hat{a}^\dagger|1\rangle\langle 2|). \tag{5.41}$$

which we transform into the interaction picture according to $e^{i\hat{H}_0 t/\hbar}\hat{H}_I e^{-i\hat{H}_0 t/\hbar}$. Employing the identity

$$\hat{\mathcal{H}} = e^{i\hat{H}_0 t/\hbar}\hat{H}_I e^{-i\hat{H}_0 t/\hbar} = \hat{H}_I + \left(\frac{it}{\hbar}\right)[\hat{H}_0, \hat{H}_I] + \frac{1}{2!}\left(\frac{it}{\hbar}\right)^2 [\hat{H}_0, [\hat{H}_0, \hat{H}_I]] + \cdots . \tag{5.42}$$

yields

$$\hat{\mathcal{H}} = g\hbar(\hat{a}e^{-i\Delta t}|2\rangle\langle 1| + \hat{a}^\dagger e^{i\Delta t}|1\rangle\langle 2|), \tag{5.43}$$

where $\Delta = \omega_2 - \omega_1 - \Omega$ is the detuning parameter.

The SE then takes the form

$$\frac{\partial|\psi\rangle}{\partial t} = -i\frac{\hat{\mathcal{H}}}{\hbar}|\psi\rangle, \tag{5.44}$$

where $|\psi\rangle$ represents the wave function of the entire system which, from the form of the Hamiltonian $\hat{\mathcal{H}}$, can be written as

$$|\psi\rangle = \sum_{n=0}^{\infty} q_n[A_{n+1}(t)|1, n+1\rangle + B_n(t)|2, n\rangle], \tag{5.45}$$

in which q_n is the probability amplitude of the incident light state. Inserting this wave function in the SE and taking the inner product with $\langle 1, n+1|$ and $\langle 2, n|$ yields two equations

$$\dot{A}_{n+1}(t) = -ig\sqrt{n+1}e^{i\Delta t}B_n(t), \qquad \dot{B}_n(t) = -ig\sqrt{n+1}e^{-i\Delta t}A_{n+1}(t). \tag{5.46}$$

Applying the transformation, $A_{n+1}(t) = \tilde{A}_{n+1}(t)e^{i\Delta t}$, yields

$$\dot{\tilde{A}}_{n+1}(t) = -i\Delta\tilde{A}_{n+1}(t) - ig\sqrt{n+1}B_n(t), \qquad B_n(t) = -ig\sqrt{n+1}\tilde{A}_{n+1}(t). \tag{5.47}$$

Which are coupled linear differential equations. To solve these, assume that $B_n(t)$ varies with time according to $e^{\mu t}$. Inserting this into the differential equations leads to

$$\mu_{1,2} = \frac{i}{2}\left[-\Delta \pm \sqrt{\Delta^2 + 4g^2(n+1)}\right]. \tag{5.48}$$

Then, setting $\tilde{A}_{n+1}(t) = a_1e^{\mu_1 t} + a_2e^{\mu_2 t}$ and $B_n(t) = b_1e^{\mu_1 t} + b_2e^{\mu_2 t}$, where a_1, a_2, b_1 and b_2 are undetermined coefficients satisfying

$$a_1 = \frac{-ig\sqrt{n+1}}{\mu_1 + i\Delta}b_1, \qquad a_2 = \frac{-ig\sqrt{n+1}}{\mu_2 + i\Delta}b_2. \tag{5.49}$$

If the atom is initially in the excited state $|2\rangle$, $B_n(0) = 1$ and $\tilde{A}_{n+1}(0) = 0$ so that $a_1 + a_2 = 0$ and $b_1 + b_2 = 1$ and the coefficients are

$$a_1 = -\frac{g\sqrt{n+1}}{\sqrt{\Delta^2 + 4g^2(n+1)}}, \qquad a_2 = \frac{g\sqrt{n+1}}{\sqrt{\Delta^2 + 4g^2(n+1)}},$$

$$b_1 = \frac{1}{2}\left(1 - \frac{\Delta}{\sqrt{\Delta^2 + 4g^2(n+1)}}\right), \qquad b_2 = \frac{1}{2}\left(1 + \frac{\Delta}{\sqrt{\Delta^2 + 4g^2(n+1)}}\right). \tag{5.50}$$

yielding finally

$$A_{n+1}(t) = \frac{g\sqrt{n+1}}{\sqrt{\Delta^2 + 4g^2(n+1)}}\left(e^{\mu_2 t} - e^{\mu_1 t}\right)e^{i\Delta t}. \tag{5.51}$$

$$B_n(t) = \frac{e^{\mu_2 t} + e^{\mu_1 t}}{2} + \frac{\Delta}{\sqrt{\Delta^2 + 4g^2(n+1)}}\left(\frac{e^{\mu_2 t} - e^{\mu_1 t}}{2}\right). \tag{5.52}$$

The dynamics of electrons within the two-level scheme can be illustrated through the inversion dynamics, where the inversion for our system is defined by $W(t) = \sum_{n=0}^{\infty} P_n\left[|B_n(t)|^2 - |A_{n+1}(t)|^2\right]$,

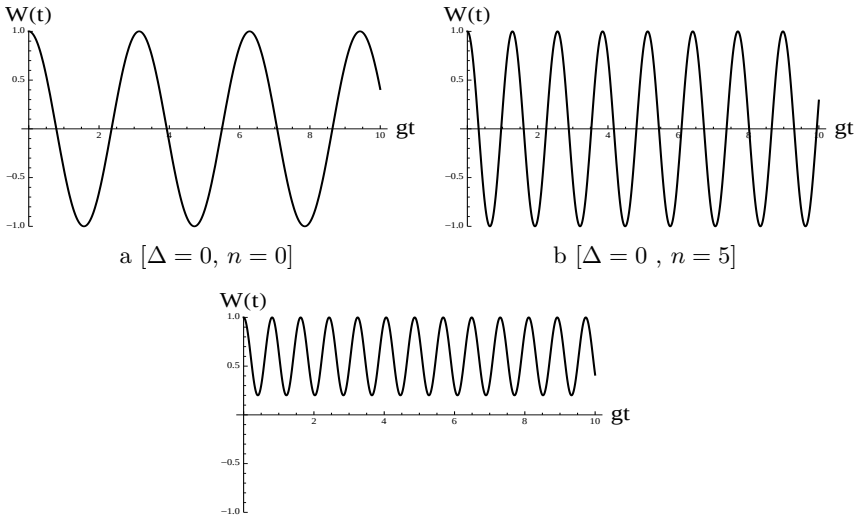

Figure 5.2: The inversion dynamics plotted against scaled time gt for various values of Δ and n.

in which $P_n = |q_n|^2$. If the initial state is the Fock state $|n\rangle$, $P_{n'} = \delta_{nn'}$ so

$$W(t) = \frac{\Delta^2 + 4g^2(n+1)\cos\left(\sqrt{\Delta^2 + 4g^2(n+1)}t\right)}{\Delta^2 + 4g^2(n+1)}. \tag{5.53}$$

The inversion dynamics for different system parameters is displayed in Fig.(5.2). All the inversion plots display ideal periodic oscillations termed Rabi oscillations at an angular frequency of $\Omega_n = \sqrt{\Delta^2 + 4g^2(n+1)}$. Although these oscillations are predicted by the semi-classical theory through the solution of Eq.(3.32), the Rabi oscillations in the full quantum treatment include vacuum oscillations with a frequency $\Omega_0 = \sqrt{\Delta^2 + 4g^2}$ as evident from Fig.(5.2a). This results from spontaneous emission which, unlike the classical theory, is inherent in the quantum theory. In Figs.(5.2b, 5.2c) we illustrate the effect of a non-zero photon number and a non-detuned field. In the later case, the excited state is more populated than the ground state.

If the initial state is a coherent state with $q_n = e^{-|\alpha|^2/2}\alpha^n/\sqrt{n!}$, the resultant inversion is

$$W(t) = \sum_{n=0}^{\infty}\left(e^{-|\alpha|^2}\frac{\alpha^{2n}}{n!}\right)\frac{\Delta^2 + 4g^2(n+1)\cos\left(\sqrt{\Delta^2 + 4g^2(n+1)}t\right)}{\Delta^2 + 4g^2(n+1)}. \tag{5.54}$$

In Fig.(5.3), we plotted this expression for two values of α ($\alpha = 3$ and 5) and for $\Delta = 0$. This generates discrete packets that undergo collapse and revival as a result of the coherent interaction

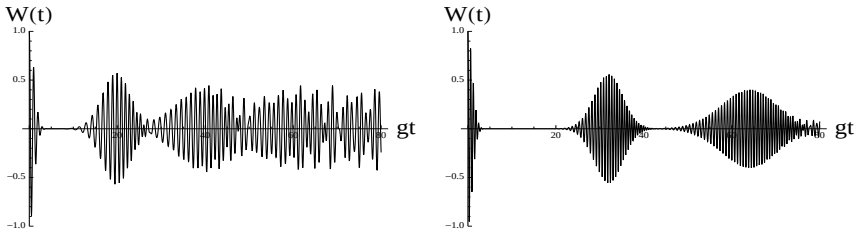

a [$\alpha = 3$] b [$\alpha = 5$]

Figure 5.3: The inversion dynamics as a function of scaled time gt for a two-level system for an initial coherent state. The field here is detuned with $\Delta = 0$.

between the different Rabi frequencies. This behavior cannot be reproduced classically as classical packets can collapse but will not be subsequently revived. As the amplitude α increases the packets become more pronounced as evident from the same figure. For all values of α, after a long scaled time gt, the packets overlap and become indistinguishable. This phenomenon has been observed experimentally [120, 121] and extensively analyzed theoretically. [122–125]. Additionally, effects such as entanglement between the field and the atom [126,127] and quadrature squeezing [128] have been studied and observed. Such phenomena will be discussed later in the context of our multi-level scheme.

5.2 Beyond JCM

The JCM has more recently been extended to multi-level atoms [129,130], multimode incident fields [131,132], multiple atoms [133,134] and intensity-dependent coupling [135]. Below we will investigate a multi-level scheme. Multi-level atoms exhibiting various nonlinear interactions are applied in many areas of quantum optics and quantum information science including electromagnetically induced transparency (EIT) [101,136], quantum jumps [137] and coherent population trapping (CPT) [138]. Nonlinear effects are incorporated into the JCM by introducing an intensity-dependent coupling between the atom and the electromagnetic field, [139, 140] which in turn experiences a nonlinear Kerr interaction [141]. Nonlinear effects can also arise from the f-deformed field of the deformed oscillations [135] or multi-photon processes with intensity-dependent coupling JCM [142]; however, these sources are not considered below. In three-level atomic schemes, the configurations V and Λ have been studied extensively for different nonlinear interactions including the interaction of two fields through a multi-photon process [143, 144] and intensity-depending coupling in Kerr medium

[145, 146]. Entanglement evolution has further been examined for Λ configurations with two fields through the cross-Kerr interaction [147].

Recently, the interaction of a four-level atom with a single field has been simulated in a fully quantized model [148–151]. Four level atoms can undergo numerous types of transitions including Y, λ, N and $\diamondsuit$ type and can exhibit nonclassical phenomena including collapse and revival, entanglement and the generation of anti-bunched photons [152, 153]. In particular, N-type systems were predicted to exhibit photon switching [154], as was subsequently verified experimentally [155, 156] as well as electromagnetically induced absorption (EIA) and electromagnetically induced transparency (EIT) [157, 158]. Also, some of these phenomena have been previously examined in the context of a fully quantized model of an atom interacting with a single mode of the electromagnetic field in the absence of an intensity-dependent coupling [159–162]. Most previous work however employed a superposition of two levels for the initial atomic state and did not investigate effects associated with intensity-dependent coupling or an initial state consisting of a single excited level.

In contrast to most four-level configurations the N and $\diamondsuit$ types are superpositions of the most common Λ and V three-level schemes. While the two schemes are mixed with effectively uncorrelated phases in the $\diamondsuit$-type configuration, they are instead superposed quasi-coherently in N-type, enhancing the resulting nonclassical properties.

Previous quantized model studies of N-type configurations either did not consider the case of an initial population in the most excited state, or assumed a specific excited state superposition that differs from that assumed below. As well, the effect of the intensity-dependent coupling in a Kerr medium has not been studied in the same manner as for e.g. Λ, V and $\diamondsuit$ systems. Accordingly, in this project the exact analytical solution of a N-type system interacting with a single-mode field in the presence of intensity-dependent coupling in a Kerr medium is obtained for an initially excited atom and a field in a coherent state. The nonclassicality of the system is characterized by computing the atomic inversion, which is directly related to the collapse and revival behaviour, the linear entropy which quantifies the degree of entanglement (DEM) between the field and the atom, the Q Mandel parameter that indicates if the field is bunched or anti-bunched as well as the standard squeezing parameter are subsequently analyzed.

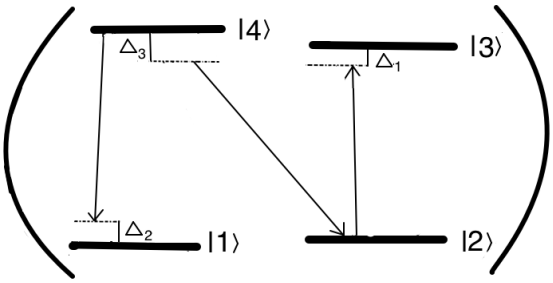

Figure 5.4: N-type configuration of a four-level atom

5.3 N-type four-level atom

Assume having a large Q cavity filled by N-type four-level atoms as illustrated by Fig.(5.4). In this figure, the uppermost atomic level is denoted by $|4\rangle$ while the ground states are $|1\rangle$ and $|2\rangle$. A single-mode field couples $|2\rangle - |3\rangle$, $|1\rangle - |4\rangle$, and $|2\rangle - |4\rangle$ with detunings Δ_1, Δ_2 and Δ_3, respectively while the $|3\rangle - |1\rangle$ transition is forbidden. The model therefore consists of two sub-coupled three-level systems Λ and V, where $|3\rangle$, $|2\rangle$ and $|4\rangle$ constitute a V-type system, and $|1\rangle$, $|4\rangle$ and $|2\rangle$ a Λ-type system. The field and atom coupling is intensity-dependent if the medium in the optical cavity possesses a Kerr nonlinearity.

An N-type scheme can be prepared by many methods [150, 163], one of which employs the four hyperfine levels of cesium (Cs) with D_2 line. The two ground states $|1\rangle$ and $|2\rangle$ correspond to the $(6^2S_{1/2})$ with $F = 3, 4$ while the upper states $|3\rangle$ and $|4\rangle$ instead are $(6^2P_{3/2})$ levels with $F' = 3, 4$. Although most experiments have employed three rather than one optical modes, since the spacing between the ground states and the upper states are nearly identical, the frequencies of the three fields can be almost indistinguishable, enabling the single mode approximation employed below. In this approximation, complicated measurements and higher order atom-photon interactions can be described by a straightforward and easily accessible formalism that could potentially be applied to numerous related research areas.

The full Hamiltonian which describes the system in the RWA is given by, with $\hbar$=1,

$$\hat{H} = \sum_{i=1}^{4} \omega_i \hat{R}_{ii} + \Omega \hat{a}^\dagger \hat{a} + g_a(\hat{A}^\dagger \hat{R}_{23} + \hat{A}\hat{R}_{32}) + g'_a(\hat{A}^\dagger \hat{R}_{14} + \hat{A}\hat{R}_{41}) + g_b(\hat{A}^\dagger \hat{R}_{24} + \hat{A}\hat{R}_{42}) + \chi \hat{a}^{\dagger 2}\hat{a}^2, \quad (5.55)$$

in which ω_i is the energy of the atomic level $|i\rangle$, $\hat{R}_{ij} = |i\rangle\langle j|$ is the lowering or raising operator of the

atomic system, Ω is the frequency of the single-mode field. g_a, g'_a and g_b are the atom-field coupling constants, χ is the third-order nonlinearity of the Kerr medium, and $\hat{A}$, $\hat{A}^\dagger$ are the deformation operators of the field defined as

$$\hat{A} = \hat{a}f(\hat{n}) = f(\hat{n}+1)\hat{a}, \qquad \hat{A}^\dagger = f(\hat{n})\hat{a}^\dagger = \hat{a}^\dagger f(\hat{n}+1). \tag{5.56}$$

Here the deformation function $f(\hat{n})$, which is a function of the number operator or equivalently the light intensity, describes the nature of the intensity-dependent coupling.

The Hamiltonian in Eq.(5.55) is conveniently expressed in the interaction picture after first writing $\hat{H} = \hat{H}_0 + \hat{H}_I$, where

$$\hat{H}_0 = \sum_{i=1}^{4} \omega_i \hat{R}_{ii} + \Omega \hat{a}^\dagger \hat{a}, \tag{5.57}$$

$$\hat{H}_I = g_a(\hat{A}^\dagger \hat{R}_{23} + \hat{A}\hat{R}_{32}) + g'_a(\hat{A}^\dagger \hat{R}_{14} + \hat{A}\hat{R}_{41}) + g_b(\hat{A}^\dagger \hat{R}_{24} + \hat{A}\hat{R}_{42}) + \chi \hat{a}^{\dagger 2}\hat{a}^2. \tag{5.58}$$

Then, the interaction Hamiltonian is found to be

$$\hat{\mathcal{H}} = g_a(\hat{A}^\dagger \hat{R}_{23} e^{i\Delta_1 t} + \hat{A}\hat{R}_{32} e^{-i\Delta_1 t}) + g'_a(\hat{A}^\dagger \hat{R}_{14} e^{i\Delta_2 t} + \hat{A}\hat{R}_{41} e^{-i\Delta_2 t}) + g_b(\hat{A}^\dagger \hat{R}_{24} e^{i\Delta_3 t} + \hat{A}\hat{R}_{42} e^{-i\Delta_3 t}) + \chi \hat{a}^{\dagger 2}\hat{a}^2, \tag{5.59}$$

where $\Delta_1 = \omega_3 - \omega_2 - \Omega$ $\Delta_2 = \omega_4 - \omega_1 - \Omega$, and $\Delta_3 = \omega_4 - \omega_2 - \Omega$ are the detuning parameters.

The dynamics of the system follow from the time-dependent Schrödinger equation which in the interaction picture adopts the form $(\partial/\partial t)|\psi\rangle = -i\hat{\mathcal{H}}|\psi\rangle$ where $|\psi\rangle$ is assumed to possess the following structure:

$$|\psi\rangle = \sum_{n=0}^{\infty} q_n [A_{n+1}(t)|1; n+1\rangle + B_{n+1}(t)|2; n+1\rangle + C_n(t)|3; n\rangle + D_n(t)|4; n\rangle], \tag{5.60}$$

Here $A_{n+1}(t)$, $B_{n+1}(t)$, $C_n(t)$ and $D_n(t)$ are the probability amplitudes of the states $|1\rangle$, $|2\rangle$, $|3\rangle$ and $|4\rangle$, respectively, and q_n is the initial probability amplitude of the single mode field. The equation of motion for the amplitudes is determined by substituting the state $|\psi\rangle$ into the Schrödinger equation. In the rotating frame, this yields the following equations:

$$\dot{A}_{n+1}(t) = -i[L_1 A_{n+1}(t) + F'_a D_n(t)], \tag{5.61}$$

$$\dot{B}_{n+1}(t) = -i[L_2 B_{n+1}(t) + F_a C_n(t) + F_b D_n(t)], \tag{5.62}$$

$$\dot{C}_n(t) = -i[L_3 C_n(t) + F_a B_{n+1}(t)], \tag{5.63}$$

$$\dot{D}_n(t) = -i[L_4 D_n(t) + F'_a A_{n+1}(t) + F_b B_{n+1}(t)], \tag{5.64}$$

where

$$F_a = \sqrt{n+1} f(n+1) g_a, \quad F'_a = \sqrt{n+1} f(n+1) g'_a, \quad F_b = \sqrt{n+1} f(n+1) g_b, \tag{5.65}$$

and

$$L_1 = A_1 + \Delta_1 + \Delta_2 - \Delta_3, \quad L_2 = A_1 + \Delta_1, \quad L_3 = A_2, \quad L_4 = A_2 + \Delta_1 - \Delta_3, \tag{5.66}$$

where

$$A_1 = \chi n(n-1), \qquad A_2 = \chi n(n+1). \tag{5.67}$$

Assuming that the amplitude $C_n(t)$ depends on time as $e^{\mu t}$, substituting into Eqs.(5.61-5.64) yields the fourth-order algebraic equation

$$\mu^4 + T_1 \mu^3 + T_2 \mu^2 + T_3 \mu + T_4 = 0, \tag{5.68}$$

where

$$\begin{aligned}
T_1 &= i(L_1 + L_2 + L_3 + L_4), \\
T_2 &= F_a^2 + F_a'^2 + F_b^2 - L_1 L_2 - L_1 L_3 - L_1 L_4 - L_2 L_3 - L_2 L_4 - L_3 L_4, \\
T_3 &= i[F_a^2 (L_1 + L_4) + F_a'^2 (L_2 + L_3) + F_b^2 (L_1 + L_3) - L_1 L_2 L_3 - L_1 L_2 L_4 - L_1 L_3 L_4 - L_2 L_3 L_4], \\
T_4 &= F_a^2 F_a'^2 + L_1 L_2 L_3 L_4 - F_a^2 L_1 L_4 - F_a'^2 L_2 L_3 - F_b^2 L_1 L_3.
\end{aligned} \tag{5.69}$$

The four roots of Eq.(5.68) are given by [164, 165]

$$\mu_{1,2} = \frac{1}{2}\left(-\sqrt{\lambda} \pm \sqrt{\lambda - 2\left(p + \lambda - \frac{q}{\lambda}\right)}\right) - \frac{T_1}{4}, \tag{5.70}$$

$$\mu_{3,4} = \frac{1}{2}\left(+\sqrt{\lambda} \pm \sqrt{\lambda - 2\left(p + \lambda + \frac{q}{\lambda}\right)}\right) - \frac{T_1}{4}, \tag{5.71}$$

where

$$\begin{aligned}
p &= T_2 - \tfrac{3T_1^2}{8}, \\
q &= T_3 - \tfrac{T_1 T_2}{2} + \tfrac{T_1^3}{8}, \\
r &= T_4 - \tfrac{T_1 T_3}{4} + \tfrac{T_1^2 T_2}{16} - \tfrac{3T_1^4}{256}, \\
\lambda &= \lambda_m = -\tfrac{x_1}{3} + \tfrac{2}{3}\sqrt{x_1^2 - 3x_2}\cos\left(\tfrac{1}{3}\cos^{-1}\left(\tfrac{9x_1x_2 - 2x_1^3 - 27x_3}{2(x_1^2-3x_2)^{3/2}}\right) + \tfrac{2\pi(m-1)}{3}\right), \\
x_1 &= 2p, \\
x_2 &= p^2 - 4r, \\
x_3 &= -q^2.
\end{aligned} \tag{5.72}$$

In Eq.(5.72) m represents one of the values {1,2,3} with λ given by the corresponding λ_m although $m = 2, 3$ is preferable. Since the $C_n(t)$ are linear combinations of terms that evolve in time as $e^{\mu_i t}$, the four probability amplitudes can be written as

$$A_{n+1}(t) = \sum_{i=1}^{4} J_i \frac{F_a'}{F_a F_b} \frac{(i\mu_i - L_2)(i\mu_i - L_3) - F_a^2}{(i\mu_i - L_1)} e^{(\mu_i + i(\Delta_1 + \Delta_2 - \Delta_3))t},$$

$$B_{n+1}(t) = \sum_{i=1}^{4} J_i \frac{(i\mu_i - L_3)}{F_a} e^{(\mu_i + i\Delta_1)t},$$

$$C_n(t) = \sum_{i=1}^{4} J_i e^{\mu_i t},$$

$$D_n(t) = \sum_{i=1}^{4} J_i \frac{(i\mu_i - L_2)(i\mu_i - L_3) - F_a^2}{F_a F_b} e^{(\mu_i + i(\Delta_1 - \Delta_3))t}. \tag{5.73}$$

These amplitudes are valid for any initial field q_n, deformation function $f(n)$, and initial atomic population. If the atomic system is initially in the most exited state $|4\rangle$, $D_n(0) = 1$, J_i equals

$$J_i = \frac{F_a F_b (iL_1 + \mu_i)}{(\mu_j - \mu_i)(\mu_k - \mu_i)(\mu_l - \mu_i)}, \qquad i \neq j \neq k \neq l. \tag{5.74}$$

5.4 Physical properties

From the exact analytical amplitudes of the previous section, which were verified both numerically and through a comparison with the limiting cases in [146, 147], the physical properties of the

system can be obtained. In particular, in this section the atomic inversion, linear entropy, Mandel Q-parameter and the normal squeezing are evaluated. Although several options exist for the nonlinearity function $f(n)$, the following three choices are employed

$$f_1(n) = 1, \qquad f_2(n) = \frac{1}{\sqrt{n}}, \qquad f_3(n) = \sqrt{n}. \tag{5.75}$$

The first function corresponds to the case of constant coupling (the standard generalization of the JCM) while the second option corresponds to the harmonious state (the nonlinear coherent state) which was first obtained in [166], and the third function is the root of n. As mentioned earlier, although the treatment below is specialized to these choices of nonlinear functions, the above equations are equally valid for arbitrary $f(n)$.

Assuming next that the initial state is the coherent state in which the value of $|\alpha|^2$ is taken to be 10 in the examples below. To simplify the analysis without affecting its generality, the remaining coupling parameters are assumed to equal $g_a = g'_a = g_b = g$, where the additional parameters are scaled by a constant proportional to g. In fact, setting the strength parameters nearly equal is physically justified since the energy differences between the ground state and each of the upper states are nearly identical. To study the effect of detuning, two different detuning constants D_1 and D_2 were examined, namely,

$$D_1 : \ \Delta_1 = 0, \Delta_2 = 0, \Delta_3 = 0, \qquad D_2 : \ \Delta_1 = 6g, \Delta_2 = 6g, \Delta_3 = 14g, \tag{5.76}$$

where D_1 corresponds to the field being in exact resonant with the system, while D_2 is set to a representative value of the detuning.

5.4.1 Population inversion

The evolution of the population of an atomic level system is governed by its degree of inversion. In particular, the population inversion can result in collapse and revival effects leading to discrete packets as we saw earlier in the two-level system. These packets, which are associated with the nonclassicality of multiple quantum interference in phase space were experimentally observed in [121].

For our scheme, the atomic inversion is defined as the difference between the population of the

exited state $|4\rangle$ and the remaining states

$$W(t) = \rho_{44} - (\rho_{33} + \rho_{22} + \rho_{11}), \tag{5.77}$$

In the above equation ρ_{ii} represents the population of the state $|i\rangle$. Defining $P_n = |q_n|^2$, the ρ_{ii} are given by

$$\begin{aligned}
\rho_{11} &= \sum_{n=0}^{\infty} P_n |A_{n+1}(t)|^2, \\
\rho_{22} &= \sum_{n=0}^{\infty} P_n |B_{n+1}(t)|^2, \\
\rho_{33} &= \sum_{n=0}^{\infty} P_n |C_n(t)|^2, \\
\rho_{44} &= \sum_{n=0}^{\infty} P_n |D_n(t)|^2,
\end{aligned} \tag{5.78}$$

in which $A_{n+1}(t)$, $B_{n+1}(t)$, $C_n(t)$, $D_n(t)$ are defined in Eq.(5.60).

Fig.(5.5) then depicts the dependence of the atomic inversion dynamics on the scaled time $\tau = gt$ for different values of the system parameters. In Figs.(5.5a,5.5b,5.5c,5.5d) the nonlinearity function $f(n) = 1$, while in Figs.(5.5e, 5.5f, 5.5g, 5.5h) $f(n) = 1/\sqrt{n}$, and $f(n) = \sqrt{n}$ in Figs.(5.5i, 5.5j, 5.5k, 5.5l).

Evidently from Fig.(5.5a), when the intensity-dependent coupling is not present, $f(n) = 1$, the inversion forms discrete packets with fluctuations that increase with time. However, in the presence of nonlinearity χ, the stability and periodicity of the packets in Fig.(5.5b) are enhanced by nonclassical effects. Modifying the second detuning parameter D_2, c.f. Fig.(5.5c) influences the collapse and revival periods through the three N-type couplings. Further, Fig.(5.5d) demonstrates that packet formation is suppressed at larger values of χ. In contrast for the intensity-dependent $f(n) = 1/\sqrt{n}$, the inversion oscillates periodically but packet formation is absent as evident from Fig.(5.5e) which covers the full range from -1 to 1 of the inversion. For small values of the Kerr nonlinearity as in Fig.(5.5f), small packets with pronounced fluctuations are generated. Increasing the second value of the detuning D_2 in Fig.(5.5g) generates periodic fluctuations for which the fourth state is heavily populated at all times. Introducing the Kerr nonlinearity in Fig.(5.5h) additionally results in a number of large amplitude packets. Finally, for $f(n) = \sqrt{n}$, narrow, high-frequency packets occur for a system detuning equal to D_1 as evident from Figs.(5.5i, 5.5j). However, for a

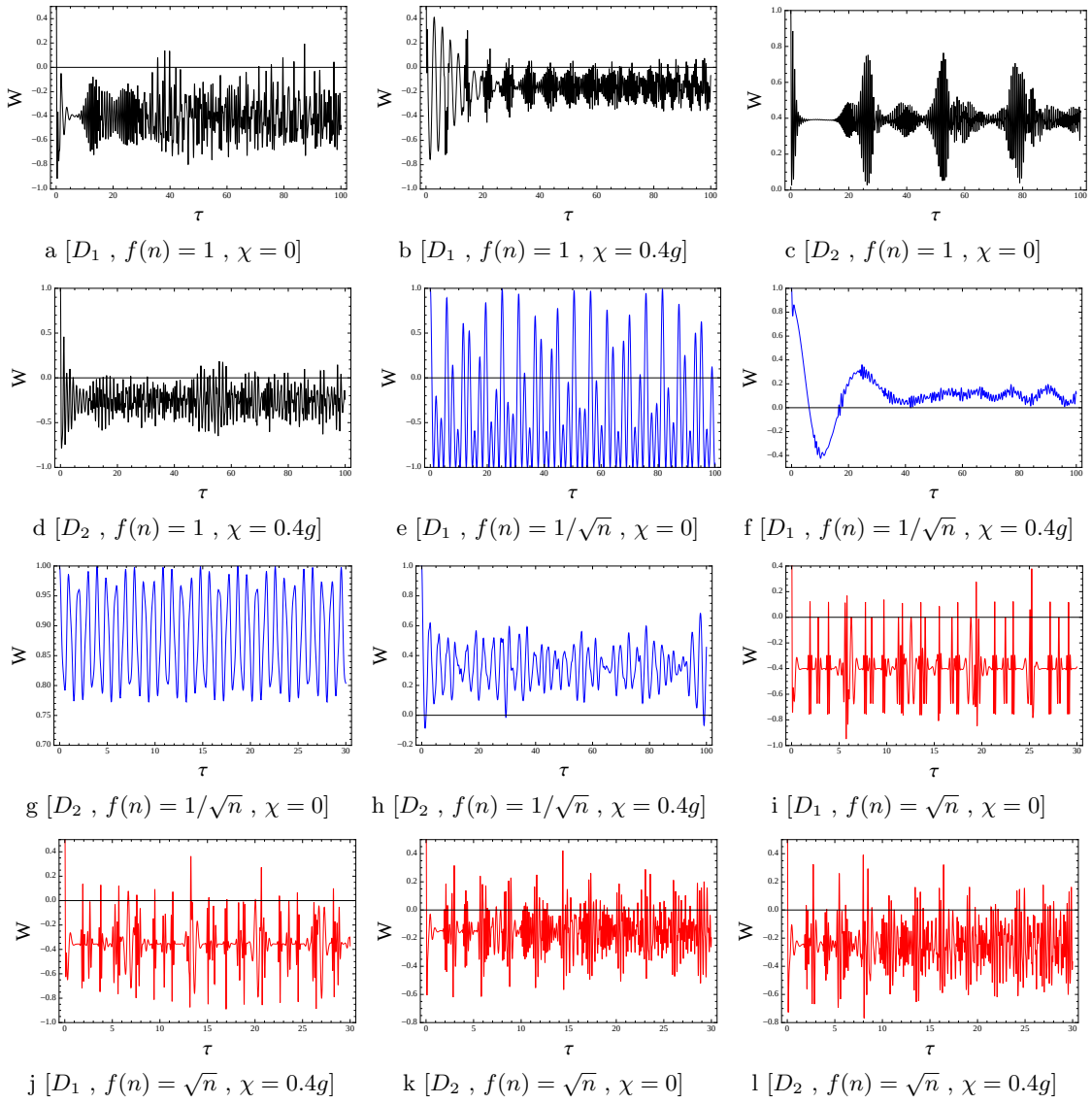

a $[D_1\ ,\ f(n)=1\ ,\ \chi=0]$ b $[D_1\ ,\ f(n)=1\ ,\ \chi=0.4g]$ c $[D_2\ ,\ f(n)=1\ ,\ \chi=0]$

d $[D_2\ ,\ f(n)=1\ ,\ \chi=0.4g]$ e $[D_1\ ,\ f(n)=1/\sqrt{n}\ ,\ \chi=0]$ f $[D_1\ ,\ f(n)=1/\sqrt{n}\ ,\ \chi=0.4g]$

g $[D_2\ ,\ f(n)=1/\sqrt{n}\ ,\ \chi=0]$ h $[D_2\ ,\ f(n)=1/\sqrt{n}\ ,\ \chi=0.4g]$ i $[D_1\ ,\ f(n)=\sqrt{n}\ ,\ \chi=0]$

j $[D_1\ ,\ f(n)=\sqrt{n}\ ,\ \chi=0.4g]$ k $[D_2\ ,\ f(n)=\sqrt{n}\ ,\ \chi=0]$ l $[D_2\ ,\ f(n)=\sqrt{n}\ ,\ \chi=0.4g]$

Figure 5.5: The inversion dynamics for various detuning parameters, Kerr coefficients and nonlinearity functions for $|\alpha|^2 = 10$.

detuning of D_2, the collapse and revival phenomenon yields the broader packets of Figs.(5.5k, 5.5l).

Since changing the Kerr coefficient modifies the collapse and revival behaviour for $f(n) = 1$ and $f(n) = 1/\sqrt{n}$, modifications to this coefficient, in principle, can be employed to modulate or extinguish this behaviour. While the same mechanism could also be applied to V-type and Λ-type atomic transitions, repeating the above calculations with either $g_a = 0$ or $g'_a = 0$, which correspond to Λ- and V- systems, respectively, indicated that the effect is far more enhanced in the N-type configuration.

5.4.2 Linear entropy

Entanglement refers to the mutual coupling of two subsystems described by a single wavefunction which can be composed of particles and/or fields. In the system considered here entanglement can occur between the field and the atom such that the state of one of these subsystems can be determined by measuring the state of the other subsystem. The degree of the entanglement (DEM) between the atom and the field can be quantified by the linear entropy defined as

$$S(t) = 1 - Tr(\hat{\rho}_A^2(t)). \tag{5.79}$$

Here the full density matrix of the system is written $\hat{\rho}_{AF}(t) = |\psi(t)\rangle\langle\psi(t)|$, while the density matrix of the atom is obtained from the trace over the field

$$\hat{\rho}_A(t) = Tr_F(\hat{\rho}_{AF}(t)) = \begin{pmatrix} \rho_{11} & \rho_{12} & \rho_{13} & \rho_{14} \\ \rho_{21} & \rho_{22} & \rho_{23} & \rho_{24} \\ \rho_{31} & \rho_{32} & \rho_{33} & \rho_{34} \\ \rho_{41} & \rho_{42} & \rho_{43} & \rho_{44} \end{pmatrix}. \tag{5.80}$$

The diagonal elements of the density matrix are introduced in Eq.(5.78), while the off-diagonal elements are

$$\rho_{12} = \sum_{n=0}^{\infty} q_n q_n^* A_{n+1} B_{n+1}^*,$$

$$\rho_{13} = \sum_{n=0}^{\infty} q_n q_{n+1}^* A_{n+1} C_{n+1}^*,$$

$$\rho_{14} = \sum_{n=0}^{\infty} q_n q_{n+1}^* A_{n+1} D_{n+1}^*,$$

$$\rho_{23} = \sum_{n=0}^{\infty} q_n q_{n+1}^* B_{n+1} C_{n+1}^*,$$

$$\rho_{24} = \sum_{n=0}^{\infty} q_n q_{n+1}^* B_{n+1} D_{n+1}^*,$$

$$\rho_{34} = \sum_{n=0}^{\infty} q_n q_n^* C_n D_n^*, \tag{5.81}$$

The remaining density matrix elements follow from the relation $\rho_{ij} = \rho_{ji}^*$. The linear entropy Eq.(5.79) is therefore

$$S(t) = 1 - [\rho_{11}^2 + \rho_{22}^2 + \rho_{33}^2 + \rho_{44}^2 + 2|\rho_{12}|^2 + 2|\rho_{13}|^2 + 2|\rho_{14}|^2 + 2|\rho_{23}|^2 + 2|\rho_{24}|^2 + 2|\rho_{34}|^2]. \tag{5.82}$$

Fig.(5.6) plots the linear entropy, Eq.(5.82), against the scaled time $\tau = gt$ for both detunings D_1 and D_2 and the parameters specified in Fig.(5.6). When the intensity-dependent coupling is constant, e.g. $f(n) = 1$ in Figs.(5.6a, 5.6b), the entropy approaches a steady state value of $0.6 - 0.7$ at long times. However, for the detuning of D_2 in Fig.(5.6c) the DEM instead increases with time while introducing a Kerr medium in Fig.(5.6d) significantly increases the steady-state value of the DEM to $\approx 0.5 - 0.7$, and rapidly stabilizes the entanglement compared to the $\chi = 0$ case for the same detuning as in Fig.(5.6c).

If the intensity-dependent coupling is instead $f(n) = 1/\sqrt{n}$ for $\chi = 0$, c.f. Fig.(5.6e), the DEM oscillates periodically in the range $0 - 0.0125$, while for a nonlinear coefficient $\chi = 0.4g$ the DEM in Fig.(5.6f) approaches a larger steady-state value of 0.5. For a detuning of D_2 and $\chi = 0$ in Fig.(5.6g), the DEM is small compared to 1, and attains a maximum of 0.0052. For $\chi = 0.4g$, Fig.(5.6h), the mean value, 0.4, of the DEM is however far greater than the mean value at $\chi = 0$. This demonstrates that the evolution of the DEM can be controlled or switched in a Kerr medium by modulating χ.

For the intensity-dependent coupling function $f(n) = \sqrt{n}$, the average value of the DEM approximates 0.6 for all cases. When the field is detuned with the atom D_1 as in Fig.(5.6i), the DEM exhibits numerous local minima. The addition of a non-zero Kerr coefficient in Fig.(5.6j) however reduces the number of these minima. For a detuning of D_2, the entropy instead adopts a nearly

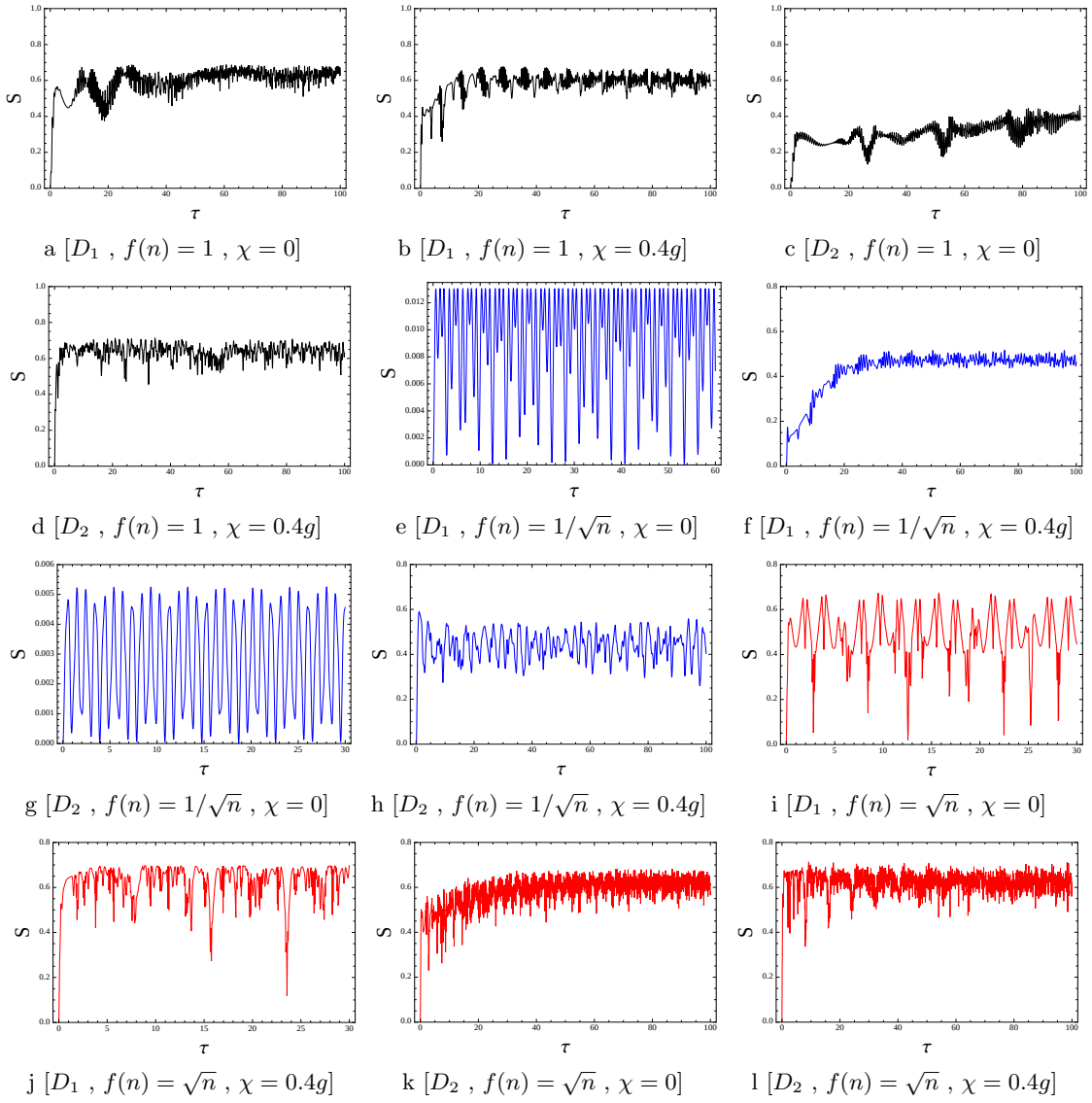

a $[D_1\ ,\ f(n)=1\ ,\ \chi=0]$ b $[D_1\ ,\ f(n)=1\ ,\ \chi=0.4g]$ c $[D_2\ ,\ f(n)=1\ ,\ \chi=0]$

d $[D_2\ ,\ f(n)=1\ ,\ \chi=0.4g]$ e $[D_1\ ,\ f(n)=1/\sqrt{n}\ ,\ \chi=0]$ f $[D_1\ ,\ f(n)=1/\sqrt{n}\ ,\ \chi=0.4g]$

g $[D_2\ ,\ f(n)=1/\sqrt{n}\ ,\ \chi=0]$ h $[D_2\ ,\ f(n)=1/\sqrt{n}\ ,\ \chi=0.4g]$ i $[D_1\ ,\ f(n)=\sqrt{n}\ ,\ \chi=0]$

j $[D_1\ ,\ f(n)=\sqrt{n}\ ,\ \chi=0.4g]$ k $[D_2\ ,\ f(n)=\sqrt{n}\ ,\ \chi=0]$ l $[D_2\ ,\ f(n)=\sqrt{n}\ ,\ \chi=0.4g]$

Figure 5.6: Linear entropy dynamics for selected values of the detuning, Kerr coefficients and nonlinearity functions with $|\alpha|^2 = 10$.

constant average value of 0.6 above $\tau \approx 20$ with superimposed fluctuations of magnitude 0.2. The introduction of a non-zero Kerr coefficient increases the stabilization time significantly to $\tau \approx 1.5$ and as well generates more pronounced packets.

Evidently, the N-type system typically exhibits an enhanced DEM while the presence of a Kerr medium stabilizes the entanglement for $f(n) = 1$ and $f(n) = \sqrt{n}$, while it can be employed to switch the DEM between on and off states for $f(n) = 1/\sqrt{n}$. Further, in comparison to the $\diamondsuit$-type interaction of [152], the N-type DEM is considerably less time-dependent than that of the $\diamondsuit$-type in the presence of a Kerr medium. Hence differing physical effects result when the V and Λ types are added coherently to generate a N-type system as opposed to incoherently resulting in $\diamondsuit$-type. The time-independence of the DEM can presumably be exploited in long time experimental measurements.

In summary, for the configuration examined above the DEM can often be increased or stabilized in the presence of a Kerr medium. Also, in the absence of an intensity-dependent coupling, $f(n) = 1$ or $f(n) = \sqrt{n}$, the DEM is larger compared to the nonlinear case, $f(n) = 1/\sqrt{n}$. Furthermore , for a deformation $f(n) = \sqrt{n}$ the behavior DEM is generally more affected by the detuning than by the other parameters investigated above. Collapse and revival also appear in all cases investigated except for Figs.(5.6e, 5.6g) and therefore appear to be a salient feature of the N-type system.

5.4.3 Q Mandel parameter

The degree of super- or sub- Poissonian statistics of nonclassical light is generally quantified by the Mandel parameter Q defined by [167]

$$Q = \frac{\langle \hat{n}^2 \rangle - \langle \hat{n} \rangle^2}{\langle \hat{n} \rangle} - 1. \tag{5.83}$$

If $Q > 0$ the field exhibits super-Poissonian statistics while for $Q < 0$ the field is sub-Poissonian. Further, the field is described by a coherent and a number state when $Q = 0$ and $Q = -1$ respectively. Sub-Poissonian statistics imply anti-bunching and thus the existence of a nonclassical field that has recently found numerous applications in quantum information theory. The basic idea of photon antibunching can be defined as follows. If a quantum light state is anti-bunched, then the photons of this state are more equally spaced in time and position than the coherent state [51, 115]. And one of the best measurements to quantify this phenomenon is the Q Mandel parameter.

To obtain Q, $\langle n^2\rangle$ and $\langle n\rangle$ are first evaluated directly from $|\psi(t)\rangle$ as

$$\langle\hat{n}\rangle = \sum_{n=0}^{\infty} P_n \left[(n+1)(|A_{n+1}|^2 + |B_{n+1}|^2) + n(|C_n|^2 + |D_n|^2)\right], \tag{5.84}$$

$$\langle\hat{n}^2\rangle = \sum_{n=0}^{\infty} P_n \left[(n+1)^2(|A_{n+1}|^2 + |B_{n+1}|^2) + n^2(|C_n|^2 + |D_n|^2)\right], \tag{5.85}$$

where P_n is $q_n q_n^*$.

Fig.(5.7) displays Q as a function of $\tau = gt$ for different values of χ and detuning parameters for the three deformation functions $f(n)$ of interest. While in most subplots $Q < 0$ indicating a sub-Poissonian field, for $f(n) = 1$, c.f. Figs.(5.7a, 5.7b, 5.7c, 5.7d) and $f(n) = \sqrt{n}$ (Figs.(5.7i, 5.7j, 5.7k, 5.7l), the Q-parameter varies between positive and negative values and hence sub- and super-Poissonian statistics. However, for the intensity-dependent coupling $f(n) = 1/\sqrt{n}$ in Fig.(5.7f), or in the absence of a Kerr medium, Figs.(5.7e, 5.7g), $Q < 0$ indicating uniform sub-Poissonian statistics. Thus, in general, media with $f(n) = 1/\sqrt{n}$ generate an increased percentage of anti-bunching photons compared to media with either $f(n) = 1$ or $f(n) = \sqrt{n}$. Full anti-bunching dynamics is in particular expected in N-type materials when $f(n) = 1/\sqrt{n}$ as is the case in the V, Λ and $\diamondsuit$ schemes. [146, 147, 152].

The negative values of the Q-parameter in the above results (which are close to those of the Λ-type system in [147]) are smaller than the typical values employed to characterize the V-type system of [146], $|Q_{N-type}| > |Q_{V-type}|$. This indicaties that the N-type system generates sub-Poissonian light more efficiently than V-type, especially when $f(n) = 1/\sqrt{n}$. Additionally, the Q parameter in our scheme is generally less negative compared to the $\diamondsuit$-type [152], but our scheme generates sub-Poissonian photons with fewer fluctuations in the presence of a Kerr medium. Therefore, the N-type system provides an excellent platform for anti-bunched light generation that can be controlled by adjusting the Kerr nonlinearity (for $f(n) = 1/\sqrt{n}$) or enhanced by letting the field at the resonant detuning, D_1 (for $f(n) = 1$ or $f(n) = \sqrt{n}$).

5.4.4 Linear squeezing

The multiplication of the uncertainties of the quadrature operators for the coherent state as in Eq.(5.28) always take the minimum possible value which is 1/16. However, if one of the quadrature uncertainties for any quantum state is lower than 1/4, then that state is said to be linearly squeezed.

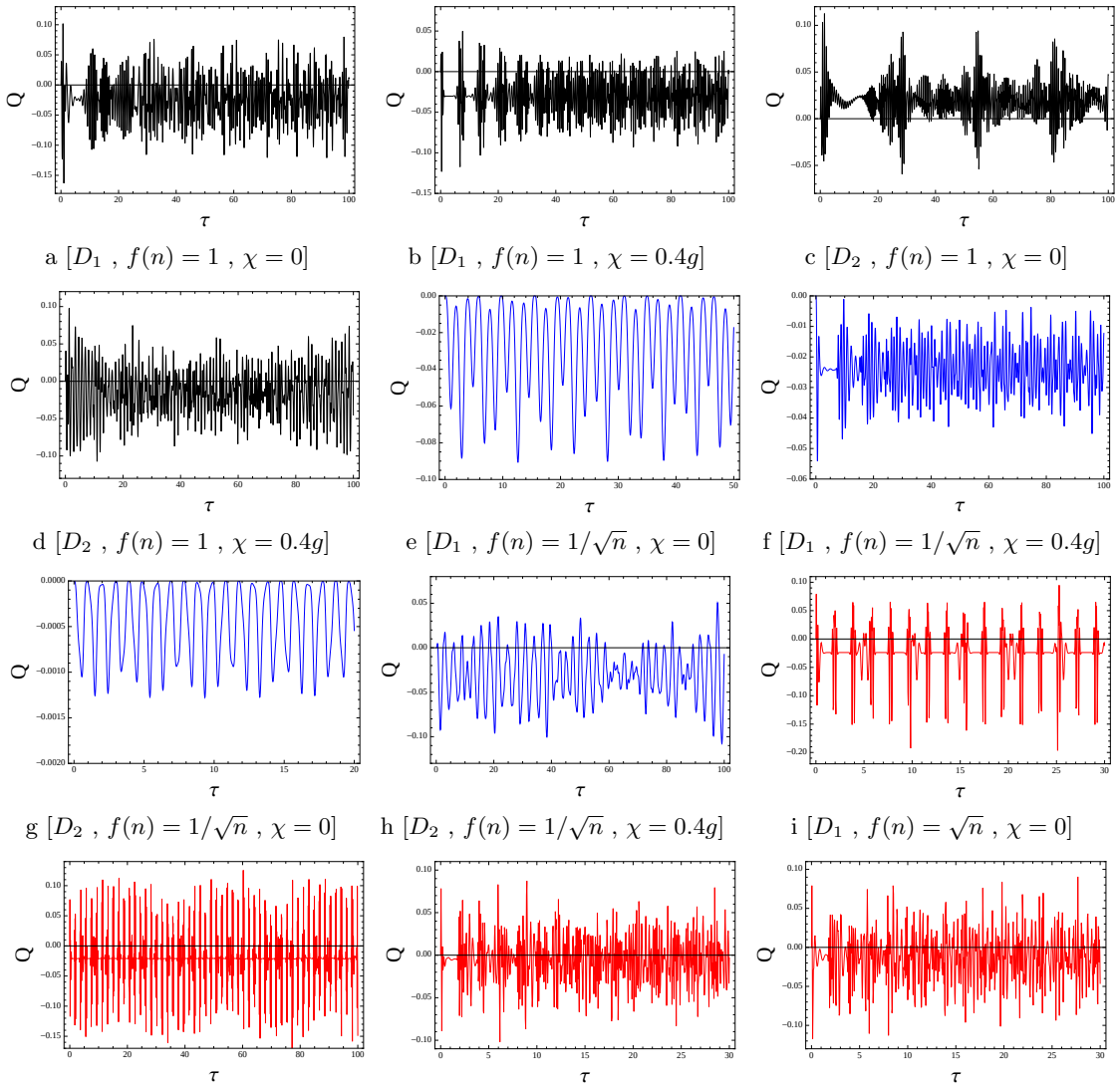

a $[D_1\ ,\ f(n)=1\ ,\ \chi=0]$ b $[D_1\ ,\ f(n)=1\ ,\ \chi=0.4g]$ c $[D_2\ ,\ f(n)=1\ ,\ \chi=0]$

d $[D_2\ ,\ f(n)=1\ ,\ \chi=0.4g]$ e $[D_1\ ,\ f(n)=1/\sqrt{n}\ ,\ \chi=0]$ f $[D_1\ ,\ f(n)=1/\sqrt{n}\ ,\ \chi=0.4g]$

g $[D_2\ ,\ f(n)=1/\sqrt{n}\ ,\ \chi=0]$ h $[D_2\ ,\ f(n)=1/\sqrt{n}\ ,\ \chi=0.4g]$ i $[D_1\ ,\ f(n)=\sqrt{n}\ ,\ \chi=0]$

j $[D_1\ ,\ f(n)=\sqrt{n}\ ,\ \chi=0.4g]$ k $[D_2\ ,\ f(n)=\sqrt{n}\ ,\ \chi=0]$ l $[D_2\ ,\ f(n)=\sqrt{n}\ ,\ \chi=0.4g]$

Figure 5.7: Q-parameter dynamics for different detuning, Kerr coefficients and nonlinearity functions for $|\alpha|^2 = 10$.

The squeezing is important for many future applications in quantum teleportation and accurate measurements. To measure the squeezing, we can use the squeezing parameter which is defined as [168, 169]

$$S_\theta = 4(\langle \hat{X}_\theta^2 \rangle - \langle \hat{X}_\theta \rangle^2) - 1 = 4(\Delta \hat{X}_\theta)^2 - 1, \tag{5.86}$$

in which $\hat{X}_\theta$ is the quadrature operator of angle θ defined as

$$\hat{X}_\theta = \frac{e^{-i\theta}\hat{a} + e^{i\theta}\hat{a}^\dagger}{2}. \tag{5.87}$$

If θ is zero ($\pi/2$), the quadrature operator is the space (momentum) operator. Here $S_\theta < 0$ and $S_\theta > 0$ for squeezed and unsqueezed states respectively. Expanding the squeezing parameter yields

$$S_\theta = e^{-2i\theta}\langle \hat{a}^2 \rangle + e^{2i\theta}\langle \hat{a}^{\dagger 2} \rangle + 2\langle \hat{a}^\dagger \hat{a} \rangle - (e^{-i\theta}\langle \hat{a} \rangle + e^{i\theta}\langle \hat{a}^\dagger \rangle)^2, \tag{5.88}$$

where the average number of photons $\langle \hat{a}^\dagger \hat{a} \rangle = \langle \hat{n} \rangle$ is given by Eq.(5.84). Inserting the system wavefunction, Eq.(5.60) yields for the averaged annihilation operator

$$\langle \hat{a} \rangle = \sum_{n=0}^{\infty} q_n^* q_{n+1} \left[\sqrt{n+1} \left(C_n^* C_{n+1} + D_n^* D_{n+1} \right) + \sqrt{n+2} \left(A_{n+1}^* A_{n+2} + B_{n+1}^* B_{n+2} \right) \right], \tag{5.89}$$

$$\langle \hat{a}^2 \rangle = \sum_{n=0}^{\infty} q_n^* q_{n+2} \left[\sqrt{n+2}\sqrt{n+1} \left(C_n^* C_{n+2} + D_n^* D_{n+2} \right) + \sqrt{n+3}\sqrt{n+2} \left(A_{n+1}^* A_{n+3} + B_{n+1}^* B_{n+3} \right) \right], \tag{5.90}$$

while the averaged creation operator is $\langle \hat{a}^{\dagger s} \rangle = \langle \hat{a}^s \rangle^*$, for integer s. The squeezing parameter Eq.(5.86) then follows from the above relations.

The calculated linear squeezing parameter as a function of scaled time $\tau = gt$ with $\theta = 0$ is plotted in Fig.(5.8) for different deformation functions and parameters. Squeezing is here evident for all deformation functions but at different parameter values and times. For all deformation functions and detuning parameter values, the squeezing in the presence of a Kerr medium becomes significant during a brief time interval $\Delta\tau = 0.1$ becomes significant, approaching -0.55 for both $f(n) = 1$ and $f(n) = 1/\sqrt{n}$ and -0.4 for $f(n) = \sqrt{n}$, c.f. Figs.(5.8b, 5.8d, 5.8f, 5.8h, 5.8j, 5.8l) . These values exceed those observed in many previously examined schemes such as the V, Λ, $\diamondsuit$-types [146, 147, 152], which possess maximum squeezing of ≈ -0.25 and is as well larger than the value (-0.03) reported for a N-type system in which the atom is initially a superposition of two

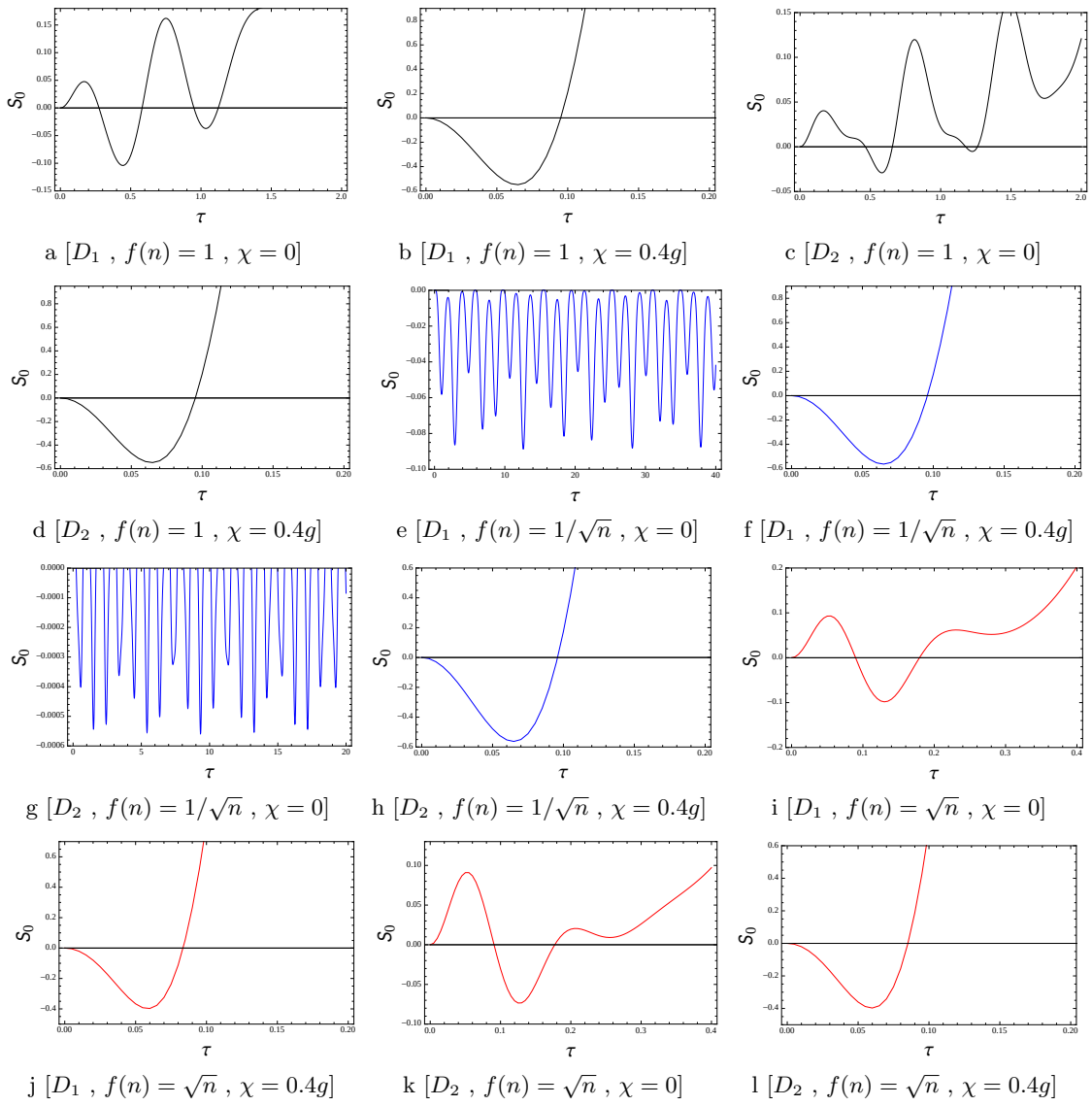

a $[D_1\ ,\ f(n)=1\ ,\ \chi=0]$ b $[D_1\ ,\ f(n)=1\ ,\ \chi=0.4g]$ c $[D_2\ ,\ f(n)=1\ ,\ \chi=0]$

d $[D_2\ ,\ f(n)=1\ ,\ \chi=0.4g]$ e $[D_1\ ,\ f(n)=1/\sqrt{n}\ ,\ \chi=0]$ f $[D_1\ ,\ f(n)=1/\sqrt{n}\ ,\ \chi=0.4g]$

g $[D_2\ ,\ f(n)=1/\sqrt{n}\ ,\ \chi=0]$ h $[D_2\ ,\ f(n)=1/\sqrt{n}\ ,\ \chi=0.4g]$ i $[D_1\ ,\ f(n)=\sqrt{n}\ ,\ \chi=0]$

j $[D_1\ ,\ f(n)=\sqrt{n}\ ,\ \chi=0.4g]$ k $[D_2\ ,\ f(n)=\sqrt{n}\ ,\ \chi=0]$ l $[D_2\ ,\ f(n)=\sqrt{n}\ ,\ \chi=0.4g]$

Figure 5.8: The squeezing parameter parameter dynamics for different detuning, Kerr coefficients and nonlinearity functions for $|\alpha|^2 = 10$ and $\theta = 0$.

atomic states [161]

For the deformation function $f(n) = 1/\sqrt{n}$ in the absence of a Kerr medium S_0 oscillates between positive and negative values while $-S_0$ is large when the field is detuned by D_1 as apparent from Figs.(5.8e, 5.8g). Thus the system oscillates between large and small values of the squeezing as a function of time, which could presumably be exploited experimentally. Further, the squeezing parameter appears to be insensitive to the detuning as for a given deformation function the squeezing is nearly identical whether D_1 or D_2 is employed. In the absence of the Kerr effect, squeezing occurs at different scaled times, namely $\tau \approx 0.5$ for $f(n) = 1$ in Figs.(5.8a, 5.8c) shows while $\tau \approx 0.13$ for $f(n) = \sqrt{n}$ in Figs.(5.8i, 5.8k). The squeezing parameters range from ≈ -0.1 to -0.05 in the two cases but are somewhat smaller in the presence of a Kerr medium. Note as well that while a $\diamondsuit$-type source does not exhibit squeezing for an intensity-dependent coupling function $f(n) = 1$ [152], the N-type system is highly squeezed for small τ. Thus in the N-type system squeezing can be realized for all the parameter values considered here. As well, the system can exhibit periodic squeezing over a long time interval or a larger squeezing amplitude over a short time. This should enable the system to be easily controlled and therefore employed as a nonclassical light source.

5.5 Conclusions

In this project, an N-type four level atom interacting with a single-mode field in the presence of a Kerr medium induced intensity-dependent coupling between the field and the atom was investigated for three deformation functions, namely a constant $f(n) = 1$ and two nonlinear functions $f(n) = 1/\sqrt{n}$ and $f(n) = \sqrt{n}$. The initial field was set to a coherent state while the atom was prepared in its most exited state. While only certain deformation functions and parameter values were examined, our analytic technique can be applied to any set of deformation functions and atomic parameters as well as initial states and atomic populations. From a practical perspective, the results indicate that the nonclassical properties of the field can be controlled by altering the detuning or the surrounding Kerr medium properties. The influence of the control parameter can presumably be further increased by careful optimzation of the system parameters.

To summarize the principal conclusions:

• Nonclassical anti-bunched, entangled and squeezed photons can be generated with an N-type 4-level system for both constant and non-constant deformation functions $f(n)$.

• The collapse and revival behaviour of the system can be controlled by modulating the properties of the Kerr medium. For a constant deformation function $f(n) = 1$, and a detuned field, collapse and revival effects persist at long times in the presence of a Kerr medium while this does not occur when the field is not detuned. Additionally for $f(n) = 1/\sqrt{n}$, the Kerr medium transforms the periodic behaviour of the system into collapse and revival.

• Collapse and revival effects can be enhanced or suppressed by controlling the detuning for $f(n) = \sqrt{n}$.

• The linear entropy (entanglement DEM) increases dramatically and stabilizes around a large amplitude in the presence of a nonlinear Kerr medium that is not detuned for all deformation functions. The Kerr nonlinearity can be employed to control or switch the entanglement for the deformation function $f(n) = 1/\sqrt{n}$.

• An N-type system yields a more nearly time-independent entanglement than a $\diamondsuit$-type in the presence of a Kerr medium

• The field statistics of an N-type system are primarily sub-Poissonian.

• Detuning normally leads to super-Poissonian statistics.

• Squeezing is observed for all deformation functions studied.

• In a Kerr medium yields the squeezing is typically larger at small times. Further the amplitude is larger than that predicted for Λ, V and $\diamondsuit$-type configurations.

• Larger values of squeezing result if only the most excited state rather than a superposition of different states is initially populated.

• For a deformation function $f(n) = 1/\sqrt{n}$ in the absence of a Kerr media, the squeezing is larger when the field is detuned. Further, both the field and the squeezing are periodic in time.

Chapter 6

Near Coherent state

In quantum mechanics, a particle can exist in a superposition of two states, a particular case of which is the well-known Schrödinger cat state (SCS). Such states are encountered frequently in modern physics, as in the superposition of two coherent states with maximum phase differences [170]. Such states have applications in, for example, quantum information and quantum computing [171, 172] and have been realized with both optical and electronic states [173, 174].

In this chapter, we study a superposition of two nearly identical coherent states that we term a near coherent state. We first briefly study the SCS of a single light mode, and then describe some possible extensions. Then, we will define the near coherent state and examine its different mathematical and nonclassical properties. After proposing a technique for generating these states we conclude by suggesting some potential applications.

6.1 Background

SCSs in a single light mode can be defined as

$$|\psi_S\rangle = C(|\alpha\rangle + e^{i\phi}|-\alpha\rangle), \tag{6.1}$$

in which ϕ is an arbitrary phase, $|\alpha\rangle$ is the coherent state defined in Eq.(5.26), and C is the normalization constant

$$C = \frac{1}{\sqrt{2 + 2e^{-2|\alpha|^2}\cos(\phi)}}. \tag{6.2}$$

The SCSs satisfy the following eigenequation

$$\hat{a}^2|\psi_S\rangle = \alpha^2|\psi_S\rangle, \tag{6.3}$$

where $|\psi_S\rangle$ here are the eigenfunctions and α^2 are the eigenvalues.

In general the two coherent states differ maximally in phase in order to confirm the interpretation of alive and dead states. However, three common implementations of SCS states which differ in their statistical properties exist. These are the even cats with $\phi = 0$, odd cats with $\phi = \pi$, and the Yurke-Stoler cats with $\phi = \pi/2$.

The superposition of two coherent states is not like a classical mixture. To see this, the density operator of the SCSs is given as

$$\hat{\rho}_S = |\psi_S\rangle\langle\psi_S| = C^2(|\alpha\rangle\langle\alpha| + |-\alpha\rangle\langle-\alpha| + e^{-i\phi}|-\alpha\rangle\langle\alpha| + e^{i\phi}|\alpha\rangle\langle-\alpha|), \tag{6.4}$$

while the density operator of a mixture of two opposite coherent states $|\pm\alpha\rangle$ equals

$$\hat{\rho}_{mix} = \frac{1}{2}(|\alpha\rangle\langle\alpha| + |-\alpha\rangle\langle-\alpha|). \tag{6.5}$$

From both expressions, we can see that there are two additional terms $|-\alpha\rangle\langle\alpha|$ and $|\alpha\rangle\langle-\alpha|$ which are not present in the classical expression. Therefore, the SCSs exhibit interference phenomena, and therefore cannot be represented classically. Furthermore, if we study the properties of the mixture of Eq.(6.5), we will not find any nonclassical behaviors.

The photon statistics distribution of the SCSs can be found by evaluating $|\langle n|\psi_S\rangle|^2$ which yields

$$P_n = \frac{|\alpha|^{2n}}{n!}\frac{1 + (-1)^n\cos(\phi)}{e^{|\alpha|^2} + e^{-|\alpha|^2}\cos(\phi)}. \tag{6.6}$$

If $\phi = \pi/2$ (Yurke-Stoler cats), then, P_n coincides with the Poisson distribution of the coherent state as in Eq.(5.29). while for $\phi = 0$ and $\phi = \pi$ which correspond to even and odd cats respectively, then $P_n = 0$ for all odd values of n when $\phi = 0$ and even values when $\phi = \pi$. Hence the even/odd cats always contain even/odd numbers of photons in a given measurement.

The linear squeezing properties of a quantum state can be determined by calculating or measuring the squeezing parameter as in Eq.(5.86) or the fluctuations of the quadrature operators Eq.(5.21).

In the case examined here, a quantum state is said to be squeezed if any of the variations of the quadrature operators has a value less than 1/4. The fluctuations of the quadrature operators of the SCSs are [175]

$$\langle(\Delta\hat{X})^2\rangle = \frac{1}{4} + \frac{|\alpha|^2}{1+e^{-2|\alpha|^2}\cos(\phi)}, \qquad \langle(\Delta\hat{Y})^2\rangle = \frac{1}{4} - |\alpha|^2 e^{-2|\alpha|^2}\left(\frac{e^{-2|\alpha|^2}+\cos(\phi)}{\left(1+e^{-2|\alpha|^2}\cos(\phi)\right)^2}\right), \quad (6.7)$$

where here for simplicity we assume that α is real. Therefore even cats ($\phi = 0$) can be squeezed as $\langle(\Delta\hat{Y})^2\rangle$ can be less than 1/4 while odd cats ($\phi = \pi$) cannot since the fluctuations of both $\hat{X}$ and $\hat{Y}$ always exceed 1/4. Finally, the Yurke-Stoler cats ($\phi = \pi/2$) are squeezed as the fluctuations of $\hat{Y}$ are always less than 1/4. Again the squeezing of the SCS is associated with the quantum nature of the state and cannot be reproduced classically.

Finally, the product of the fluctuations of both quadrature operators of the SCS is always greater than the minimum value of 1/16, and increases with the coherence parameter α. This behavior is the opposite of that of the coherent state, for which the product always equals the minimum value as Eq.(5.28) shows.

The quadrature space of the Fock state is given by

$$\psi_n(X) = \langle X|n\rangle = \frac{H_n(X)e^{-X^2/2}}{\sqrt{2^n n!\sqrt{\pi}}}, \quad (6.8)$$

where X represents the position space, and $H_n(X)$ is the Hermite polynomial, which fluctuates more as the number of photons (n) is increased. The quadrature space of a coherent state is

$$\psi_\alpha(X) = \langle X|\alpha\rangle = \frac{1}{\pi^{1/4}}\exp\left(-\frac{1}{2}X^2 - \frac{1}{2}\alpha^2 - \frac{1}{2}|\alpha|^2 + \sqrt{2}\alpha X\right), \quad (6.9)$$

which describes a Gaussian distribution centered at $\sqrt{2}\,\mathrm{Re}(\alpha)$. From these two equations, the quadrature space of the SCS is

$$\psi_S(X) = \langle X|\psi_S\rangle = \frac{C}{\pi^{1/4}}\exp\left(-\frac{1}{2}X^2 - \frac{1}{2}\alpha^2 - \frac{1}{2}|\alpha|^2\right)\left(e^{\sqrt{2}\alpha X} + e^{i\phi}e^{-\sqrt{2}\alpha X}\right), \quad (6.10)$$

where its probability distribution is plotted in Fig.(6.1). The two peaks in Fig.(6.1b) are centered at $\pm\sqrt{2}\mathrm{Re}(\alpha)$. The significance of the imaginary part of α decreases as the real part of α becomes larger. For small values of $\mathrm{Re}(\alpha)$, the fluctuations between the two peaks are very clear as is evident

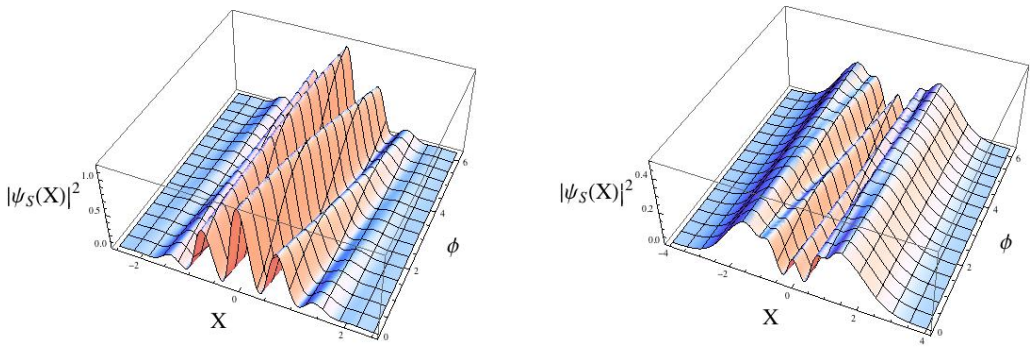

a $[\alpha = 3i]$. b $[\alpha = 1 + 3i]$.

Figure 6.1: The quadrature space probability function of the SCS as a function of X and ϕ.

in Fig.(6.1a), indicating the nonclassical signature of these states.

The Wigner distribution $W(\alpha)$ is a distribution over phase space that provides information on whether a state can be described classically or not. In particular, a state with a Wigner function that is negative at any point must be nonclassical, hence the function is often termed a quasi-probability distribution. The Wigner function is defined as

$$W(\alpha) = \frac{1}{\pi^2} \int d^2\gamma \mathrm{Tr}\left[\hat{\rho}\hat{D}(\gamma)\right] e^{-(\gamma\alpha^* - \gamma^*\alpha)}, \tag{6.11}$$

where $\hat{\rho}$ is the density operator of the state, and $\hat{D}(\gamma)$ is the displacement operator defined in Eq.(5.30) and the integration is taken over the entire physically accessible region.

The Wigner function for the even and odd SCSs is given by, with replacing α of Eq.(6.1) to $\alpha \to \beta$

$$W_{e,o}(\alpha) = \frac{e^{-2(\alpha_r - \beta)^2 - 2\alpha_i^2} + e^{-2(\alpha_r + \beta)^2 - 2\alpha_i^2} \pm 2\cos(4\alpha_i\beta)e^{-2\alpha_r^2 - 2\alpha_i^2}}{\pi(1 + e^{-2\beta^2})}, \tag{6.12}$$

where the + and - signs refers to the even and odd SCSs respectively while α_r, α_i are the real and imaginary parts of the coherent coefficient α. Since this Wigner function is always negative within some region near the origin, the SCS is nonclassical. The Wigner function of an even cat is depicted in Fig.(6.2). The peaks correspond to the two coherent states $|\pm\beta\rangle$ while quantum interference yields oscillations between the peaks which are negative in some regions. While SCS possess many additional properties, one that should be mentioned is that the even cats are always bunched while the odd cats are always anti-bunched [176].

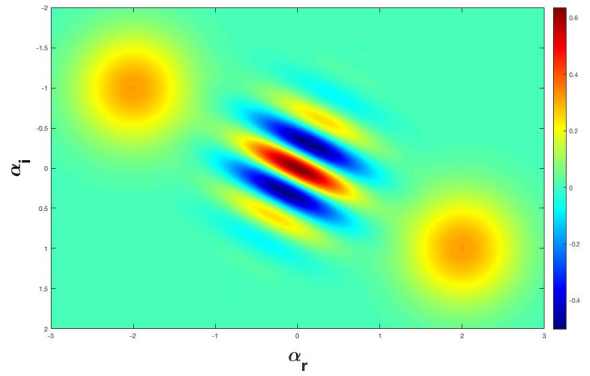

Figure 6.2: The Wigner function $W(\alpha)$ of the even cat state for $\beta = 2 + i$. The oscillations between the two peaks result from quantum interference.

6.1.1 Extensions

While SCSs have been extended by many authors, one state of particular interest results from superposing two coherent states with α parameter but with opposite phases [177], e.g.

$$|\psi\rangle = N(|\alpha e^{i\phi/2}\rangle + |\alpha e^{-i\phi/2}\rangle). \tag{6.13}$$

Another state was constructed with two different values of the coherent parameter but with a fixed phase for each [178], while the superposition of two identical magnitude coherent states that are $\pi/2$, π or $3\pi/2$ out of phase was considered in [179–182]. In each case, nonclassical properties such as squeezing, anti-bunching, Wigner function were examined. All these studies are however special cases of the most general expression for the superposition of two arbitrary coherent states introduced by Hari Prakash and Pankaj Kumarb in 2003 [183, 184], namely

$$|\psi\rangle = Z_1|\alpha\rangle + Z_2|\beta\rangle, \tag{6.14}$$

where Z_1, Z_2, α and β can take any complex value. The normalization condition requires that

$$\langle\psi|\psi\rangle = |Z_1|^2 + |Z_2|^2 + 2\mathrm{Re}\left[Z_1^* Z_2 e^{-\frac{1}{2}(|\alpha|^2+|\beta|^2)+\alpha^*\beta}\right] = 1. \tag{6.15}$$

They examined the linear squeezing of this state and found that the minimum possible value of the uncertainties of the quadrature operators leading to maximum squeezing is 0.11077. This value

occurs for an infinite number of parameter sets that satisfy $\alpha - \beta = i1.59912$ and $Z_1/Z_2 = e^{\alpha^*\beta - \alpha\beta^*}$ [185]. These and many other studies confirm that the superposition of two coherent states is clearly nonclassical. The experimental realization of such states is presented in [170–172, 186–189] and numerous applications have been proposed. Additionally, superpositions of states other than the coherent state have also been studied [190–192]).

Despite the many previous extensions and generalizations of SCSs, one superposition has not been examined to the best of our knowledge, namely the superposition of two almost identical coherent states

$$|\alpha, \Delta\theta\rangle = \lim_{|\Delta\alpha|\to 0} C_\alpha(|\alpha + \Delta\alpha\rangle - |\alpha\rangle). \tag{6.16}$$

where C_α is a normalization constant, $\Delta\alpha = |\Delta\alpha|e^{i\Delta\theta}$ is here termed the source of the state and $\Delta\theta$ is the phase of the source. While such a state would appear to vanish, the presence of the large normalization constant insures that this state approaches the quantum mechanical analogue of the derivative of a coherent state that we term here the near coherent state.

On the other hand, it is not immediately apparent from the definition of Eq.(6.16) if the near coherent state exhibits nonclassical properties. In fact, however, the analysis of this chapter demonstrates that the near state exhibits marked nonclassical properties that differ from those of the SCSs and presumably from other similar quantum states. Below we investigate the quantum properties of such a superposition.

6.2 The near coherent states

We can define the near coherent state by

$$|\alpha, \Delta\theta\rangle = \lim_{|\Delta\alpha|\to 0} C_\alpha(|\alpha+\Delta\alpha\rangle - |\alpha\rangle) = \lim_{|\Delta\alpha|\to 0} C_\alpha(|\tilde{\alpha}\rangle - |\tilde{\alpha}-\Delta\alpha\rangle) = \lim_{|\Delta\alpha\to 0} C_\alpha(|\bar{\alpha}+\Delta\alpha/2\rangle - |\bar{\alpha}-\Delta\alpha/2\rangle), \tag{6.17}$$

where $\tilde{\alpha} = \alpha + \Delta\alpha$ and $\bar{\alpha} = \alpha + \Delta\alpha/2$. These formulas are equivalent even if $\tilde{\alpha}$ and $\bar{\alpha}$ are not functions of $\Delta\alpha$. Note that in the limit

$$|\psi\rangle = \lim_{\phi\to 0} N(|\alpha\rangle - |\alpha e^{i\phi}). \tag{6.18}$$

for which the source phase $\Delta\theta$ equals $\theta - \pi/2$, since for small ϕ, $\alpha e^{i\phi} \approx \alpha - |\alpha|\phi e^{i(\theta-\pi/2)}$ we recover the second expression of Eq.(6.17) with $\Delta\theta = \theta - \pi/2$, where θ is the phase of $\alpha = |\alpha|e^{i\theta}$.

The normalization constant C_α is obtained from $\langle \alpha, \Delta\theta | \alpha, \Delta\theta \rangle = 1$ and therefore

$$C_\alpha = \frac{1}{\sqrt{2 - \langle \alpha + \Delta\alpha | \alpha \rangle - \langle \alpha | \alpha + \Delta\alpha \rangle}}. \tag{6.19}$$

Accordingly, the inner product of two general coherent states $|\alpha\rangle$ and $|\beta\rangle$ is given by

$$\langle \beta | \alpha \rangle + c.c. = e^{-\frac{1}{2}|\alpha|^2 - \frac{1}{2}|\beta|^2} \left(e^{\beta^* \alpha} + e^{\beta \alpha^*} \right). \tag{6.20}$$

Using this relation, we find the inner product of $\langle \alpha + \Delta\alpha | \alpha \rangle$ and its complex conjugate as

$$\langle \alpha + \Delta\alpha | \alpha \rangle + c.c. = 2e^{-\frac{|\Delta\alpha|^2}{2}} \cos(|\Delta\alpha||\alpha| \sin(\Delta\theta - \theta)). \tag{6.21}$$

This expression can be expanded around $|\Delta\alpha| \approx 0$ to give

$$\langle \alpha + \Delta\alpha | \alpha \rangle + c.c. \approx 2 - \left[1 + |\alpha|^2 \sin(\Delta\theta - \theta)^2 \right] |\Delta\alpha|^2 + \cdots. \tag{6.22}$$

Then, C_α is given as

$$C_\alpha = \frac{1}{|\Delta\alpha| \sqrt{1 + |\alpha|^2 \sin(\Delta\theta - \theta)^2}}. \tag{6.23}$$

which diverges in the $|\Delta\alpha| \to 0$ limit. Accordingly, the state $|\alpha + \Delta\alpha\rangle - |\alpha\rangle$ must first be determined after which the limit is taken. Accordingly, the near coherent state can be expressed as

$$|\alpha, \Delta\theta\rangle = \frac{1}{\sqrt{1 + |\alpha|^2 \sin(\Delta\theta - \theta)^2}} \lim_{|\Delta\alpha| \to 0} \frac{|\alpha + \Delta\alpha\rangle - |\alpha\rangle}{|\Delta\alpha|}. \tag{6.24}$$

Substituting $|\alpha\rangle$ from Eq.(5.26) into Eq.(6.24) yields

$$|\alpha, \Delta\theta\rangle = \frac{1}{\sqrt{1 + |\alpha|^2 \sin(\Delta\theta - \theta)^2}} \lim_{|\Delta\alpha| \to 0} \sum_{n=0}^{\infty} \frac{1}{\sqrt{n!}|\Delta\alpha|} \left[e^{-\frac{1}{2}|\alpha + \Delta\alpha|^2} (\alpha + \Delta\alpha)^n - e^{-\frac{1}{2}|\alpha|^2} \alpha^n \right] |n\rangle. \tag{6.25}$$

The expression inside the bracket inside the summation can be further written as

$$e^{-\frac{1}{2}|\alpha|^2} \left[e^{-\frac{1}{2}|\Delta\alpha|^2 - |\alpha||\Delta\alpha| \cos(\Delta\theta - \theta)} \left(|\alpha| e^{i\theta} + |\Delta\alpha| e^{i\Delta\theta} \right)^n - |\alpha|^n e^{in\theta} \right]. \tag{6.26}$$

Expanding the above expression around $|\Delta\alpha| \approx 0$ then gives

$$e^{-\frac{1}{2}|\alpha|^2}\alpha^n \left[\frac{e^{i(\Delta\theta-\theta)}n}{|\alpha|} - |\alpha|\cos(\Delta\theta-\theta)\right]|\Delta\alpha| + \cdots . \tag{6.27}$$

Substituting this expression back into Eq.(6.25), the source amplitude $|\Delta\alpha|$ cancels between the denominator and numerator resulting in

$$|\alpha, \Delta\theta\rangle = e^{-\frac{1}{2}|\alpha|^2}\sum_{n=0}^{\infty}\frac{\alpha^n\left[\frac{e^{i(\Delta\theta-\theta)}n}{|\alpha|} - |\alpha|\cos(\Delta\theta-\theta)\right]}{\sqrt{n!}\sqrt{1+|\alpha|^2\sin(\Delta\theta-\theta)^2}}|n\rangle. \tag{6.28}$$

This expression can be further simplified as follows

$$\frac{\partial|\alpha\rangle}{\partial|\alpha|} = e^{-\frac{1}{2}|\alpha|^2}\sum_{n=0}^{\infty}\frac{\alpha^n}{\sqrt{n!}}\left[\frac{n}{|\alpha|} - |\alpha|\right]|n\rangle = \frac{e^{-\frac{1}{2}|\alpha|^2}}{|\alpha|}\sum_{n=0}^{\infty}\frac{n\alpha^n}{\sqrt{n!}}|n\rangle - |\alpha||\alpha\rangle, \tag{6.29}$$

or equivalently

$$e^{-\frac{1}{2}|\alpha|^2}\sum_{n=0}^{\infty}\frac{n\alpha^n}{\sqrt{n!}}|n\rangle = |\alpha|\frac{\partial|\alpha\rangle}{\partial|\alpha|} + |\alpha|^2|\alpha\rangle, \tag{6.30}$$

where $\frac{\partial\alpha\rangle}{\partial|\alpha|}$ is referred to as the derivative state. The near coherent state can finally be written as

$$|\alpha, \Delta\theta\rangle = \frac{e^{i\delta\theta}\frac{\partial|\alpha\rangle}{\partial|\alpha|} + i|\alpha|\sin(\delta\theta)|\alpha\rangle}{\sqrt{1+|\alpha|^2\sin(\delta\theta)^2}}, \tag{6.31}$$

where $\delta\theta = \Delta\theta - \theta$ is the phase difference. This constitutes the complete expression for the near coherent state. Evidently the near coherent state exists and takes the form of a superposition of a coherent state and a derivative state. Also, the form of the near coherent state depends on the phase differences $\delta\theta$ which in the $\delta\theta = 0$ limit, where the the source and α possess the same phase, simplifies to $|\alpha, \Delta\theta\rangle = \frac{\partial|\alpha\rangle}{\partial|\alpha|}$. When instead $\delta\theta = \pm\pi/2$, the state becomes $|\alpha, \Delta\theta\rangle = \pm i(\frac{\partial|\alpha|\rangle}{\partial|\alpha} + |\alpha||\alpha\rangle)/\sqrt{1+|\alpha|^2}$. Lastly if $\alpha = 0$, the near coherent state becomes $|1\rangle$. Before we examining the properties of near coherent states, in the next section we provide a general formulation for constructing a near state starting with any state.

6.3 Generalizations of the near coherent state

Consider a single mode state $|r\rangle$ parametrized by a complex parameter r such as for example a qubit state $|r\rangle = (r|0\rangle + |1\rangle)/\sqrt{|r|^2+1}$. The near state corresponding to $|r\rangle$ is defined as

$$|r, \Delta\theta\rangle = \lim_{|\Delta r|\to 0} C_r(|r+\Delta r\rangle - |r\rangle) = \lim_{|\Delta r|\to 0} C_r(|r+|\Delta r|e^{i\Delta\theta}\rangle - |r\rangle). \tag{6.32}$$

with the normalization constant C_r

$$C_r = \frac{1}{\sqrt{2-\langle r+\Delta r|r\rangle - \langle r|r+\Delta r\rangle}}. \tag{6.33}$$

Expanding the inner product $\langle r|r+\Delta r\rangle$ around $|\Delta r| \approx 0$, gives

$$\langle r|r+\Delta r\rangle \approx 1 + g_1(r)\,|\Delta r| - \frac{g_2(r)}{2}|\Delta r|^2 + \cdots, \tag{6.34}$$

where $g_1(r)$ and $g_2(r)$ are expansion functions. Combining this expression with its conjugate

$$\langle r+\Delta r|r\rangle + c.c. \approx 2 + 2\,\mathrm{Re}(g_1(r))|\Delta r| - \mathrm{Re}(g_2(r))|\Delta r|^2 + \cdots \tag{6.35}$$

Substituting Eq.(6.35) into the normalization constant C_r then yields

$$C_r = \lim_{|\Delta r|\to 0} \frac{1}{\sqrt{-2\,\mathrm{Re}(g_1(r))|\Delta r| + \mathrm{Re}(g_2(r))|\Delta r|^2}}. \tag{6.36}$$

Since the expansion of $|r+\Delta r\rangle - |r\rangle$ in Eq.(6.32) around $|\Delta r| \approx 0$ is of the order of $|\Delta r|$, the expression of $\mathrm{Re}(g_1(r))$ in Eq.(6.36) must be zero to obtain a finite near state. Therefore, if expanding Eq.(6.35) for a given state yields a nonzero value of $\mathrm{Re}(g_1(r))$, this state cannot construct a near state. Thus $\mathrm{Re}(g_1(r)) = 0$ is the necessary condition for constructing a nonvanishing near state. Assuming that $|r\rangle$ satisfies this condition, the normalization constant C_r then becomes

$$C_r = \sqrt{\frac{1}{\mathrm{Re}(g_2(r))}}\;\frac{1}{|\Delta r|}. \tag{6.37}$$

Substituting this expression back into the near state $|r, \Delta\theta\rangle$ yields

$$|r, \Delta\theta\rangle = \sqrt{\frac{1}{\mathrm{Re}(g_2(r))}} \lim_{|\Delta r|\to 0} \frac{|r+\Delta r\rangle - |r\rangle}{|\Delta r|}. \tag{6.38}$$

After expanding the state $|r+\Delta r\rangle$ around $|\Delta r| \approx 0$ we have

$$|r+\Delta r\rangle \approx |r\rangle + \left(\frac{\partial |r+\Delta r\rangle}{\partial |\Delta r|}\right)\Big|_{|\Delta r|=0} |\Delta r| + \cdots . \tag{6.39}$$

which leads to, after combining with the near state expression Eq.(6.38)

$$|r, \Delta\theta\rangle = \sqrt{\frac{1}{\mathrm{Re}(g_2(r))}} \left(\frac{\partial |r+\Delta r\rangle}{\partial |\Delta r|}\right)\Big|_{|\Delta r|=0}. \tag{6.40}$$

This final expression describes a near state dependent on a single parameter. Note that Eq.(6.40) requires two inputs, the state $|r+\Delta r\rangle$ and $g_2(r)$ which originated in the expansion of the inner product $\langle r|r+\Delta r\rangle$. If we assume that both r and Δr are real, Eq.(6.40) or Eq.(6.38) simplify to

$$|r, \Delta\theta\rangle = \sqrt{\frac{1}{\mathrm{Re}(g_2(r))}} \left(\frac{d|r\rangle}{dr}\right), \tag{6.41}$$

which corresponds to a derivative state with respect to the real parameter r.

We next examine the question of whether the existence of near states is a purely quantum mechanical phenomena or whether it also exists classically. Clearly if two classical waves are superimposed according to

$$S_1 = \lim_{|\Delta y|\to 0} [H(y + |\Delta y| e^{i\Delta\theta}) - H(y)], \tag{6.42}$$

where $H(y)$ is any vector field dependent on a variable y which could be, for example, the amplitude, frequency, wave vector of the wave, the result is zero, $S_1 = 0$.

On the other hand combining two classical distributions according to

$$S_2 = \lim_{\Delta s\to 0} C_s[P(s + \Delta s e^{i\Delta\theta}) - P(s)], \tag{6.43}$$

where $P(s)$ is any non-normalized distribution function, and s, Δs both are real parameters [1] which

[1] Note that $e^{i\Delta\theta}$ is complex, but, in general, it can be replaced to any function $e^{i\Delta\theta} \to f(\Delta\theta)$, and the final result will be the same.

characterizes the distribution. For example, $P(s)$ could be a Gaussian distribution, $P(s) = e^{-x^2/2s^2}$, and s could be the mean or the standard deviation. x is the real variable of the distribution. C_s is the normalization constant, which after imposing the normalization condition $\int S_2 dx = 1$, can be written as

$$C_s = \frac{1}{\int [P(s + \Delta s e^{i\Delta\theta}) - P(s)] dx}. \tag{6.44}$$

Expanding $P(s + \Delta s e^{i\Delta\theta})$ around $\Delta s \approx 0$, yields

$$P(s + \Delta s e^{i\Delta\theta}) \approx P(s) + e^{i\Delta\theta} \frac{\partial P(s)}{\partial s} \Delta s + \frac{1}{2} e^{2i\Delta\theta} \frac{\partial^2 P(s)}{\partial s^2} \Delta s^2 + \cdots . \tag{6.45}$$

Then, the superposition of Eq.(6.43) becomes

$$S_2 = \lim_{\Delta s \to 0} \frac{e^{i\Delta\theta} \frac{\partial P(s)}{\partial s} \Delta s + \frac{1}{2} e^{2i\Delta\theta} \frac{\partial^2 P(s)}{\partial s^2} \Delta s^2}{\int \left[e^{i\Delta\theta} \frac{\partial P(s)}{\partial s} \Delta s + \frac{1}{2} e^{2i\Delta\theta} \frac{\partial^2 P(s)}{\partial s^2} \Delta s^2 \right] dx}. \tag{6.46}$$

Then, if $\frac{\partial P(s)}{\partial s}$ exists, S_2 becomes

$$S_2 = \frac{\frac{\partial P(s)}{\partial s}}{\int \frac{\partial P(s)}{\partial s} dx}. \tag{6.47}$$

Hence the near distribution of Eq.(6.43) exists, and is finite. However the source phase is no longer present in S_2, so that the resultant distribution is not a function of $\Delta\theta$. On the other hand, in Eq.(6.35) or Eq.(6.22) the source's phase did not factor out as in Eq.(6.45). This is accordingly suggest that this is a pure quantum mechanical effect.

Hence applying the definition of near states to classical waves yields zero, but when it applied to classical distributions they exist but do not depend on the source phase, unlike quantum near states.

6.4 Identities and mathematical properties

In this section, we derive several mathematical properties of the near coherent state. First, to construct the generator of a state $\hat{A_\alpha}$. Observe that if a photon is added to a coherent state by applying the operator $\hat{a}^\dagger$, the resulting state is [193]

$$\hat{a}^\dagger |\alpha\rangle = \left(\frac{\partial}{\partial \alpha} + \frac{\alpha^*}{2} \right) |\alpha\rangle = \frac{e^{-\frac{1}{2}|\alpha|^2}}{\alpha} \sum_{n=0}^{\infty} \frac{\alpha^n n}{\sqrt{n!}} |n\rangle. \tag{6.48}$$

where the derivative is taken with respect to α rather than $|\alpha|$ as in the near coherent state. The relationship between the two derivatives is

$$\frac{\partial|\alpha\rangle}{\partial\alpha} = \frac{|\alpha|}{\alpha}\frac{\partial|\alpha\rangle}{\partial|\alpha|} + \frac{|\alpha|^2}{2\alpha}|\alpha\rangle. \tag{6.49}$$

By applying Eq.(6.30), the derivative in Eq.(6.29) simplifies to

$$\frac{\partial|\alpha\rangle}{\partial|\alpha|} = \left(\frac{\alpha}{|\alpha|}\hat{a}^\dagger - |\alpha|\right)|\alpha\rangle = \left(\frac{\alpha}{|\alpha|}\hat{a}^\dagger - \frac{|\alpha|}{\alpha}\hat{a}\right)|\alpha\rangle \tag{6.50}$$

from which Eq.(6.31) can be rewritten as

$$|\alpha, \Delta\theta\rangle = \left[\frac{e^{i\delta\theta}\frac{\alpha}{|\alpha|}\hat{a}^\dagger - [1 - i\sin(\delta\theta)]\frac{|\alpha|}{\alpha}\hat{a}}{\sqrt{1 + |\alpha|^2\sin(\delta\theta)^2}}\right]|\alpha\rangle = \hat{A_\alpha}|\alpha\rangle. \tag{6.51}$$

where the expression inside the bracket is the generator operator $\hat{A_\alpha}$. When $\delta\theta = 0$, this operator becomes

$$\hat{A_\alpha} = \left(e^{i\theta}\hat{a}^\dagger - e^{-i\theta}\hat{a}\right), \tag{6.52}$$

where again θ is the complex phase of α. This operator is skew-Hermitian and commutes with its Hermitian conjugate. The operator $\hat{A_\alpha}$ is nonunitary, implying that the near coherent state cannot be generated from the vacuum state. The commutation relation of $\hat{A_\alpha}$ is then

$$[\hat{A_\alpha}, \hat{A_\alpha}^\dagger] = \frac{\sin(\delta\theta)^2}{1 + |\alpha|^2\sin(\delta\theta)^2}[\hat{a}, \hat{a}^\dagger]. \tag{6.53}$$

The near state can however be related to other known states as for example the Agarwal state or the photon-added coherent state [194] by applying the annihilation operator according to

$$a^\dagger|\alpha\rangle = \sqrt{1 + |\alpha|^2}\,|\alpha, 1\rangle, \tag{6.54}$$

where $|\alpha, 1\rangle$ is the Agarwal state.

Acting with the annihilation operator on the derivative of Eq.(6.50) now gives

$$\hat{a}\left(\frac{\partial|\alpha\rangle}{\partial|\alpha|}\right) = \alpha\frac{\partial|\alpha\rangle}{\partial|\alpha|} + \frac{\alpha}{|\alpha|}|\alpha\rangle. \tag{6.55}$$

while applying the annihilation operator to $|\alpha, \Delta\theta\rangle$ yields

$$\hat{a}|\alpha, \Delta\theta\rangle = \alpha|\alpha, \Delta\theta\rangle + \frac{e^{i\delta\theta}\alpha}{|\alpha|\sqrt{1+|\alpha|^2\sin(\delta\theta)^2}}|\alpha\rangle, \tag{6.56}$$

which yields the initial state plus the coherent state. Note that if $\delta\theta$ equals zero, this identity simplifies to

$$\hat{a}|\alpha, \Delta\theta\rangle = \alpha|\alpha, \Delta\theta\rangle + \frac{\alpha}{|\alpha|}|\alpha\rangle. \tag{6.57}$$

Also, we can derive

$$\hat{a}^2|\alpha, \Delta\theta\rangle = \alpha^2|\alpha, \Delta\theta\rangle + \frac{2e^{i\delta\theta}\alpha^2}{|\alpha|\sqrt{1+|\alpha|^2\sin(\delta\theta)^2}}|\alpha\rangle. \tag{6.58}$$

Next we can find the eigenequation of the near coherent state from Eq.(6.56) and Eq.(6.58) namely

$$\hat{\mathcal{A}}_\alpha|\alpha, \Delta\theta\rangle \equiv \left(2\hat{a} - \frac{\hat{a}^2}{\alpha}\right)|\alpha, \Delta\theta\rangle = \alpha|\alpha, \Delta\theta\rangle, \tag{6.59}$$

where $\hat{\mathcal{A}}_\alpha$ is $\left(2\hat{a} - \frac{\hat{a}^2}{\alpha}\right)$. The near coherent state is not the only possible eigenfunction of this operator, the coherent state $|\alpha\rangle$ itself is a possible solution as well. The operator $\hat{\mathcal{A}}_\alpha$ is, in fact, a special case of the C.Brif operator [195].

To calculate inner products Eqs.(6.20, 6.48, 6.50) can be applied to the coherent state with the derivative state $\langle\alpha|\left(\frac{\partial|\beta\rangle}{\partial|\beta|}\right)$ to yield

$$\langle\alpha|\left(\frac{\partial|\beta\rangle}{\partial|\beta|}\right) = e^{-\frac{1}{2}|\alpha|^2 - \frac{1}{2}|\beta|^2 + \beta\alpha^*}\left[\frac{\beta\alpha^*}{|\beta|} - |\beta|\right]. \tag{6.60}$$

Note that if the derivative is taken with respect to α instead of β, this inner product becomes zero, implying $\langle\alpha|(\partial|\alpha\rangle/\partial|\alpha|) = 0$. From Eq.(6.60) and Eq.(6.31), the inner product of the near coherent state is then

$$\langle\alpha|\beta, \Delta\theta\rangle = \frac{e^{-\frac{1}{2}|\alpha|^2 - \frac{1}{2}|\beta|^2 + \beta\alpha^*}}{\sqrt{1+|\beta|^2\sin(\delta\theta)^2}}\left[e^{i\delta\theta}\left(\frac{\beta\alpha^*}{|\beta|} - |\beta|\right) + i|\beta|\sin(\delta\theta)\right]. \tag{6.61}$$

If both states are instead with respect to α,

$$\langle\alpha|\alpha, \Delta\theta\rangle = \frac{i|\alpha|\sin(\delta\theta)}{\sqrt{1+|\alpha|^2\sin(\delta\theta)^2}}. \tag{6.62}$$

The inner product of two derivative states is found to be

$$\left(\frac{\partial\langle\alpha|}{\partial|\alpha|}\right)\left(\frac{\partial|\beta\rangle}{\partial|\beta|}\right) = e^{-\frac{1}{2}|\alpha|^2-\frac{1}{2}|\beta|^2+\beta\alpha^*}\left[\frac{\alpha^*\beta}{|\alpha||\beta|}+\frac{\alpha^{*2}\beta^2}{|\alpha||\beta|}-\frac{|\beta|\alpha^*\beta}{|\alpha|}-\frac{|\alpha|\alpha^*\beta}{|\beta|}+|\alpha||\beta|\right]. \tag{6.63}$$

which can also be employed to calculate the inner product of near coherent states. Observe that this yields unity when $\beta = \alpha$, indicating that the derivative state is normalized.

6.5 Propagation and quadrature properties

While during propagation the coherent state does not change its form or amplitude, its phase varies with time as

$$e^{iHt/\hbar}|\alpha\rangle = e^{-i\omega t/2}|\alpha e^{-i\omega t}\rangle, \tag{6.64}$$

where H is the Hamiltonian for free propagation of a single mode $H = \hbar\omega(\hat{a}^\dagger\hat{a}+1/2)$. Applying the evolution operator to the derivative state Eq.(6.29) yields

$$e^{iHt/\hbar}\frac{\partial|\alpha\rangle}{\partial|\alpha|} = e^{-i\omega t/2}\frac{\partial|\alpha e^{-i\omega t}\rangle}{\partial|\alpha|}. \tag{6.65}$$

When the above equations are subsequently applied to the near coherent state we obtain

$$e^{iHt/\hbar}|\alpha,\Delta\theta\rangle = e^{-i\omega t/2}|\alpha e^{-i\omega t},\Delta\theta\rangle. \tag{6.66}$$

Hence free propagation does not alter the amplitude of the near coherent state. Although the phase of α is altered the source phase $\Delta\theta$ and the phase differences $\delta\theta$ remain invariant. Therefore, a coherent state prepared with a given value of $\delta\theta$ is not affected by free propagation.

The quadrature space of the near coherent state can now be evaluated with Eqs.(6.8,6.9) which leads to

$$\psi_d(X) = \left(\frac{\sqrt{2}\alpha X-\alpha^2}{|\alpha|}-|\alpha|\right)\psi_\alpha(X), \tag{6.67}$$

where $\psi_\alpha(X)$ is the coherent quadrature function of Eq.(6.9). Applying the near coherent state expression, Eq.(6.31), yields for the quadrature space

$$\psi_{NC}(X) = \left[\frac{|\alpha|^{-1}e^{i\delta\theta}(\sqrt{2}\alpha X-\alpha^2)+|\alpha|\left(i\sin(\delta\theta)-e^{i\delta\theta}\right)}{\sqrt{1+|\alpha|^2\sin(\delta\theta)^2}}\right]\psi_\alpha(X), \tag{6.68}$$

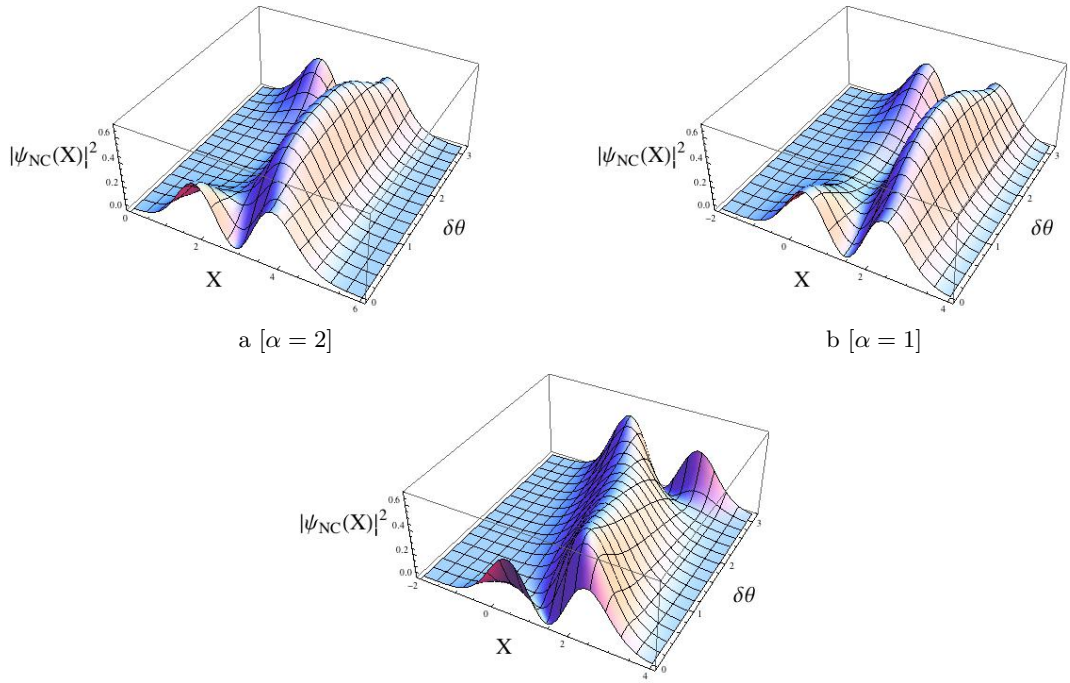

a $[\alpha = 2]$ b $[\alpha = 1]$

c $[\alpha = 1 + 3i]$

Figure 6.3: The quadrature distribution of the near coherent state for different values of α.

which is proportional to the coherent quadrature function $\psi_\alpha(X)$. This implies that the value of α does not affect, in general, the form of $|\psi_{NC}(X)|^2$, which is similar to the behavior of coherent states but contrasts with that of general SCSs. The quadrature distribution of the near coherent state for different values of α is displayed in Fig.(6.3). The shape but not the location of the distribution depends significantly on the imaginary component of α while the real component does not significantly change the shape but does lead to an overall displacement. When $\delta\theta$ equals 0 and π two peaks located at $\sqrt{2}\,\mathrm{Re}(\alpha) \pm 1$ are evident in the distribution where the zero point is located at $\sqrt{2}\,\mathrm{Re}(\alpha)$. These two peaks arise from the quantum interference resulting from the superposition of the two near coherent states.

6.6 Statistical properties

Examining next the statistical properties of the near coherent state, the photon probability distribution, is obtained by multiplying Eq.(6.28) with $\langle n|$ and squaring, which yields

$$P_n = |\langle n|\alpha, \Delta\theta\rangle|^2 = \frac{e^{-|\alpha|^2}|\alpha|^{2n}\left[\frac{n^2}{|\alpha|^2} + \cos(\delta\theta)^2(|\alpha|^2 - 2n)\right]}{n!\,(1 + |\alpha|^2\sin(\delta\theta)^2)}. \tag{6.69}$$

Thus even when $\alpha = 0$ one photon is still present. The photon distribution is illustrated in Fig.(6.4). When $\delta\theta = 0$, the probability equals zero at $n = |\alpha|^2$, indicating the presence of a strong quantum interference. Also, at the same angle, $\delta\theta = 0$ as $|\alpha|$ becomes larger the two peaks of Fig.(6.4) become identical. Similarly when $\delta\theta$ equals $\pi/2$, only one peak is present that is is similar in shape to the Poisson distribution of the coherent state.

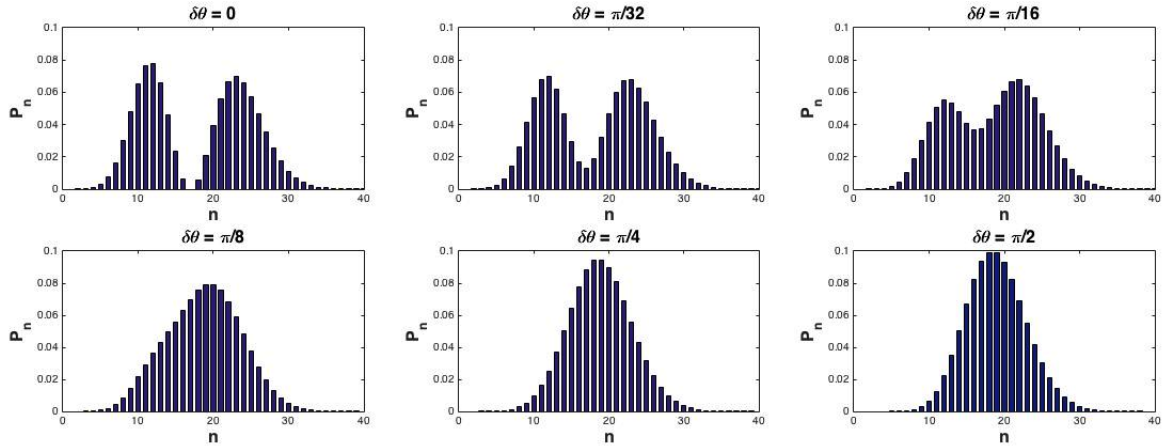

Figure 6.4: The photon probability distribution of the near coherent state for different values of the phase differences $\delta\theta$ for $|\alpha| = 4$.

The average number of photons of the near coherent state, $\langle\hat{n}\rangle$, is evaluated from Eq.(6.56),

$$\langle\hat{n}\rangle = |\alpha|^2 + \frac{1 + 2|\alpha|^2\sin(\delta\theta)^2}{1 + |\alpha|^2\sin(\delta\theta)^2} = |\alpha|^2 + M, \tag{6.70}$$

where M is defined as

$$M = \frac{1 + 2|\alpha|^2\sin(\delta\theta)^2}{1 + |\alpha|^2\sin(\delta\theta)^2}. \tag{6.71}$$

The maximum value of Eq.(6.70) attains a maximum equal to $2 + |\alpha|^2$ when $\delta\theta$ equals $\pi/2$ and $|\alpha|^2 \gg 1$, and a minimum of $|\alpha|^2 + 1$, at $\delta\theta = 0$. Further, after applying the identity Eq.(6.58), we

obtain for the square number operator

$$\langle \hat{n}^2 \rangle = \langle \hat{a}^\dagger \hat{a} \hat{a}^\dagger \hat{a} \rangle = |\alpha|^4 + 5|\alpha|^2 + \frac{1 + 2|\alpha|^2 \sin(\delta\theta)^2}{1 + |\alpha|^2 \sin(\delta\theta)^2} = |\alpha|^4 + 5|\alpha|^2 + M. \tag{6.72}$$

So the photon number fluctuation

$$\langle \Delta\hat{n} \rangle = \sqrt{\langle \hat{n}^2 \rangle - \langle \hat{n} \rangle^2} = \sqrt{|\alpha|^2(5 - 2M) + M(1 - M)} = \sqrt{\langle \hat{n} \rangle (5 - 2M) + M(M - 4)}, \tag{6.73}$$

which reaches a maximum equal to $\sqrt{3}\,|\alpha|$ for a phase difference $\delta\theta = 0$, and a minimum value at $\delta\theta = \pi/2$.

Next, we calculate the quantum phase distribution $\mathcal{P}(\varphi)$ of the near coherent state in the Pegg-Barnett formulation [196, 197], namely

$$\mathcal{P}(\varphi) = \frac{1}{2\pi} |\langle \varphi | r \rangle|^2, \tag{6.74}$$

where the state $|\varphi\rangle$ is defined as

$$|\varphi\rangle = \sum_{n=0}^{\infty} e^{in\varphi} |n\rangle. \tag{6.75}$$

Employing Eq.(6.28) then yields

$$\mathcal{P}(\varphi) = \frac{1}{2\pi} |\langle \varphi | \alpha, \Delta\theta \rangle|^2 = \frac{e^{-|\alpha|^2}}{2\pi[1 + |\alpha|^2 \sin(\delta\theta)^2]} \left| \sum_{n=0}^{\infty} \frac{e^{-i(n\varphi - \theta)} |\alpha|^n}{\sqrt{n!}} \left(\frac{n e^{i\delta\theta}}{|\alpha|} - |\alpha| \cos(\delta\theta) \right) \right|^2 \tag{6.76}$$

which approaches the single peaked phase distribution of the coherent state as $\delta\theta \to \pi/2$. In contrast, when $\delta\theta \to 0$, the distribution exhibits two peaks.

6.7 Nonclassical properties

6.7.1 Squeezing properties

The nonclasicality of the near state also manifests itself in squeezing. To evaluate the expectation values of the quadrature operators of Eq.(5.21) for the near coherent state certain mathematical

relations derived from Eqs.(6.56,6.58,6.62) are useful, namely

$$\langle \hat{a} \rangle = \alpha \left(1 - iK^2 \sin(\delta\theta) e^{i\delta\theta}\right),$$

$$\langle \hat{a}^2 \rangle = \alpha^2 \left(1 - 2iK^2 \sin(\delta\theta) e^{i\delta\theta}\right),$$

$$\langle \hat{a}\hat{a}^\dagger \rangle = 1 + |\alpha|^2 + K^2(1 + 2|\alpha|^2 \sin(\delta\theta)^2) = 1 + \langle \hat{n} \rangle, \tag{6.77}$$

where K is $1/\sqrt{1 + |\alpha|^2 \sin(\delta\theta)^2}$. Note that K is always bounded between 0 and 1. The expectation value of the operators $\hat{X}$ and $\hat{Y}$ are accordingly given by

$$\langle \hat{X} \rangle = \frac{\alpha + \alpha^*}{2} + |\alpha| K^2 \sin(\delta\theta) \sin(\Delta\theta), \tag{6.78}$$

$$\langle \hat{Y} \rangle = \frac{\alpha - \alpha^*}{2i} - |\alpha| K^2 \sin(\delta\theta) \cos(\Delta\theta). \tag{6.79}$$

where $\delta\theta = \Delta\theta - \theta$. Therefore, both the phase difference $\delta\theta$ and the source phase $\Delta\theta$ must be determined. Note that when $\Delta\theta = \delta\theta$, the above expressions yield the coherent state results, for which the second term equals zero.

Next, the expectation value for the square of $\hat{X}$ and $\hat{Y}$ operators are

$$\langle \hat{X}^2 \rangle = \frac{1}{4} + \frac{\alpha^2 + \alpha^{*2}}{4} + \frac{|\alpha|^2}{2} + \frac{K^2}{2} \left[1 + 2|\alpha|^2 S_1\right], \tag{6.80}$$

where S_1 is $\sin(\delta\theta)[\sin(\delta\theta) + \sin(2\Delta\theta - \delta\theta)]$,

$$\langle \hat{Y}^2 \rangle = \frac{1}{4} - \frac{\alpha^2 + \alpha^{*2}}{4} + \frac{|\alpha|^2}{2} + \frac{K^2}{2} \left[1 + 2|\alpha|^2 S_2\right], \tag{6.81}$$

and S_2 equals $\sin(\delta\theta)[\sin(\delta\theta) - \sin(2\Delta\theta - \delta\theta)]$. The fluctuations of these operators are given by

$$\langle (\Delta\hat{X})^2 \rangle = \frac{1}{4} + K^2 \left[\frac{1}{2} - |\alpha|^2 K^2 \sin(\delta\theta)^2 \sin(\Delta\theta)^2\right], \tag{6.82}$$

$$\langle (\Delta\hat{Y})^2 \rangle = \frac{1}{4} + K^2 \left[\frac{1}{2} - |\alpha|^2 K^2 \sin(\delta\theta)^2 \cos(\Delta\theta)^2\right]. \tag{6.83}$$

From these relations, in general, a state is squeezed if one of the following conditions is satisfied

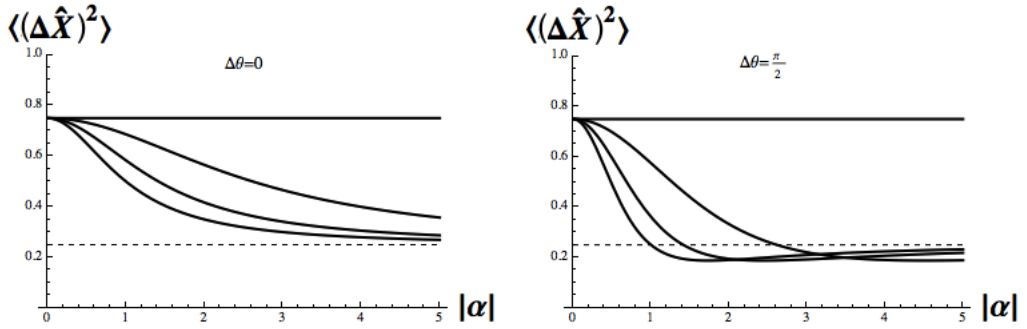

Figure 6.5: The fluctuation of $\hat{X}$ operator of the near coherent state for different values of $\Delta\theta$ and $\delta\theta$. Each plot displays curves, from top to bottom, $\delta\theta = 0, \pi/8, \pi/4, \pi/2$ where the straight line in both figures is the $\delta\theta = 0$ result.

$$\frac{1}{2} < |\alpha|^2 K^2 \sin(\delta\theta)^2 \sin(\Delta\theta)^2, \qquad \frac{1}{2} < |\alpha|^2 K^2 \sin(\delta\theta)^2 \cos(\Delta\theta)^2. \tag{6.84}$$

When $\delta\theta = 0$, Eqs.(6.82, 6.83) yield 3/4, which corresponds to the minimum fluctuation of one photon from Eq.(5.23). In Fig.(6.5) we display the fluctuations of the $\hat{X}$ operator for $\delta\theta$ and $\Delta\theta$ phase differences. This figure indicates the presence of squeezing for certain values of $\Delta\theta$. The maximum amount of squeezing occurs when $\delta\theta = \pi/2$ and $\Delta\theta = \pi/2$ [0] for the $\hat{X}$ [$\hat{Y}$] operator, and when $|\alpha| = \sqrt{3}$ for which Eq.(6.82) [Eq.(6.83)] yield 3/16, and Eq.(6.83) [Eq.(6.82)] yield 6/16. In contrast for a phase difference $\delta\theta = 0$ squeezing is not present.

The product of Eq.(6.82) and Eq.(6.83) always satisfies the upper and lower bounds

$$\frac{1}{16} \leq \langle(\Delta\hat{X})^2\rangle\langle(\Delta\hat{Y})^2\rangle \leq \frac{9}{16}. \tag{6.85}$$

For example, if both $\delta\theta$ and $\Delta\theta$ equal $\pi/2$, the product is

$$\langle(\Delta\hat{X})^2\rangle\langle(\Delta\hat{Y})^2\rangle = \frac{1}{16}\frac{(3+|\alpha|^2)(3+|\alpha|^4)}{(1+|\alpha|^2)^3}, \tag{6.86}$$

which equals 9/16 for $|\alpha| = 0$ and decreases to 1/16 for $|\alpha| \gg 1$. The product of Eq.(6.85) is bounded by the fluctuations of the vacuum and the photon unlike the SCS for which fluctuations are unbounded as α increases.

6.7.2 Q Mandel parameter

The Mandel Q-parameter, which was introduced in Sec.(5.4.3) of the previous chapter quantifies the photon number distribution and the anti-bunching properties. By substituting Eqs.(6.70,6.73) into the formula for the Mandel Q-parameter Eq.(5.83), we find

$$Q = \frac{2|\alpha|^2(2-M) - M^2}{|\alpha|^2 + M} \tag{6.87}$$

which is plotted in Fig.(6.6) against $|\alpha|^2$ for different values of $\delta\theta$. The Q parameter indicates that the phase differences between $\pi/4 < \delta\theta < 3\pi/4$ are uniformly negative implying anti-bunching while phases less than $\delta\theta < \pi/4$ are associated with bunching at large $|\alpha|$. In all cases when α is near zero the field is anti-bunched. The maximum anti-bunching for a given $|\alpha|$ occurs when $\delta\theta = \pi/2$. The anti-bunching of the near coherent state again confirms its nonclassicality.

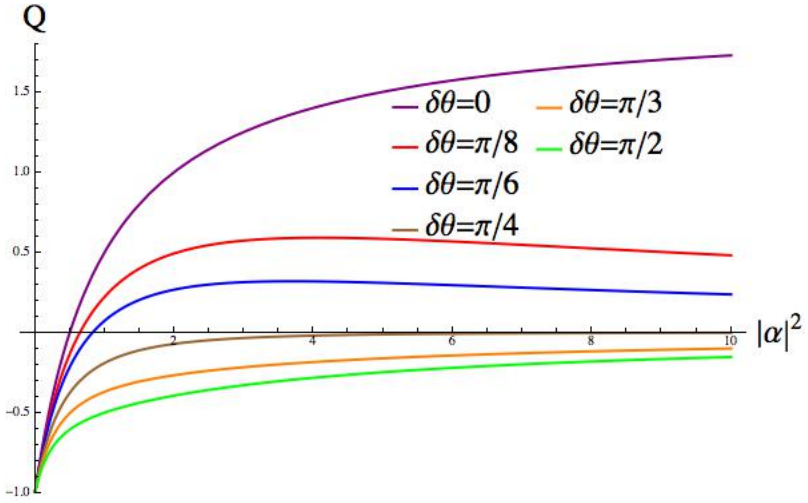

Figure 6.6: The Mandel Q-parameter of the near coherent state for different values of $\delta\theta$.

6.7.3 Wigner function

Calculating the Wigner function defined by Eq.(6.11) for a near coherent state with density matrix $\hat{\rho} = |\beta, \Delta\theta\rangle\langle\beta, \Delta\theta|$ gives

$$\begin{aligned} W(\alpha) &= -\tfrac{K^2}{\pi} e^{-2|\alpha-\beta|^2} \Big[2 - 8|\alpha|^2 - |\beta|^2(5 + 3\cos(2\delta\theta)) + (\alpha^*\beta + \alpha\beta^*)(6 + 2\cos(2\delta\theta)) \\ &\quad + 2i(\alpha^*\beta - \alpha\beta^*)\sin(2\delta\theta) \Big], \end{aligned} \tag{6.88}$$

which is plotted in Fig.(6.7) with $\alpha = \alpha_r + i\alpha_i$ for different values of $\delta\theta$. While the Wigner function appears to always possess negative regions for $\beta < 1$, as β increases the negative regions become smaller in extent except when $\delta\theta = 0$, for which the Wigner function always possesses large negative values as it reduces to

$$W(\alpha) = \frac{2}{\pi}(4|\alpha - \beta|^2 - 1)e^{-2|\alpha-\beta|^2}. \tag{6.89}$$

This behavior again results from the nonclassical nature of the near coherent state.

To summarize, the nonclassical properties of the near coherent state are most evident for either $\delta\theta = 0$ or $\delta\theta = \pi/2$. Squeezing and anti-bunching are maximized for $\delta\theta = \pi/2$, the Wigner function is most negative when $\delta\theta = 0$. Indeed, at $\delta\theta = 0$, the near coherent state becomes a pure derivative state as Eq.(6.31) demonstrates while when $\delta\theta = \pi/2$, the superposition between the derivative state and the coherent state is maximized.

6.8 Production

Generating a near coherent state requires a nonunitary procedure as is evident from Eq.(6.51). This also is true for SCSs which have nonunitary operators. Here we propose an extension to the Gerry's method for creating SCSs [198] depicted in Fig.(6.8). Here the Mach-Zehnder interferometer possesses two modes b and c, with one photon in mode b and zero photons in c. Two coherent states $|\alpha\rangle$ and $|\beta\rangle$ are incident as indicated in the figure. The interferometer is coupled to a nonlinear medium through the cross-Kerr interaction with mode a where the unitary operator of the nonlinear medium is $\hat{U}_{Kerr} = e^{-it\chi\hat{a}^\dagger\hat{a}\hat{b}^\dagger\hat{b}}$. The coefficient χ is related to the third order nonlinear susceptibility $\chi^{(3)}$, and t is the interaction time inside the medium and we additionally assume below that χt can be varied.

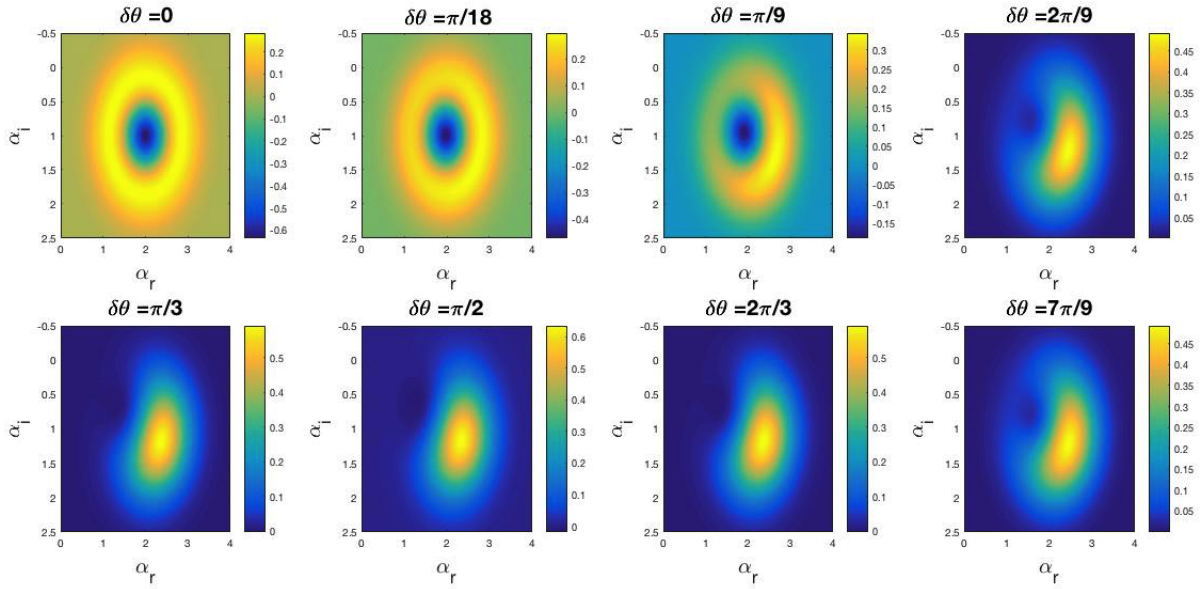

Figure 6.7: The Wigner function $W(\alpha)$ of the near coherent state for different phase differences $\delta\theta$ and $\beta = 2 + i$.

Denoting the phase shifter by φ, which its unitary operator is given by $\hat{U}_{shift} = e^{i\varphi\hat{c}^\dagger\hat{c}}$. Also assume that 50/50 splitters are employed in the two sides $\mathrm{BS}_{1,2}$ with the unitary operator $\hat{U}_{BS} = e^{i\frac{\pi}{4}(\hat{c}^\dagger\hat{b}+\hat{c}\hat{b}^\dagger)}$ while the final 50/50 beam splitter is represented by the unitary operator $U_{BS_3} = e^{i\frac{\pi}{4}(\hat{a}^\dagger\hat{d}+\hat{a}\hat{d}^\dagger)}$.

The entrance state in the system is then $|\alpha\rangle_a|1\rangle_b|0\rangle_c$. After the first beam splitter (BS_1), it becomes

$$|\alpha\rangle_a|1\rangle_b|0\rangle_c \to \frac{1}{\sqrt{2}}|\alpha\rangle_a(|1\rangle_b|0\rangle_c + i|0\rangle_b|1\rangle_c). \tag{6.90}$$

while after the phase shifter φ and the cross-Kerr interaction, the state is transformed to

$$\frac{1}{\sqrt{2}}|\alpha\rangle_a(|1\rangle_b|0\rangle_c + i|0\rangle_b|1\rangle_c) \to \frac{1}{\sqrt{2}}(|\alpha e^{-i\chi t}\rangle_a|1\rangle_b|0\rangle_c + ie^{i\varphi}|\alpha\rangle_a|0\rangle_b|1\rangle_c). \tag{6.91}$$

The third beam splitter (BS_3), which acts on mode a, yields

$$\to \frac{1}{\sqrt{2}}\left(\left|\frac{\beta+\alpha e^{-i\chi t}}{\sqrt{2}}\right\rangle_a|1\rangle_b|0\rangle_c + ie^{i\varphi}\left|\frac{\beta+\alpha}{\sqrt{2}}\right\rangle_a|0\rangle_b|1\rangle_c\right). \tag{6.92}$$

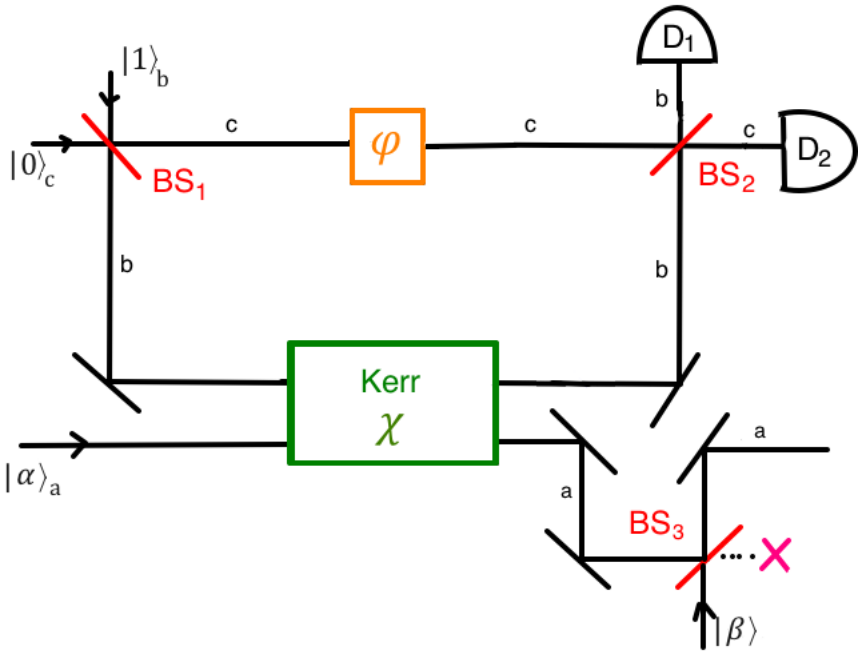

Figure 6.8: A procedure for generating the near coherent states.

while the second beam splitter (BS_2) generates

$$|1\rangle_b|0\rangle_c \to \frac{1}{\sqrt{2}}(|1\rangle_b|0\rangle_c + i|0\rangle_b|1\rangle_c), \qquad |0\rangle_b|1\rangle_c \to \frac{1}{\sqrt{2}}(|0\rangle_b|1\rangle_c + i|1\rangle_b|0\rangle_c). \tag{6.93}$$

After setting $\varphi = 0$ and rearranging terms, we obtain

$$|\psi(\chi t)\rangle = \frac{1}{2}\left\{|1\rangle_b|0\rangle_c\left[|\gamma + \Delta\gamma\rangle_a - |\gamma\rangle_a\right] + i|0\rangle_b|1\rangle_c\left[|\gamma + \Delta\gamma\rangle_a + |\gamma\rangle_a\right]\right\}. \tag{6.94}$$

Here $\gamma \equiv (\alpha + \beta)/\sqrt{2}$ and $\Delta\gamma \equiv \alpha(e^{-i\chi t} - 1)/\sqrt{2}$.

If an event is registered in D_1 , the state projected on mode a is $|\gamma + \Delta\gamma\rangle - |\gamma\rangle$, while if D_2 detects an event , the projected state is $i|\gamma + \Delta\gamma\rangle + |\gamma\rangle$. If $\chi t \to 2\pi$, $\Delta\gamma$ becomes $\approx \frac{|\alpha|}{\sqrt{2}}(\chi t - 2\pi)e^{i(\theta + 3\pi/2)}$, which approaches zero as $\chi t \to 2\pi$ and can therefore function as the source of a near coherent state with $\Delta\theta_{effective} = \theta + 3\pi/2$. This method can also be applied with $\chi t \to 0$, if the interaction time is suitably small.

After performing the normalization, the projected state in a when D_1 fires is a near coherent state with

$$|\gamma, \Delta\theta_{effective}\rangle = \lim_{|\Delta\gamma| \to 0} C_\gamma(|\gamma + \Delta\gamma\rangle - |\gamma\rangle). \tag{6.95}$$

To insure that the near coherent state is obtained, χt must be close to but not exactly 2π. If β and α possess the same amplitude but different phases, we can write $\alpha = |\alpha|e^{i\theta}, \beta = |\alpha|e^{is}$. Then, the amplitude of the near coherent state is $|\gamma| = |\alpha|\sqrt{\frac{1+\cos(\theta-s)}{2}}$, and its phase is $\theta_{effective} = \frac{\theta+s}{2}$ so that the phase difference is

$$\delta\theta_{effective} = \Delta\theta_{effective} - \theta_{effective} = \frac{\theta - s}{2} + \frac{3\pi}{2}. \tag{6.96}$$

The value $\delta\theta_{effective}$ can possess any value in the range $0 - 2\pi$, so, at least in principle, by adjusting the phases of the input coherent states $|\alpha\rangle$ and $|\beta\rangle$, a near coherent state can be produced with any phase difference and amplitude.

6.9 Conclusion

To conclude, in this chapter we investigated a particular superposition of two coherent states which is characterized by a new parameter, the source phase. While the state is a particular superposition of two coherent states, it can be expressed as a superposition of coherent state and a derivative state, each weighted with a separate function of the phase difference. We demonstrated that this state is nonclassical and provided a possible method for generating it experimentally.

While the near coherent state is a superposition of coherent states, its properties are different than the standard SCSs. Instead, its properties resemble those of coherent states, but are nonclassical. For example, when $\delta\theta = \pi/2$, the photon probability distribution adopts a quasi-Poissonian distribution and the quadrature space becomes a semi-Gaussian function.

This state can be applied to study the quantum interfaces from other perspectives. This is true because of the fact that this state is nonvanishing and a function of the source phase. Also, the nonclassical properties of this state can be applied in standard fashion to a variety of applications in quantum optics and information.

Bibliography

[1] Anas Othman and David Yevick, Stretchable photonic crystal design, Opt. and Quant. Electron. , **48**, 207 (2016).

[2] Anas Othman and David Yevick, Enhanced negative refractive index control in a 5-level system, J. Mod. Opt. , **64**, 1208 (2017).

[3] Anas Othman and David Yevick, The interaction of a N-type four level atom with the electromagnetic field for a Kerr medium induced intensity-dependent coupling, Int. J. Theor. Phys., **57**, 159 (2018).

[4] Anas Othman, David Yevick and Mohammed Al-Amri, Generation of three wide frequency bands within a single white light cavity, (**submitted**).

[5] Anas Othman, The superposition of two identical states: The empty state, Photonics North (PN), (2016).

[6] J. D. Joannopoulos, S. G. Johnson, J. N. Winn, R. D. Meade, Photonic Crystals, Molding the flow of light, Princeton University Press, Second Edition (2008).

[7] S. Noda, Recent progresses and future prospects of two- and three-dimensional photonic crystals. IEEE J. Lightwave Technol. **24**, 4554 (2006).

[8] K. Staliunas, Spatial filtering of light beams in chirped photonic crystals. IEEE/LEOS Winter Topicals Meeting Series (Innsbruck, Austria), pp. 176-177 (2009).

[9] D. Englund, D. Fattal, E. Waks, et al., Controlling the spontaneous emission rate of single quantum dots in a two-dimensional photonic crystal. Phys. Rev. Lett. **95**, 013904 (2005).

[10] A.M. Kasten, M.P. Tan, J.D. Sulkin, et al., Photonic crystal vertical cavity lasers with wavelength-independent single-mode behavior. IEEE photon. Technol. Lett. **20**, 2010 (2005).

[11] E. Yablonovitch, Inhibited spontaneous emission in solid-state physics and electronics. Phys. Rev. Lett. **58**, 2059 (1987).

[12] I. A. Sukhoivanov and I. V. Guryev, Photonic Crystals, Physics and Practical Modeling, Springer Series in optical sciences, pp. 46-50 (2009).

[13] K. Sakoda, Optical properties of photonic crystals, Springer Series in optical sciences (2001).

[14] S. Obayya, Computational photonics, John Wiley & Sons Ltd. (2011).

[15] M. S. Wartak, Computational photonics; an introduction with MATLAB, Cambridge University Press (2013).

[16] M. Notomi, K. Yamada, et al., Extremely large group-velocity dispersion of line-defect waveguides in photonic crystal slabs, Phys. Rev. Lett. **87**, 253902 (2001).

[17] W. T. Lau and S. Fan, Creating large bandwidth line defects by embedding dielectric waveguides into photonic crystal slabs, Appl. Phys. Lett. **81**, 3915 (2002).

[18] S. G. Johnson, P. R. Villeneuve, et al., Linear waveguides in photonic-crystal slabs, Phys. Rev. B **62**, 8212 (2000).

[19] Y. Sugimoto, T. Yu Tanaka, I. Naoki, et al., Low propagation loss of 0.76 dB/mm in GaAs-based single-line- defect two-dimensional photonic crystal slab waveguides up to 1 cm in length, Opt. Express **12**, 1090 (2004).

[20] K. R. inendra, S. W. Robert, and J. S. Andrew, Visible continuum generation in air-silica microstructure optical fibers with anomalous dispersion at 800 nm, Opt. Lett. **25**, 25 (2000).

[21] A. Mendez and T. F. Morse, Specialty Optical Fibers Handbook, Elsevier Inc. (2000).

[22] S. G. Johnson, M. Ibanescu, et al., Low-loss asymptotically single-mode propagation in large-core OmniGuide fibers, Opt. Express **9**, 748 (2001).

[23] M. Ibanescu, S. G. Johnson, et al., Analysis of mode structure in hollow dielectric waveguide fibers, Phys. Rev. E **67**, 046608 (2003).

[24] M. R. Watts, S. G. Johnson, et al., Electromagnetic cavity with arbitrary Q and small modal volume without a complete photonic bandgap, Opt. Lett. **27**, 1785 (2002).

[25] B.-S. Song, S. Noda, et al., Ultra-high-Q photonic double-heterostructure nanocavity, Nature Mater. **4**, 207 (2005).

[26] M Augustin, R Iliew, C Etrich, et al., Dispersion properties of photonic crystal waveguides with a low in-plane index contrast, New J. Phys. **8** 210 (2006).

[27] D. Yang, H. Tian, and Y. Ji, Nanoscale photonic crystal sensor arrays on monolithic substrates using side-coupled resonant cavity arrays, Opt. Express **19**, 20023 (2011).

[28] L. Gan and Z. Li, Designs and experiments on infrared two-dimensional silicon photonic crystal slab devices, Front. Optoelec. **5**, 21 (2012).

[29] M. Eichenfield, R. Camacho, et al., A picogram- and nanometre-scale photonic-crystal optomechanical cavity, Nature **459**, 550 (2009).

[30] S. Vignolini, F. Riboli, et al., Local nanofluidic light sources in silicon photonic crystal microcavities, Phys. Rev. E **78**, 045603(R) (2008).

[31] Z. Lu and Y. Yin, Colloidal nanoparticle clusters: functional materials by design, Chem. Soc. Rev, **41**, 6874 (2012).

[32] M. G. Han, C. G. et al., Full Color Tunable Photonic Crystal from Crystalline Colloidal Arrays with an Engineered Photonic Stop-Band, Adv. Materials **24**, 6438 (2012).

[33] X. Zhu, Y. Zhang, et al., Two-dimensional photonic crystals with anisotropic unit cells imprinted from poly (dimethylsiloxane) membranes under elastic deformation, Appl. Phys. Lett. **93**, 161911 (2008).

[34] H. Wang and K.-Q. Zhang, Photonic Crystal Structures with Tunable Structure Color as Colorimetric Sensors, Sensors **13**, 4192 (2013).

[35] L. Y. Chun, K. Hyunwoo, et al., Stretchable Photonic Crystal Cavity with Wide Frequency Tunability" Nano Lett. **13**, 248 (2013).

[36] K. X. Wang, Z. Yu, et al., Light trapping in photonic crystals, Energy Env. Sci., **7**, 2725 (2014).

[37] P. Bienstman, S. Assefa, et al., Taper structures for coupling into photonic crystal slab waveguides, J. Opt. Soc. Am. B **20**, 1817 (2003).

[38] V. G. Veselago, The electrodynamics of substances with simultaneously negative values of ϵ and μ, Sov. Phys. Usp. **10**, 509 (1968).

[39] M. W. Feise, P. J. Bevelacqua, and J. B. Schneider, Effects of surface waves on the behavior of perfect lenses, Phys.Rev. B **66**, 035113 (2002).

[40] K. Aydin, I. Bulu, and E. Ozbay, Subwavelength resolution with a negative-index metamaterial superlens, Appl. Phys. Lett. **90**, 254102 (2007).

[41] J. B. Pendry, Negative Refraction Makes a Perfect Lens, Phys. Rev. Lett. **85**, 3966 (2000).

[42] D. R. Smith, W. J. Padilla, D. C. Vier, S. C. Nemat-Nasser, and S. Schultz, Composite medium with simultaneously negative permeability and permittivity, Phys. Rev. Lett. **84**, 4184 (2000).

[43] R. A. Shelby, D. R. Smith, and S. Schultz, Experimental Verification of a Negative Index of Refraction, Science **292**, 77 (2001).

[44] T. J. Yen, W. J. Padilla, N. Fang, D. C. Vier, D. R. Smith, J. B. Pendry, D. N. Basov, and X. Zhang, Terahertz Magnetic Response from Artificial Materials, Science 303, 1494 (2004).

[45] Stefan Linden, Christian Enkrich, Martin Wegener, Jiangfeng Zhou, Thomas Koschny, and C. M. Soukoulis, Magnetic Response of Metamaterials at 100 Terahertz, Science **306**, 1351 (2004).

[46] J. B. Pendry, A Chiral Route to Negative Refraction, Science **306**, 1353 (2004).

[47] C. Enkrich, M. Wegener, S. Linden, S. Burger, L. Zschiedrich, F. Schmidt, J. F. Zhou, Th. Koschny, and C. M. Soukoulis, Magnetic Metamaterials at Telecommunication and Visible Frequencies, Phys. Rev. Lett. **95**, 203901 (2005).

[48] E. Cubukcu, K. Aydin, E. Ozbay. S. Foteinopoulou, and C. M. Soukoulis, Electromagnetic waves: Negative refraction by photonic crystals, Nature (London) **423**, 604 (2003).

[49] Sailing He, Zhichao Ruan, Long Chen, and Jianqi Shen, Focusing properties of a photonic crystal slab with negative refraction, Phys. Rev. B **70**, 115113 (2004).

[50] A. Berrier, M. Mulot, M. Swillo, M. Qiu, L. Thylen, A. Talneau, and S. Anand, Negative Refraction at Infrared Wavelengths in a Two-Dimensional Photonic Crystal, Phys. Rev. Lett. **93**, 073902 (2004).

[51] M. O. Scully, and M. S. Zubairy, Quantum optics, Cambridge university press (1997).

[52] W. Becker, On the equivalence of the rE and the pA interaction hamiltonian, Opt. Commun. **56**, 107 (1985).

[53] C.-T. Claude, D.-R. Jacques, and G., Gilbert, Atom-Photon Interactions: Basic Processes and Applications, Wiley (1992).

[54] H.-P. Breuer and F. Petruccione, The Theory of Open Quantum Systems, Oxford University Press, Page.(117).

[55] Shuncai Zhao, Zhengdong Liu, and Qixuan Wu, Zero absorption and a large negative refractive index in a left-handed four-level atomic medium, J. Phys. B: At. Mol. Opt. Phys. **43**, 045505 (2010).

[56] Shun-Cai Zhao, Zheng-Dong Liu, and Qi-Xuan Wu, Negative refraction without absorption via both coherent and incoherent fields in a four-level left-handed atomic system, Opt. Comm. **283**, 3301 (2010).

[57] Huifang Zhang, Haihong Ren, Xiaona Yan, and Lihua Bai, Quantum-interference and the concentration of Er^{3+} ion effect on left-handedness with zero absorption and large negative refractive index in Er^{3+}:YAG crystal, J. Mod. Opt. **59**, 1133 (2012).

[58] J.-Q. Shen, Gain-assisted negative refractive index in a quantum coherent medium, Prog. Electromagn. Res. **133**, 37 (2013).

[59] Michael Fleischhauer, Atac Imamoglu, and Jonathan P. Marangos, Electromagnetically induced transparency: Optics in coherent media, Rev. Mod. Phys. **77**, 633 (2005).

[60] Shun-Cai Zhao, Xiao-Fan Qian, Ya-Ping Zhang, and Yong-An Zhang, Negative Refraction with Little Loss Manipulated by the Voltage and Pulsed Laser in Double Quantum Dots, Prog. Theor. Phys. **128**, 243 (2012).

[61] Zhao S.C., Zhang S. Y. and Xu Y. Y., Large and tunable negative refractive index via electromagnetically induced chirality in a semiconductor quantum well nanostructure, Jetp Lett. **100**, 385 (2014).

[62] Zhao Shun-Cai, Zhang Shuang-Ying, Wu Qi-Xuan and Jia Jing, Left-Handedness with Three Zero-Absorption Windows Tuned by the Incoherent Pumping Field and Inter-Dot Tunnelings in a GaAs/AlGaAs Triple Quantum Dots System, Chin. Phys. Lett. **32**, 058104 (2015).

[63] Q. Thommen and P. Mandel, Electromagnetically Induced Left Handedness in Optically Excited Four-Level Atomic Media, Phys. Rev. Lett. **96**, 053601 (2006).

[64] J. Kästel, M. Fleischhauer, S. F. Yelin, and R. L. Walsworth, Tunable Negative Refraction without Absorption via Electromagnetically Induced Chirality, Phys. Rev. Lett. **99**, 073602 (2007).

[65] Fu-li Li, Ai-ping Fang, and Meng Wang, Electromagnetic chirality-induced negative refraction via atomic coherence, J. Phys. B: At. Mol. Opt. Phys. **42**, 195505 (2009).

[66] D. E. Sikes and D. D. Yavuz, Negative refraction with low absorption using Raman transitions with magnetoelectric coupling, Phys. Rev. A **82**, 011806(R) (2010).

[67] Peter P. Orth, Roman Hennig, Christoph H. Keitel, and Jörg Evers, Negative refraction with tunable absorption in an active dense gas of atoms, New J. Phys. **15**, 013027 (2013).

[68] M.Ö. Oktel and Ö. E. Müstecaplioğlu, Electromagnetically induced left-handedness in a dense gas of three-level atoms, Phys. Rev. A **70** ,053806 (2004).

[69] M. O. Scully, Enhancement of the index of refraction via quantum coherence, Phys. Rev. Lett. **67**, 1855 (1991).

[70] C. S. Zhao, and D. Z. Liu, Left-handness in a four-level atomic system, Int. J. Quant. Inf. **7**, 747 (2009).

[71] Ai-Ping Fang, Wenchao Ge, Meng Wang, Fu-li Li, and M. Suhail Zubairy, Negative refraction without absorption via quantum coherence, Phys. Rev. A **93**, 023822 (2016).

[72] J. Mlynek and W. Lange, A simple method of observing coherent ground state transients, Opt. Commun. **30**, 337 (1979).

[73] M. Fleischhauer, C. H. Keitel, M. O. Scully, C. Su, B. T. Ulrich, and S. Y. Zhu, Resonantly enhanced refractive index without absorption via atomic coherence, Phys. Rev. A **46**, 1468 (1992).

[74] M. Jain, H. Xia, G. Y. Yin, A. J. Merriam, and S. E. Harris, Efficient Nonlinear Frequency Conversion with Maximal Atomic Coherence, Phys. Rev. Lett. 77, 4326 (1996).

[75] J. D. Jackson, Classical Electrodynamics, Wiley, New York, (1998).

[76] R. A. Depine and A. Lakhtakia, Microw., A new condition to identify isotropic dielectric-magnetic materials displaying negative phase velocity, Opt. Technol. Lett. **41**, 315 (2004).

[77] R. X. Adikhari, Gravitational radiation detection with laser interferometry, Rev. Mod. Phys. **86**, 121 (2014).

[78] A. Buonanno, Y. Chen, Scaling law in signal recycled laser-interferometer gravitational-wave detectors, Phys. Rev. D, **67**, 62002 (2003).

[79] W. K. Chang, Y. H. Chen, and J. W. Chang, Pulsed orange generation optimized in a diode-pumped Nd:YVO_4 laser using monolithic dual PPLN electro-optic Q switches, Opt. Lett. **35**, 2687 (2010).

[80] T. Shigeki, M. Masanao, and S. Seiji, 12?W Q-switched Er:ZBLAN fiber laser at 2.8?μ m, Opt. Lett. **36**, 2812 (2011).

[81] M. Skorczakowski et al., Mid-infrared Q-switched Er:YAG laser for medical applications, Laser Phys. Lett. **7**, 498 (2010).

[82] P. Peng and F.-L. Li, Entangling two atoms in spatially separated cavities through both photon emission and absorption processes, Phys. Rev. A **75**, 062320 (2007).

[83] J. I. Cirac, P. Zoller, H. J. Kimble and H. Mabuchi, Quantum State Transfer and Entanglement Distribution among Distant Nodes in a Quantum Network, Phys. Rev. Lett. **78**, 3221 (1997).

[84] H. J. Kimble, The quantum internet, Nature **453**, 1023 (2008).

[85] L.-M Duan and C. Monroe, Colloquium: Quantum networks with trapped ions, Rev. Mod. Phys. **82**, 1209 (2010).

[86] L.-G. Wang, M. Ikram, and M. S. Zubairy, Control of the Goos-Hanchen shift of a light beam via a coherent driving field, Phys. Rev. A **77**, 023811 (2008).

[87] J.-X. Zhang, H.-T. Zhou, D.-W. Wang, and S.-Y. Zhu, Enhanced reflection via phase compensation from anomalous dispersion in atomic vapor, Phys. Rev. A **83**, 053841 (2011).

[88] H.-T. Zhou, D.-W. Wang, D. Wang, J.-X. Zhang, and S.-Y. Zhu, Efficient reflection via four-wave mixing in a Doppler-free electromagnetically-induced-transparency gas system, Phys. Rev. A **84**, 053835 (2011).

[89] D. Yafan, L. Gongwei, Z. Shicheng, N. Yueping, G. Shangqing, Low light level all-optical switching in a four-level atom-cavity system, Opt. Commun. **358**, 73 (2016).

[90] B. Dayan, A. S. Parkins, T. Aoki, E. P. Ostby, K. J. Vahala, and H. J. Kimble, A Photon Turnstile Dynamically Regulated by One Atom, Science **319**, 1062 (2008).

[91] A. W. Brown and M. Xiao, All-optical switching and routing based on an electromagnetically induced absorption grating, Opt. Lett. **30**, 699 (2005).

[92] X. M. Su, B. S. Ham, Dynamic control of the photonic band gap using quantum coherence, Phys. Rev. A **71**, 013821 (2005).

[93] R. S.-Bonabi, T. Naseri, and M. N.-Toupchi, Electromagnetically induced grating in the microwave-driven four-level atomic systems, Applied Opt. **54**, 368 (2015).

[94] J. Xu, M. Al-Amri, Y. Yang, S.-Y. Zhu and M. S. Zubairy, Wide-band optical switch via white light cavity, Phys. Rev. A **86**, 033828 (2012).

[95] G. S. Pati, M. Salit, K. Salit and M. S. Shahriar, Demonstration of a Tunable-Bandwidth White-Light Interferometer Using Anomalous Dispersion in Atomic Vapor, Phys. Rev. Lett. **99**, 133601 (2007).

[96] R. H. Rinkleff, A. Wicht, The Concept of White Light Cavities Using Atomic Phase Coherence, Physica Scripta **T118**, 85 (2005).

[97] A. Rocco, A. Wicht, R.-H.Rinkleff, K. Danzmann, Anomalous dispersion of transparent atomic two- and three-level ensembles, Phys.Rev. A **66**, 053804 (2002).

[98] A. Wicht, K. Danzmann, M. Fleischhauer, M. Scully, G. Miller, R.H. Rinkleff, White-light cavities, atomic phase coherence, and gravitational wave detectors, Opt. Commun. **134**, 431 (1997).

[99] R.-H. Rinkleff and A. Wicht, The Concept of White Light Cavities Using Atomic Phase Coherence, Phys. Scr. **T118**, 85 (2005).

[100] Qingqing Sun, M. Selim Shahriar, and M. Suhail Zubairy, Effects of noise and parameter deviations in a bichromatic Raman white light cavity, Phys. Rev. A **81**, 033826 (2010).

[101] K.-J. Boller, A. Imamoǵlu, and S. E. Harris, Observation of electromagnetically induced transparency, Phys. Rev. Lett. **66**, 2593 (1991).

[102] M. Mücke, E. Figueroa, J. Bochmann et al., Electromagnetically induced transparency with single atoms in a cavity, Nature (London) **465**, 755 (2010).

[103] M. O. Scully, Enhancement of the index of refraction via quantum coherence, Phys. Rev. Lett. **67**, 1855 (1991).

[104] Y. Zhang, Y.-M. Liu et al., Phase control of stationary light pulses due to a weak microwave coupling, Opt. Comm. **343**, 183 (2015).

[105] Y.-W. Lin, W.-T. Liao et al., Stationary Light Pulses in Cold Atomic Media and without Bragg Gratings, Phys. Rev. Lett. **102**, 213601 (2009).

[106] M. Cheneau et al., Geometric potentials in quantum optics: A semi-classical interpretation, Europhys. Lett. **83**, 60001 (2008).

[107] D. F. Phillips, A. Fleischhauer, A. Mair, R. L. Walsworth, and M. D. Lukin, Storage of Light in Atomic Vapor, Phys. Rev. Lett. **86**, 783 (2001).

[108] C. Liu, Z. Dutton, C. H. Berhoozi, and L. V. Hau, Observation of coherent optical information storage in an atomic medium using halted light pulses, Nature (London) **409**, 490 (2001).

[109] E. A. Korsunsky and D. V. Kosachov, Phase-dependent nonlinear optics with double-? atoms, Phys. Rev. A **60**, 4996 (1999).

[110] D. Arsenović and J. Dimitrijević, Comparison of a double-Λ atomic scheme with single- and two-fold coupled transitions, Phys. Scr. **T149**, 014008 (2012).

[111] V. V. Dodonov, V. I. Man'ko, theory of nonclassical states of light, CRC Press, (2003).

[112] V. V. Dodonov, 'Nonclassical' states in quantum optics: a squeezed' review of the first 75 years, J. Opt. B: Quantum Semiclass. Opt. **4**, R1 (2002).

[113] M.C. de Oliveira, W.J. Munro, Nonclassicality and information exchange in deterministic entanglement formation, Phys. Lett. A **320**, 352 (2004).

[114] M.S. Kim, W. Son, V. Buzek, P.L. Knight, Entanglement by a beam splitter: Nonclassicality as a prerequisite for entanglement, Phys. Rev. A **65**, 032323 (2002).

[115] Girish S. Agarwal, Quantum Optics, Cambridge University Press, (2013).

[116] Roy J. Glauber, Coherent and Incoherent States of the Radiation Field, Phys. Rev. **131**, 2766 (1963).

[117] Rodney Loudon, The Quantum Theory of Light, Third edition, Oxford university press, (2000).

[118] E. T. Jaynes and F. W. Cummings, Comparison of quantum and semiclassical radiation theories with application to the beam maser, Proc. IEEE **51**, 89 (1963).

[119] H. I. Yoo and J. H. Eberly, Dynamical theory of an atom with two or three levels interacting with quantized cavity fields, Phys. Rep. **118**, 239 (1985).

[120] P.L. Knight and P.M. Radmore, Quantum revivals of a two-level system driven by chaotic radiation, Phys. Lett. A **90**, 342 (1982).

[121] G. Rempe and H. Walther, Observation of quantum collapse and revival in a one-atom maser, Phys. Rev. Lett. **58**, 353 (1987).

[122] D. F. Walls and G. J. Milburn, Quantum Optics, Springer, Berlin (1994).

[123] J. Perina, Quantum Statistics of Linear and Nonlinear Optical Phenomena, Reidel, Dordrecht (1984).

[124] J. H. Eberly, N. B. Narozhny, and J. J. Sanchez-Mondragon, Periodic Spontaneous Collapse and Revival in a Simple Quantum Model, Phys. Rev. Lett. **44**, 1323 (1980).

[125] Bruce W. Shore and Peter L. Knight, The Jaynes-Cummings Model, Journal of Modern Optics, **40**, 1195 (1993).

[126] P. Meystre M. S. Zubairy, Squeezed states in the Jaynes-Cummings model, Phys. Lett. A **89**, 390 (1982).

[127] P. K. Aravind and G. H. Hu, Influence of initial conditions on squeezing and anti-bunching in the Jaynes-Cummings model, Physica B+C **150**, 427 (1988).

[128] M. F. Fang, S. Swain, and P. Zhou, Super-revivals, chaos, and entanglement of a trapped ion in a standing wave, Phys. Rev. A **63**, 013812 (2000).

[129] D. A. Cardimona, Effect of atomic-state coherence and spontaneous emission on three-level dynamics, Phys. Rev. A **41**, 5016 (1990).

[130] M. J. Faghihi, M. K. Tavassoly and M. Bagheri Harouni, Tripartite entanglement dynamics and entropic squeezing of a three-level atom interacting with a bimodal cavity field, Laser Phys. A **24**, 045202 (2014).

[131] F. F. A. El-Orany, Relationship between the atomic inversion and Wigner function for multi-mode multiphoton Jaynes?Cummings model, J. Phys. A: Math. Gen. **37**, 6157 (2004).

[132] M. S. Abdalla, E. M. Khalil and A-S F. Obada , Statistical properties of a two-photon cavity mode in the presence of degenerate parametric amplifier, Ann. Phys. **322**, 2554 (2007).

[133] S. Mahmood and M. S. Zubairy, Cooperative atomic interactions in a single-mode laser, Phys. Rev. A **35**, 425 (1987).

[134] H. Hekmatara and M. K. Tavassoly, Sub-Poissonian statistics, population inversion and entropy squeezing of two two-level atoms interacting with a single-mode binomial field: intensity-dependent coupling regime, Opt. Commun. **319**, 121 (2014).

[135] Sántos-Sanchez O de los and J. Récamier, The f-deformed Jaynes-Cummings model and its nonlinear coherent states, J. Phys. B: At. Mol. Opt. Phys. **45**, 015502 (2012).

[136] J. P. Marangos, Electromagnetically induced transparency, J. Mod. Opt. **45**, 471 (1998).

[137] J. C. Bergquist, Randall G. Hulet, Wayne M. Itano, and D. J. Wineland, Observation of Quantum Jumps in a Single Atom, Phys. Rev. Lett. **57**, 1699 (1986).

[138] B. J. Dalton, R. McDuff and P. L. Knight, Coherent Population Trapping, J. Mod. Opt. **32**, 61 (1985).

[139] H. R. Baghshahi, M. K. Tavassoly and A. Behjat, Entropy squeezing and atomic inversion in the k-photon Jaynes?Cummings model in the presence of the Stark shift and a Kerr medium: A full nonlinear approach, Chin. Phys. B **23**, 074203 (2014).

[140] B. Buck and C.V. Sukumar, Exactly soluble model of atom-phonon coupling showing periodic decay and revival, Phys. Lett. A **81**, 132 (1981).

[141] M. F. Fang and H. E. Liu, Properties of entropy and phase of the field in the two-photon Jaynes-Cummings model with an added Kerr medium, Phys. Lett. A **200**, 250 (1995).

[142] F.F.A. El-Orany, Revival-collapse phenomenon in the quadrature squeezing of the multiphoton intensity-dependent Jaynes-Cummings model, J. Mod. Opt. **53**, 1699 (2006).

[143] A. S. F. Obada, S. A. Hanoura, and A. A. Eied, Entropy of a general three-level atom interacting with a two mode, Laser Phys. **23**, 025201 (2013).

[144] A. S. F. Obada, S. A. Hanoura, and A. A. Eied, Entanglement for a general formalism of a three-level atom in a V-configuration interacting nonlinearly with a non-correlated two-mode field, Laser Phys. **23**, 055201 (2013).

[145] M.J. Faghihi and M.K. Tavassoly, Dynamics of entropy and nonclassical properties of the state of a Λ-type three-level atom interacting with a single-mode cavity field with intensity-dependent coupling in a Kerr medium, J. Phys. B: At. Mol. Opt. Phys. **45**, 035502 (2012).

[146] R.A. Zait, Nonclassical statistical properties of a three-level atom interacting with a single-mode field in a Kerr medium with intensity dependent coupling, Phys. Lett. A **319**, 461 (2003).

[147] G.R. Honarasa and M.K. Tavassoly, Generalized deformed Kerr states and their physical properties, Phys. Scr. **86**, 035401 (2012).

[148] R.A. Zait, Four-level Hamiltonian model with an additional Kerr medium and multiphoton processes, Opt. Commun. **247**, 367 (2005).

[149] M. Bina, F. Casagrande, and A. Lulli, Exact results on decoherence and entanglement in a system of N driven atoms and a dissipative cavity mode, Eur. Phys. J. D **49**, 257 (2008).

[150] K. Wang, Y. Gu, and Q.H. Gong, Stimulated emission and multi-peaked absorption in a four level N-type atom, Chin. Phys. **16** 130 (2007).

[151] Y.H. Wang, L. Hao, X. Zhou, and G.L. Long, Behavior of quantum coherence of ?-type four-level atom under bang?bang control, Opt. Commun. **281**, 4793 (2008).

[152] H.R. Baghshahi, M.K. Tavassoly and A. Behjat, Dynamics of entropy and nonclassicality features of the interaction between a $\diamondsuit$-type four-level atom and a single-mode field in the presence of intensity-dependent coupling and Kerr nonlinearity, Commun. Theor. Phys. **62**, 430 (2014).

[153] A. A. Eied, S.A. Hanoura, and A. S. F. Obada, Quantum Entropy of a Four-Level Atom with Arbitrary Nonlinearities, Int. J. Theor. Phys. **51**, 2665 (2012).

[154] S. E. Harris and Y. Yamamoto, Photon Switching by Quantum Interference, Phys. Rev. Lett. **81**, 3611 (1998).

[155] M. Yan et al., Observation of absorptive photon switching by quantum interference, Phys. Rev. A **64**, 041801 (2001).

[156] W. Xu and J. Y. Gao, Absorption mechanism in a four-level system, Phys. Rev. A **67**, 033816 (2003).

[157] C. Goren, A. D. Wilson-Gordon, M. Rosenbluh M and H. Fried-mann, Atomic four-level N systems, Phys. Rev. A **69**, 053818 (2004).

[158] H. Schmidt and A. Imamoglu, Giant Kerr nonlinearities obtained by electromagnetically induced transparency, Opt. Lett. **21**, 1936 (1996).

[159] N. H. Abdel-Wahab, The interaction between a four-level N-type atom and two-mode cavity field in the presence of a Kerr medium, J. Phys. B: At. Mol. Opt. Phys. **40**, 4223 (2007).

[160] N. H. Abdel-Wahab, A moving four-level N-type atom interacting with cavity fields, J. Phys. B: At. Mol. Opt. Phys. **41**, 105502 (2008).

[161] N. H. Abdel-Wahab and Lamia Thabet, The influence of the relative phase on the interaction between a single mode cavity field and a four-level N-type atom, Eur. Phys. J. Plus **128**, 52 (2013).

[162] N. H. Abdel-Wahab and Lamia Thabet, Dynamics of N-configuration four-level atom interacting with one-mode cavity field, Eur. Phys. J. Plus **129**, 144 (2014).

[163] V. M. Éntin et al., Experimental implementation of a four-level N-type scheme for the observation of Electromagnetically Induced Transparency, JETP Lett. **71**, 175 (2000).

[164] L.N. Childs, A Concrete Introduction to Higher Algebra, 3rd ed., Springer, Berlin (2008).

[165] D. Auckly, Solving the Quartic with a Pencil, Amer. Math. Monthly **114**, 29 (2007).

[166] V.I. Man'ko, G. Marmo, E.C.G. Sudarshan, and F. Zaccaria, f-Oscillators and Nonlinear Coherent States, Phys. Scr. **55**, 528 (1997).

[167] L. Mandel, Sub-Poissonian photon statistics in resonance fluorescence, Opt. Lett. **4**, 205 (1979).

[168] H. P. Yuen, Two-photon coherent states of the radiation field, Phys. Rev. A **13**, 2226 (1976).

[169] B. L. Schumaker and C. M. Caves, New formalism for two-photon quantum optics. II. Mathematical foundation and compact notation, Phys. Rev. A **31**, 3093 (1985).

[170] Scott C. Glancy, Hilma M. Vasconcelos, Methods for Producing Optical Coherent State Superpositions, Journal of the Optical Society of America B-Optical Physics, **25**, 712 (2008).

[171] H. Jeong and M. S. Kim, Purification of entangled coherent states, Quantum Information & Computation, **2**, 208 (2002).

[172] H. Jeong and T. C. Ralph, Quantum Information with Continuous Variables of Atoms and Light, **Chapter**: Schrodinger Cat States for Quantum Information Processing, Imperial College Press, 160 (2007).

[173] G. S. Agarwal, R. R. Puri, and R. P. Singh, Atomic Schrdinger cat states, Phys. Rev. A **56**, 2249 (1997).

[174] Robert McConnell, Hao Zhang, Senka Cuk, Jiazhong Hu, Monika H. Schleier-Smith, and Vladan Vuletic, Generating entangled spin states for quantum metrology by single-photon detection, Phys. Rev. A **88**, 063802 (2013).

[175] Dong Chuan-hua, Superposition coherent states and their properties, Journal of Shanghai University (English Edition), **4**, 112 (2000).

[176] C.C. Gerry, Non-classical properties of even and odd coherent states, J. Mod. Opt. **40**, 1053 (1993).

[177] W. Schleich, M. Pernigo, and Fam Le Kien, Nonclassical state from two pseudoclassical states, Phys. Rev. A **44**, 2172 (1991).

[178] W. Schleich, J.P. Dowling, R.J. Horowicz, S. Varro, in: A. Barut (Ed.), New Frontiers in Quantum Optics and Quantum Electrodynamics, Plenum, New York (1990).

[179] R. Zeng, M.A. Ahmad, S. Liu, Nonclassical state via superposition of two coherent states ($\pi/2$ out of phase) and related entangled states, Optics Commun. **271**, 162 (2007).

[180] M. Ashfaq, S.-T. Liu, Superposition of two coherent states π out of phase with average photon number as relative phase, Optik **120**, 68 (2009).

[181] M.A. Ahmad, R. Zeng, S.-T. Liu, Nonclassical properties of superposition of two coherent states shifted in phase by $3\pi/2$, Chin. Phys. Lett. **23**, 2438 (2006).

[182] Hari Prakasha, Pankaj Kumarb, Non-classical properties of superposition of two coherent states having phase difference ϕ, Optik **122**, 1058 (2011).

[183] H. Prakash, P. Kumar, Squeezing in superposed coherent states, Physica A **319**, 305 (2003).

[184] H. Prakash, P. Kumar, Maximum simultaneous squeezing and antibunching in superposed coherent states, Physica A **341**, 201 (2004).

[185] Lu Dao-Ming, The entropic squeezing of superposition of two arbitrary coherent states, Chin. Phys. Soc. **17**, (2008).

[186] B. Yurke, D. Stoler, Generating quantum mechanical superpositions of macro-scopically distinguishable states via amplitude dispersion, Phys. Rev. Lett. **57**, 13 (1986).

[187] M. Brune, S. Haroche, J.M. Raimond, L. Davidovich, N. Zagury, Manipulation of photons in a cavity by dispersive atom-field coupling: quantum-nondemolition measurements and generation of Schrdinger cat states, Phys. Rev. A **45**, 5193 (1992).

[188] J. Gea-Banacloche, Atom-and field-state evolution in the Jaynes-Cummings model for large initial fields, Phys. Rev. A **44**, 5913 (1991).

[189] S. Schaufler, M. Freyberger, W.P. Schleich, The Birth of a Phase-cat, J. Mod. Opt. **41**, 1765 (1994).

[190] B.Roy, Nonclassical properties of the real and imaginary nonlinear Schrdinger cat states, Phys. Lett. A **249**, 25 (1998).

[191] J. Rëcamier, R. Jäuregui, Construction of even and odd combinations of Morse- like coherent states, J. Opt. B: Quant. Semiclass. Opt. **5**, S365 (2003).

[192] L. H. Ford, Thomas A. Roman, Negative energy density in superposition and entangled states , Phys. Rev. D **77**, 045018 (2008).

[193] Werner Vogel, Dirk-Gunnar Welsch, Quantum Optics, WILEY-VCH, Weinheim, (2006).

[194] G. S. Agarwal, K. Tara, Nonclassical properties of states generated by the excitations on a coherent state, Phys. Rev. A **43**, 492 (1991).

[195] C. Brif, Two-Photon Algebra Eigenstates: A Unified Approach to Squeezing, annals of physics, **251**, 180 (1996).

[196] S. M. Barnett, D. T. Pegg, On the Hermitian optical phase operator, J. Mod. Opt. **36**, 7 (1989).

[197] D. T. Pegg, S. M. Barnett, Phase properties of the quantized single-mode electro magnetic field, Phys. Rev. A **39**, 1665 (1989).

[198] C. Gerry, Generation of optical macroscopic quantum superposition states via state reduction with a Mach-Zehnder interferometer containing a Kerr medium ,Phys. Rev. A **59**, 4095 (1999).